(2)

NAVAL POSTGRADUATE SCHOOL

Monterey, California

THESIS

THE SENSITIVITY OF AGEOSTROPHIC CIRCULATIONS
TO MODEL RESOLUTION:
A CASE STUDY USING NGM FORECASTS OF ERICA IOP-4

by

James Berdeguez

December, 1992

Thesis Advisor: Patricia M. Pauley

Approved for public release; distribution is unlimited

REPORT DOCUMENTATION PAGE

1a. REPORT SECURITY CLASSIFICATION Unclassified	1b. RESTRICTIVE MARKINGS
2a. SECURITY CLASSIFICATION AUTHORITY	3. DISTRIBUTION/AVAILABILITY OF REPORT Approved for public release; distribution is unlimited.
2b. DECLASSIFICATION/DOWNGRADING SCHEDULE	
4. PERFORMING ORGANIZATION REPORT NUMBER(S)	5. MONITORING ORGANIZATION REPORT NUMBER(S)
6a. NAME OF PERFORMING ORGANIZATION Naval Postgraduate School 6b. OFFICE SYMBOL (*If applicable*) 35	7a. NAME OF MONITORING ORGANIZATION Naval Postgraduate School
6c. ADDRESS (*City, State, and ZIP Code*) Monterey, CA 93943-5000	7b. ADDRESS (*City, State, and ZIP Code*) Monterey, CA 93943-5000
8a. NAME OF FUNDING/SPONSORING ORGANIZATION 8b. OFFICE SYMBOL (*If applicable*)	9. PROCUREMENT INSTRUMENT IDENTIFICATION NUMBER
8c. ADDRESS (*City, State, and ZIP Code*)	10. SOURCE OF FUNDING NUMBERS Program Element No / Project No / Task No / Work Unit Accession Number

11. TITLE (*Include Security Classification*)
THE SENSITIVITY OF AGEOSTROPHIC CIRCULATIONS TO MODEL RESOLUTION: A CASE STUDY USING NGM FORECASTS OF ERICA IOP-4

12. PERSONAL AUTHOR(S) Berdeguez, James

13a. TYPE OF REPORT	13b. TIME COVERED	14. DATE OF REPORT (*year, month, day*)	15. PAGE COUNT
Master's Thesis	From To	1992 December	145

16. SUPPLEMENTARY NOTATION
The views expressed in this thesis are those of the author and do not reflect the official policy or position of the Department of Defense or the U.S. Government.

17. COSATI CODES			18. SUBJECT TERMS (*continue on reverse if necessary and identify by block number*)
FIELD	GROUP	SUBGROUP	ageostrophic circulations, psi-vector technique, model resolution, ERICA

19. ABSTRACT (*continue on reverse if necessary and identify by block number*)

The effect of model resolution on the ageostrophic circulations and dynamics of a rapidly deepening extratropical cyclone that occurred during the Intensive Observing Period (IOP) 4 (4-5 January 1989) of the Experiment on Rapidly Intensifying Cyclones over the Atlantic (ERICA) is examined using the psi-vector technique proposed by Keyser et al. (1989). A comparison of forecasts made by the National Meteorological Center's Nested Grid Model (NGM) using operational (C-grid) and double-resolution (D-grid) versions indicated central pressure and frontal evolution differences between the two forecasts. The IOP-4 cyclone was observed to deepen by 60 mb in 24 h to a central pressure of 936 mb. The NGM C-grid forecast attained a central pressure at 0000 UTC 5 Jan of 959 mb, while the D-grid forecast attained a central pressure of 949 mb. Differences in the laterally coupled jet streaks between the C- and D-grid forecasts enabled the D-grid forecast to depict stronger transverse ageostrophic circulations that produced stronger ascent and greater spin-up of the low-level cyclone.

20. DISTRIBUTION/AVAILABILITY OF ABSTRACT	21. ABSTRACT SECURITY CLASSIFICATION	
☒ UNCLASSIFIED/UNLIMITED ☐ SAME AS REPORT ☐ DTIC USERS	Unclassified	
22a. NAME OF RESPONSIBLE INDIVIDUAL Patricia M. Pauley	22b. TELEPHONE (*Include Area code*) (408) 646-3275	22c. OFFICE SYMBOL MR/Pa

DD FORM 1473, 84 MAR — 83 APR edition may be used until exhausted; All other editions are obsolete

Approved for public release; distribution is unlimited.

The Sensitivity of Ageostrophic Circulations to Model Resolution:
A Case Study Using NGM Forecasts of ERICA IOP-4

by

James Berdeguez
Lieutenant , United States Navy
B.S., United States Naval Academy, 1985

Submitted in partial fulfillment
of the requirements for the degree of

MASTER OF SCIENCE IN METEOROLOGY AND PHYSICAL OCEANOGRAPHY

from the

NAVAL POSTGRADUATE SCHOOL
December 1992

Author: _____
James Berdeguez

Approved by: _____
Patricia M. Pauley, Thesis Advisor

_____
Carlyle H. Wash, Second Reader

_____
Robert L. Haney, Chairman
Department of Meteorology

ABSTRACT

The effect of model resolution on the ageostrophic circulations and dynamics of a rapidly deepening extratropical cyclone that occurred during the Intensive Observing Period (IOP) 4 (4-5 January 1989) of the Experiment on Rapidly Intensifying Cyclones over the Atlantic (ERICA) is examined using the psi-vector technique proposed by Keyser et al. (1989). A comparison of forecasts made by the National Meteorological Center's Nested Grid Model (NGM) using operational (C-grid) and double-resolution (D-grid) versions indicated central pressure and frontal evolution differences between the two forecasts. The IOP-4 cyclone was observed to deepen by 60 mb in 24 h to a central pressure of 936 mb. The NGM C-grid forecast attained a central pressure at 0000 UTC 5 Jan of 959 mb, while the D-grid forecast attained a central pressure of 949 mb. Differences in the laterally coupled jet streaks between the C- and D-grid forecasts enabled the D-grid forecast to depict stronger transverse ageostrophic circulations that produced stronger ascent and greater spin-up of the low-level cyclone.

TABLE OF CONTENTS

I. INTRODUCTION

The importance of model resolution to the prediction of extratropical cyclone and frontal development has been well established. Sanders (1987) examined the skill of the National Meteorological Center's (NMC) operational dynamical models in the prediction of explosive cyclogenesis and found that the Nested Grid Model (NGM) performed notably better than the Limited Fine-Mesh Model (LFM) in the fine-grid area. Kuo and Low-Nam (1990) performed a series of numerical model experiments for nine cases of rapidly deepening oceanic cyclones and ranked horizontal grid resolution second in importance behind initial conditions. With increasing computer capacity and speed, numerical models will continue to have finer resolution and physics. How does higher model resolution depict lower central pressures in these oceanic storms? In order to provide some insight to this question, this study will focus on the Experiment on Rapidly Intensifying Cyclones over the Atlantic (ERICA) Intensive Observing Period 4 (IOP-4) case, examining the effect model resolution has on ageostrophic circulations in the vicinity of upper-level jet streaks and on the dynamics of explosive deepening.

Previous research on resolution effect by Weygandt and Seaman (1988) examined whether increasing model resolution increased forecast accuracy. Using three different grid resolutions (160, 80, and 26.7 km) in the Penn State/NCAR mesoscale model for five cases of continental cyclogenesis, they found that as grid length is decreased the mesoscale meteorological features were better resolved in 72 h simulations. However, with the smallest grid length (26.7 km) certain aspects, such as cold frontal intensity and propagation, were occasionally predicted to be greater than in the objective analysis. In these cases, the high-resolution forecast may actually be more accurate than the analyses since the standard surface observation network and the objective analysis procedure cannot fully resolve many of these features. This study quantitatively examined the relationship between forecast accuracy and grid resolution. They concluded that as grid resolution is increased, changes in the initialization techniques as well as the model physics must be considered.

The comprehensive study by Kuo and Low-Nam (1990) also examined the impact of horizontal and vertical resolution as well as physical parameterizations on the prediction of nine explosive cyclones over the western Atlantic using the Penn State/NCAR mesoscale model. Their experiments with the Arakawa-Schubert parameterization scheme revealed that a reduction in grid size from 80 km to 40 km contributed to

additional deepening. However, an increase in vertical resolution from 15 layers to 23 layers did not improve the forecast. In fact, a slight reduction in the deepening rate occurred in the 23-layer simulations. They concluded that an optimal vertical resolution was related to the horizontal resolution and that improving the horizontal resolution is more important than improving the vertical resolution for grid-point operational models.

Pecnick and Keyser (1989) studied the effect of spatial resolution on upper-tropospheric frontogenesis using a two-dimensional primitive equation model. They varied the horizontal resolution between 100 and 12.5 km and the number of layers between 10 and 70, and found that increasing grid resolution in both the horizontal and vertical better defined the frontal structure. In addition, the absolute vorticity and potential temperature gradients increased with greater horizontal resolution, although the strength of the jet was relatively insensitive to resolution changes. They concluded that these increases primarily result from decreases in the cross-frontal scale, in other words, tighter gradients. In addition, they found that for each horizontal resolution there is a point where additional vertical resolution has little impact, and therefore, is no longer cost effective.

The question of consistency between horizontal and vertical resolution was also investigated by Persson and Warner (1991), who diagnosed model generation of spurious

gravity waves due to resolution inconsistency. They found a physical relationship between the vertical and horizontal scales, that is determined by the slope of the narrow thermal structures. If there is an inconsistency in model resolution, spurious gravity waves are produced. They concluded that the selection of vertical grid spacing should take into consideration the horizontal grid spacing, consistent with the Pecnick and Keyser (1989) findings.

The effect of resolution on the depiction of the ERICA IOP-4 storm's central pressure was examined by Pauley and Bramer (1992) using a one-dimensional Fourier analysis. The Fourier analysis of pressure profiles from manual analyses suggested that doubling the horizontal resolution in the NGM should be sufficient to capture the 936 mb central pressure for the IOP-4 cyclone at maximum intensity. Since the double resolution D-grid forecast, discussed in more detail in Pauley et al. (1991) and in this thesis, did not reach 936 mb but rather predicted a central pressure of 949 mb in the 48 h forecast, Pauley and Bramer (1992) suggested that other processes, such as mesoscale features too small to be resolved in the observations may have affected the synoptic-scale evolution. If such features are necessary to accurately predict the central pressure in storms as intense as in this one, then further increases in resolution and possibly refinements in physical parameterizations are needed.

The present study uses the operational-resolution NGM C-grid forecast and D-grid forecast of ERICA IOP-4 to examine differences in storm dynamics resulting from differences in resolution. The ageostrophic circulations associated with the upper-level trough/ridge systems and jet streaks will be examined to explore the subsequent rapid deepening of IOP-4 and the sensitivity of the forecasts to resolution. Surface deepening can be related to the spin-up of low-level vorticity. This can be seen by analyzing the frictionless vorticity equation in pressure coordinates, such that

$$\frac{\partial(\zeta+f)}{\partial t} = -\vec{V}\cdot\nabla(\zeta+f) - \omega\frac{\partial\zeta}{\partial p} - (\zeta+f)\,\nabla\cdot\vec{V} - \vec{k}\cdot\left(\nabla\omega\times\frac{\partial\vec{V}}{\partial p}\right). \quad (1.1)$$

Assuming that the horizontal and vertical advections of vorticity and tilting of the horizontal components of vorticity into the vertical may be ignored at the surface cyclone center (Petterssen 1956), then (1.1) becomes

$$\frac{\partial(\zeta+f)}{\partial t} \approx -(\zeta+f)\nabla\cdot\vec{V}. \quad (1.2)$$

Equation (1.2) indicates that the absolute vorticity intensifies at the surface cyclone center due to horizontal convergence scaled by absolute vorticity (Petterssen 1956). Horizontal convergence is related to vertical motion by the continuity equation, such that

$$\nabla\cdot\vec{V} = -\frac{\partial\omega}{\partial p}. \quad (1.3)$$

Therefore, the upward motion at or near the surface cyclone center is associated with low-level horizontal convergence which causes stretching of the column of air and cyclonic spin-up, and therefore deepening of the surface low center. Gyakum et al. (1992) emphasized the role of the pre-existing surface vorticity in the deepening process, and found that greater antecedent vorticity was generally followed by greater deepening as suggested by (1.2). The objective of this study is to detail the role of the low-level horizontal convergence as inferred from the vertical gradient of omega associated with the ageostrophic vertical circulations accompanying the upper-level trough/ridge system and jet streaks. The following chapters will cover jet streak dynamics, an overview of the NGM C- and D-grid model configurations, the synoptic situation of IOP-4, diagnostic computations in partitioning the ageostrophic circulation, and the findings of this study.

II. BACKGROUND

The development of a surface cyclone requires a net reduction in mass in the column of air directly over the incipient cyclone. This can be accomplished by either net divergence in the column or net advection of less dense air, the former of which is generally emphasized. Since the low-level wind field is generally convergent, the upper-level divergence must exceed the low-level convergence for development of a cyclone, following Dines' compensation. As seen in Figure 2.1, the structure of upper-level divergence is associated with the presence of upper-level trough/ridge patterns which lead to longitudinal (or along-stream) ageostrophic wind components opposing the flow upstream of cyclonic curvature and along the flow downstream of anticyclonic curvature (Kocin and Uccellini 1990).

The jet streak pattern also plays an important role in the upper-level divergence and vorticity structure by contributing transverse (or cross-stream) ageostrophic components, thereby altering the divergence field and influencing the development of the surface cyclone (Kocin and Uccellini 1990). Jet streams are narrow cores of higher velocity winds located within a larger region of lower velocity winds. Maxima that occur along the jet stream are known as jet streaks. The

entrance region of an idealized jet streak is where the transverse ageostrophic component is directed toward the cyclonic-shear side of the jet, and the exit region is where this component is directed toward the anticyclonic-shear side of the jet, as seen in Figure 2.2a (Uccellini and Kocin 1987). A four-quadrant divergence/convergence pattern is associated with these transverse ageostrophic winds. Furthermore, in the entrance (exit) region, the transverse ageostrophic components represent the upper branch of the direct (indirect) circulation which converts available potential (kinetic) energy into kinetic (available potential) for parcels accelerating (decelerating) into (out of) the jet (Fig 2.2b).

Uccellini and Kocin (1987) illustrated the interaction between individual transverse circulations and the development of heavy snow events along the East Coast of the United States. Figure 2.3 depicts the lateral coupling of a favorably aligned thermally direct circulation near a northern jet-entrance region and a thermally indirect circulation near a southern jet-exit region, which together produce a region of strong ascent located between the two jet streaks. This strong ascent generally coincides with a heavy snowfall event. In this study, the thermally direct and indirect circulations will be diagnosed in cross-sections by forming circulation vectors from the divergent ageostrophic wind and vertical motion fields. These circulations will also be compared with

the ageostrophic vertical circulations associated with the upper-level trough/ridge patterns.

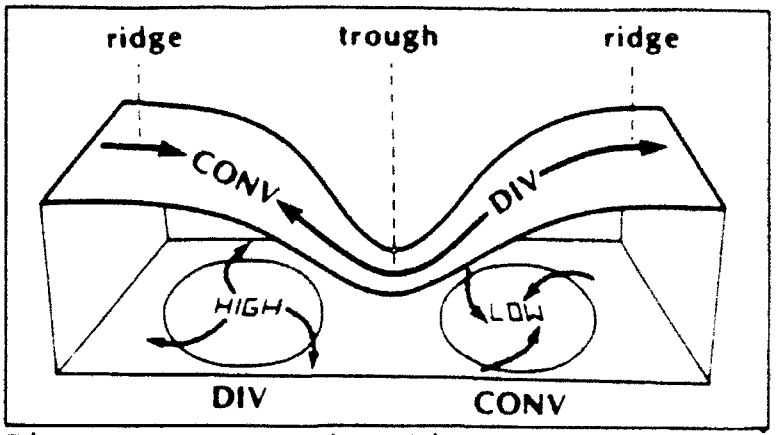

Figure 2.1. Schematic relating the alongstream ageostrophic wind (arrows) to patterns of divergence associated with an upper-level trough/ridge system. (From Kocin and Uccellini 1990)

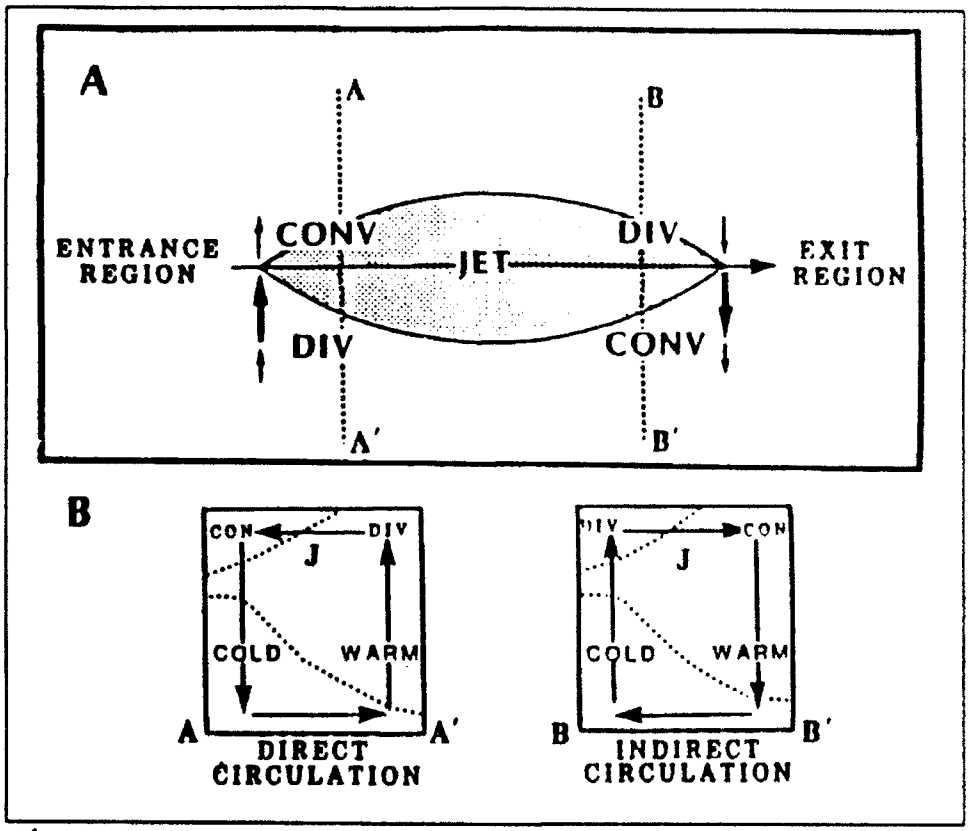

Figure 2.2. (a) Schematic of the transverse ageostrophic wind within a jet entrance and exit regions. (b) Vertical cross-section of direct (AA′) and indirect (BB′) circulations within the jet entrance and exit regions. (From Uccellini and Kocin 1987)

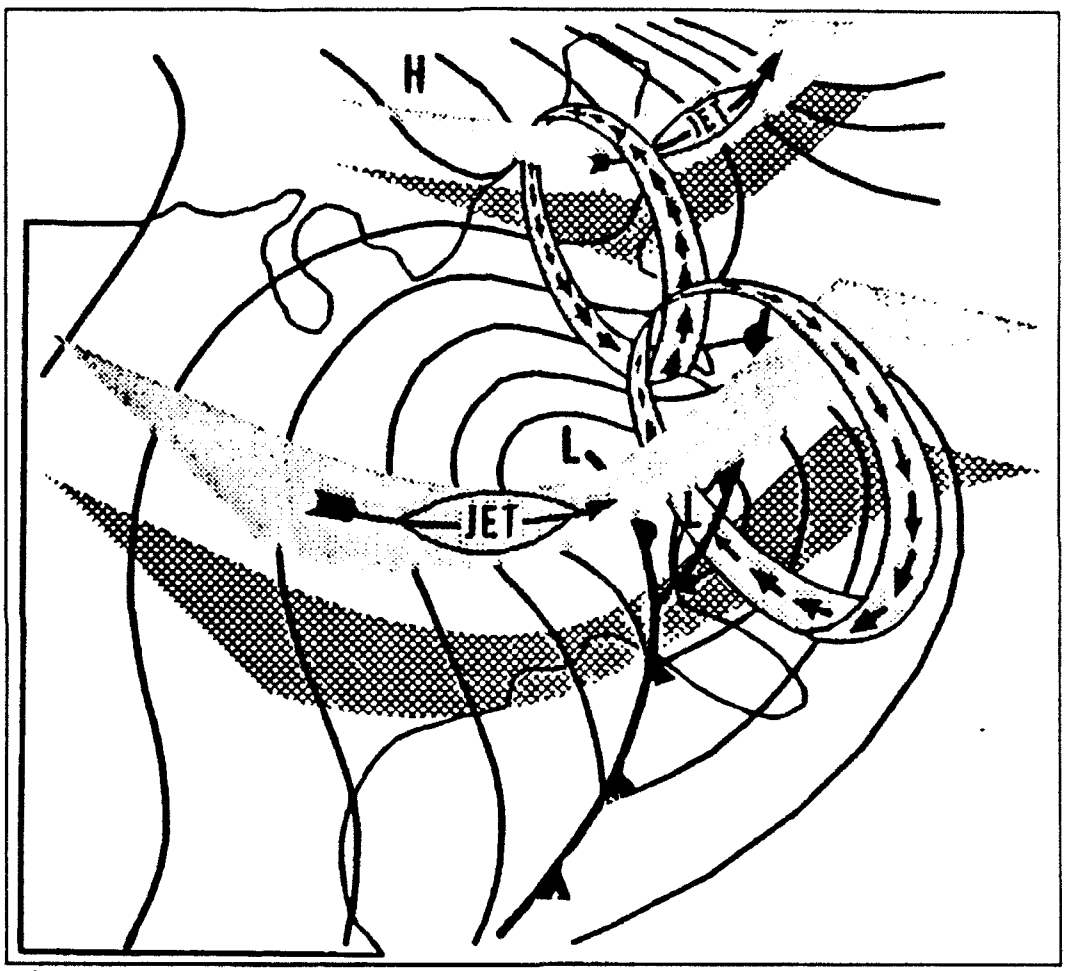

Figure 2.3. 3-D schematic of coupled ageostrophic vertical circulations associated with a jet-entrance region to the north, and a jet-exit region to the south. (From Hakim and Uccellini 1992)

III. THE NESTED GRID MODEL (NGM)

The NGM is the forecast component of the National Meteorological Center's (NMC) Regional Analysis and Forecast System (RAFS) which was designed to improve short-range numerical guidance over that provided by NMC's Limited-area Fine-mesh Model (LFM) (Hoke et al. 1989). This research uses forecasts to 48 h which were made by an experimental version of the NGM. The following section provides a brief description of the operational NGM as of 1989 when these forecasts were performed, as well as aspects that differ in the experimental version.

The NGM is a stand-alone model that does not require boundary conditions from a larger-scale model. The 1989 version of the operational NGM has a three-grid configuration, with the outermost grid (A-grid) covering the northern hemisphere. Each interior grid has twice the resolution of the grid surrounding it, and allows a two-way exchange of information at the boundaries between the grids (Hoke et al. 1989). For this study the NGM configuration was supplemented with an additional nested grid (D-grid) with double the resolution of the surrounding C-grid.

Figure 3.1 depicts the horizontal domain of the D-grid used in this study. The entire grid system was rotated 20°

east of the operational configuration for both the C- and D-grid forecasts to ensure boundary effects would have a minimal influence on the IOP-4 cyclone (Pauley et al. 1991). The C-grid has a horizontal resolution of 92.45 km at 60°N, whereas the D-grid has a horizontal resolution of 46.44 km at 60° N.

The operational NGM is run with 16 sigma level in the vertical on all grids. Out of these 16 levels, 13 are in the troposphere with layer thickness varied to yield the greatest resolution in the planetary boundary layer. For the D-grid version, the vertical resolution is doubled over the entire grid system. As seen in Figure 3.2, each of the 16 sigma levels is divided into two layers retaining the functional relationship of the layer thickness to height (Houghton et al. 1992).

The NGM uses an Arakawa-D system of staggering the forecast variables in the horizontal, along with a Lax-Wendroff time differencing scheme (Hoke et al. 1989). The time step is 75 s for the C-grid and 37.5 s for the D-grid. A fourth-order Shapiro-type smoothing operator is applied to the horizontal components of the wind, potential temperature and specific humidity as a method of noise control for the NGM forecasts. A variety of physical processes are modeled in the NGM, including convective and grid-scale precipitation, longwave and shortwave radiation, the exchange of momentum, heat and moisture between the surface of the earth and the atmosphere, boundary-layer mixing, dry convection and vertical

turbulent transport by eddies (Hoke et al. 1989). The parameterizations were not varied in these experiments.

The model output was post-processed to vertically interpolate all quantities to pressure surfaces from 1000 mb to 100 mb at a 50 mb increment. In additon, the output from both forecasts was horizontally interpolated to a subset of the C-grid east of approximately 85°W. Diagnostic calculations presented in this thesis were computed from the post-processed datasets.

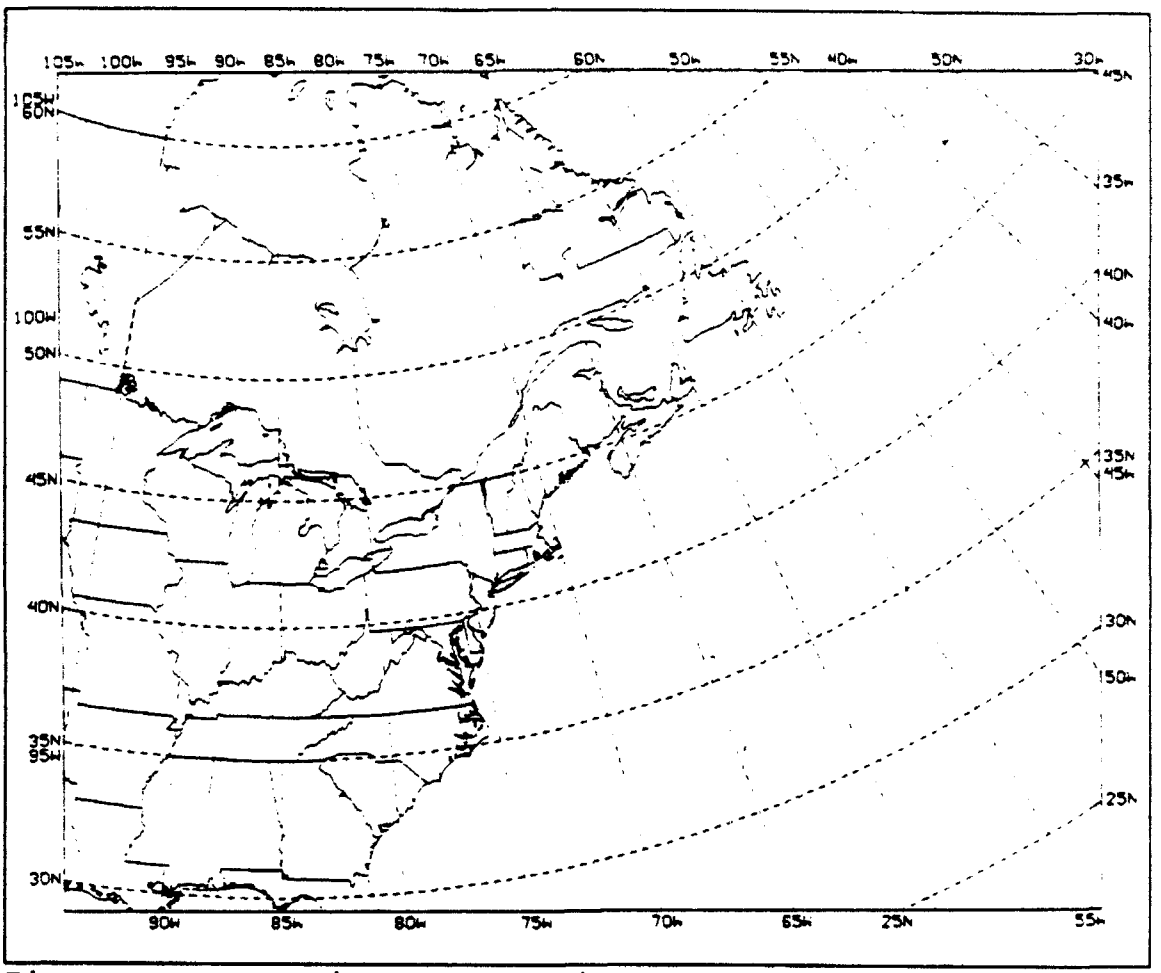

Figure 3.1. Horizontal domain used for the NGM D-grid forecast.

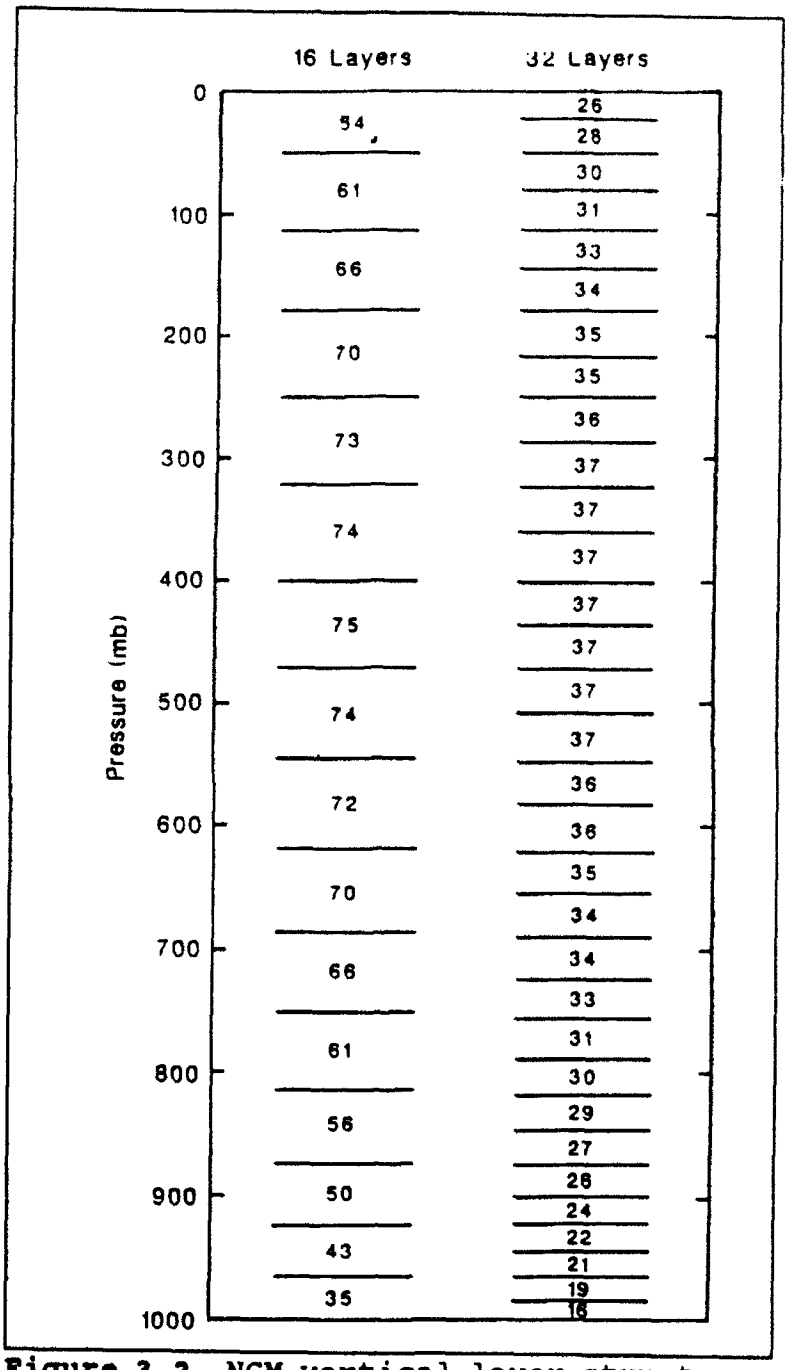

Figure 3.2. NGM vertical layer structure: 16-layer C-grid and 32-layer D-grid configuration. Pressure values assume a surface value of 1000 mb. (From Houghton et al. 1992)

IV. SYNOPTIC DISCUSSION

This section describes the development of the ERICA IOP-4 storm as observed and as predicted by the NGM in the C-grid and D-grid configurations described above. In the first part, operational NGM analyses are used to describe the synoptic situation and are compared to research-quality manual analyses by Sanders (personal communication), Neiman and Shapiro (1992; hereafter referred to as NS) and Wakimoto et al. (1992; hereafter referred to as WK). These analyses are also used for verification of the NGM C- and D-grid forecasts. The NGM analyses were prepared from the operational data stream and had no benefit of the supplemental ERICA observations. However, all three sets of manual analyses did utilize supplemental data from ships, buoys, ERICA aircraft, and satellites, with the emphasis in the Sanders analyses on synoptic-scale features and the emphasis in the other two on the mesoscale. The NS analyses were based primarily on in-situ observations using a time-to-space adjustment to better examine frontal features. WK superimposed surface analyses, radar composites based on aircraft radar reflectivity data, and satellite imagery in order to correlate features in the remotely sensed data with in-situ observations. In the second part of this section, the NS 850 mb analyses and WK radar

analyses are compared to the NGM 850 mb forecasts with an emphasis on verifying the model-predicted mesoscale thermal structure.

A. VERIFICATION OF SYNOPTIC-SCALE FEATURES

The ERICA IOP-4 storm began to develop as a surface trough at approximately 1200 UTC 03 January 1989 (12Z/03)[1] just off Cape Hatteras, North Carolina, and formed a closed center with a central pressure of 996 mb by 0000 UTC 04 January (00Z/04). The system deepened 60 mb in the following 24 h to a central pressure of 936 mb at 0000 UTC 05 January (00Z/05), according to the Sanders and NS hand analyses.

Figure 4.1 is a comparison of central sea-level pressures during this period between the NGM analyses and forecasts and the hand analyses by Sanders, NS, and WK. Throughout the entire period, these manual analyses agree within 3 mb. The NGM analysis was available only every 12 h, therefore does not have central pressure values for 06Z/04 and 18Z/04. Note that the NGM analysis is in close agreement with the hand analyses at 00Z/04 and 12Z/04, but only deepens the storm to 946 mb by 00Z/05. As discussed by Pauley and Bramer (1992), the operational NGM C-grid cannot be expected to capture the intense pressure gradient near the storm center, due to limitations in resolution and the smoothing inherent in the

[1]Times will be abbreviated as hhZ/dd where hh is hour (UTC) and dd is date.

analysis scheme. During the first 6 h, the NGM D-grid forecast was very slow to deepen the cyclone; however after this initial period, the deepening rate is nearly equivalent to that in the Sanders analyses. In contrast, the NGM C-grid forecast was slow to deepen the cyclone throughout the life cycle of the storm, again reflecting resolution limitations.

1. 1200 UTC 03 January (12Z/03)

The NGM model forecasts examined in this research were initialized 12 h prior to this time. At 12Z/03, there is a surface low pressure system located over Wisconsin with a secondary low center over Kentucky in the NGM analysis (Fig. 4.2a). A 500 mb shortwave trough over Minnesota and Iowa provides upper-level support for the primary surface low (Fig. 4.2b). Over the next 12 h, the positive vorticity advection (PVA) associated with the absolute vorticity maximum of 20×10^{-5} s^{-1} in this trough moves rapidly toward the coast and provides the upper-level support for the generation of the IOP-4 surface cyclone. The 18Z/03 Sanders analysis (not shown) shows a hint of the old Kentucky low over Virginia at that time. Satellite imagery (not shown) and thermal steering suggest that IOP-4 formed as a secondary cyclone associated with the Kentucky low and in the wake of another very intense cyclone which aided in setting up the strong dynamical and thermodynamical forcing.

2. 0000 UTC 04 January (00Z/04)

A closed low, which was the incipient IOP-4 storm, formed at the surface near Cape Hatteras with a central pressure of 998 mb in the NGM analysis (Fig. 4.3a). The thickness and sea level pressure pattern implies significant cold air advection to the southwest and warm air advection to the east of the low. Both the Sanders and the NS analyses are similar to the NGM analysis, but have central pressures of 996 mb (Figs. 4.4a,b). The NS analysis also indicates a low over Virginia, which could possibly be the old Kentucky low.

The NGM C- and D-grid 24 h forecasts valid at 00Z/04 position the surface low pressure center west of the analyzed position, centered over North Carolina and Virginia (Figs. 4.5a,b). Perhaps the low depicted in these forecasts is actually the former Kentucky low and not the incipient IOP-4 storm, in which case both NGM forecasts miss or mistime the formation of the secondary low. The NGM D-grid low center is slightly east of the NGM C-grid low with indications of a trough extending toward the southeast, where the IOP-4 storm formed. The NGM C-grid and D-grid forecast thickness patterns are similar to each other and to the NGM analysis, although a thickness ridge is present in the analysis to the southeast of the low pressure center which is not evident in either of the forecasts. Over the next 6 h, the system will develop from an open wave to a triple point low with an incipient bent-back warm front to the west.

The NGM 500 mb analysis shows a trough near 85°W approaching the coast (Fig. 4.3b). The absolute vorticity maximum associated with this trough has intensified to 26×10^{-5} s^{-1} over the previous 12 h, with its large region of significant PVA located over the cyclone's surface center, providing excellent upper-level support for rapid intensification. According to Sanders and Auciello (1989), the criteria for predicting explosive cyclogenesis include a 500 mb absolute vorticity maximum of 17×10^{-5} s^{-1} or more in the NGM initial analysis, maintaining intensity or strengthening during the NGM forecast cycle and crossing the coast during the forecast interval. The NGM C-grid 24 h forecast vorticity pattern agrees well with the NGM analysis (Fig. 4.6a). Due to its finer resolution, the NGM D-grid 24 h forecast vorticity pattern is more complex than the analysis and C-grid forecast, with a greater number of minima and maxima. The NGM D-grid forecast indicates a vorticity maximum of 28×10^{-5} s^{-1} located over Tennessee and a second maximum of 16×10^{-5} s^{-1} just off the coast near Cape Hatteras (Fig. 4.6b).

3. 1200 UTC 04 January (12Z/04)

The IOP-4 storm intensified to 960 mb, a remarkable decrease of 36 mb in 12 h, and propagated eastward to a position near 37°N 66°W at 12Z/04 (Fig. 4.7a). A strong pressure gradient has developed especially to the west of the low center, and the thickness contours have gained the

distinctive "s-shape". Both the Sanders and the NS analyses agree with the NGM central pressure and position (Figs. 4.8a,b)

The NGM C-grid and D-grid 36 h forecast low center positions are close to the NGM analysis with the C-grid center moving slightly faster than the D-grid center (Figs. 4.9a,b). As previously mentioned, the C-grid and D-grid predicted central pressures were significantly weaker than observed, at 980 mb and 973 mb, respectively. However, the 6 h period ending at this time yielded the greatest difference in deepening rates between the two forecasts. The NGM C- and D-grid forecast thickness patterns are similar to the NGM analysis; however the C-grid thickness ridge near the cyclone center has less amplitude than the D-grid forecast, which in turn has less amplitude than the analysis.

The NGM 500 mb analysis shows the trough has propagated eastward to 70°W, and the absolute vorticity maximum has increased to 28×10^{-5} s^{-1} by this time (Fig 4.7b). The region of PVA ahead of the trough is over the surface cyclone's center which supports further intensification. The NGM C-grid 36 h forecast vorticity pattern is similar with a maximum of 28×10^{-5} s^{-1} (Fig. 4.10a). Again, the NGM D-grid 36 h forecast vorticity pattern is more complex and stronger than that of the NGM analysis with a maximum of 36×10^{-5} s^{-1} (Fig. 4.10b).

4. 0000 UTC 05 January (00Z/05)

The IOP-4 storm reached its maximum intensity at approximately 00Z/05 with a central pressure of 946 mb in the NGM analysis (Fig. 4.11a). A strong pressure gradient exists, especially to the west of the cyclone, and the thickness contours indicate strong warm air advection to the north and strong cold air advection to the south of the cyclone. The Sanders and NS analyses depict the central pressure of the IOP-4 storm at 936 mb at this time, 10 mb deeper than the NGM analysis and a 24 mb decrease over the previous 12 h (Figs. 4.12a,b). The WK analysis (not shown) has the central pressure at 938 mb.

The NGM C- and D-grid 48 h forecast positions are somewhat west of the NGM analysis, with the D-grid position slightly lagging the C-grid position. Central pressures are 959 mb and 949 mb for the C- and D-grid forecasts, respectively (Figs. 4.13a,b). The thickness patterns in the two forecasts are similar to the NGM analysis with the D-grid having a stronger thickness gradient along the west side of the low center.

The NGM 500 mb analysis (Fig. 4.11b) shows a closed low just to the west of the surface center. However, the absolute vorticity maximum is directly over the surface center and has decreased in intensity to 26×10^{-5} s^{-1}. Over the next 24 h, the system will become vertically stacked and slowly begin

to fill. Both the NGM C- and D-grid 48 h forecast vorticity patterns are more complex and stronger than the NGM analysis, with the C-grid forecast having a broader maximum elongated along a north-south axis and an absolute vorticity maximum of $32x10^{-5}$ s^{-1} (Figs. 4.14a,b). The D-grid forecast has an s-shaped pattern with a maximum of $40x10^{-5}$ s^{-1}.

B. VERIFICATION OF MESOSCALE THERMAL AND FRONTAL STRUCTURES

This section examines the frontal evolution of the ERICA IOP-4 cyclone as characterized by the NS 850 mb temperature analyses and by the WK surface and radar analyses, compared to the NGM forecasts. NS point out that the 850 mb temperature evolution of the IOP-4 storm departs significantly from that of the Norwegian frontal-cyclone model and is more indicative of the alternative model of frontal-cyclone evolution proposed by Shapiro and Keyser (1990). The Shapiro-Keyser conceptual model describes four phases of frontal structure during the life cycle of marine extratropical cyclones: (1) the incipient broad-baroclinic phase; (2) the frontal fracture in the vicinity of the cyclone center and scale contraction of the discontinuous warm and cold frontal gradients; (3) frontal T-bone and bent-back warm front; and (4) the warm-core seclusion.

The NGM C- and D-grid frontal structures are slow to evolve and trail the NS hand analyses, but follow the Shapiro-Keyser model nevertheless. The verifying analyses will

therefore be offset by 6 h to document the extent to which the NGM produces similar frontal features. For example, the 06Z/04 analysis will be used to verify the NGM 36 h forecast, valid at 12Z/04.

1. 0600 UTC 04 January (06Z/04)

The NS analysis (Fig. 4.15) at 06Z/04 shows the frontal fracture phase with the warm-frontal and cold-frontal temperature gradients separated south of the low center. The WK surface analysis (not shown), however, indicates the cyclone is beginning to form a T-bone structure, as the cold front intersects the warm front at right angles to the east of the low center. The radar reflectivity structure composite (not shown) shows the warm-frontal structure extends west then south as it begins to wrap around the low.

The NGM C-grid 36 h forecast (Fig. 4.16a), valid at 12Z/04, indicates a slight weakening of the cold-frontal temperature gradient near the low center, however, not enough to signify the beginning of a frontal fracture. The D-grid 36 h forecast (Fig. 4.16b), however, does depict a weakening of the temperature gradient south of the low center, and so more closely resembles the 06Z/04 NS analysis.

2. 1200 UTC 04 January (12Z/04)

The NS analysis (Fig. 4.17) at 12Z/04 indicates the cyclone possesses a T-bone frontal configuration at the triple point, where the north-south-oriented cold front intersects

the west-east-oriented warm front (NS). A north-south oriented bent-back warm front exists west and south of the low center.

The NGM C-grid 42 h forecast, valid at 18Z/04, continues to show the cold-frontal temperature gradient extending into the low center with no evidence of a frontal fracture (Fig. 4.18a). On the other hand, the D-grid 42 h forecast indicates a T-bone structure and a well-developed bent-back warm front. The bent-back, however, is not as contracted as in the NS analysis and is not yet beginning to wrap around the low center to the south (Fig. 4.18b).

3. 1800 UTC 04 January (18Z/04)

The NS analysis (Fig. 4.19) at 18Z/04 shows the bent-back warm front continuing to contract and beginning to evolve into the mature warm-core seclusion phase (NS). A warm-core seclusion occurs when the bent-back warm front encircles the cyclone center, thereby leaving a pocket of relatively warm air in the center of the cyclone. The WK surface and radar analyses (not shown) also indicate the bent-back warm front has continued to wrap around low and is entering the warm-core seclusion phase.

The NGM C-grid 48 h forecast, valid at 00Z/05, is beginning to develop a weak bent-back warm front with some evidence of a frontal fracture in the cold front, but no T-bone structure (Fig. 4.20a). The NGM D-grid 48 h forecast

depicts the bent-back warm front as continuing to wrap around the cyclone, but somewhat slower than indicated in the NS analysis (Fig. 4.20b).

4. 0000 UTC 05 JANUARY (00Z/05)

The NS analysis at 00/05 shows the cyclone has evolved into the mature warm-core seclusion phase (Fig. 4.21). The WK surface analyses (not shown) indicate the bent-back warm front wrapped around the low with a pressure trough extending to the south-southeast from the low center. This pattern enables the cold air to wrap around and seclude the warmer air to the rear of the cold front (WK).

The NGM forecasts model runs were not available for the valid time 06Z/05 and probably would not have depicted the details of a mature warm-core seclusion. Even on the D-grid, the model resolution is likely not fine enough to capture this small-scale feature.

Overall, the NGM D-grid forecast performed much better than that for the C-grid. Except for the initial delay in deepening the IOP-4 cyclone, the D-grid deepening rates were similar to the observed and substantially greater than the C-grid deepening rates. In addition, except for the warm-core seclusion phase, the D-grid forecast depicted mesoscale frontal structures similar to NS, although, the D-grid was slow to evolve these features. The C-grid forecast, however, was very slow to develop the frontal features, and did not

portray a T-bone structure even at 00Z/05 but rather kept the cold front at the center of the low.

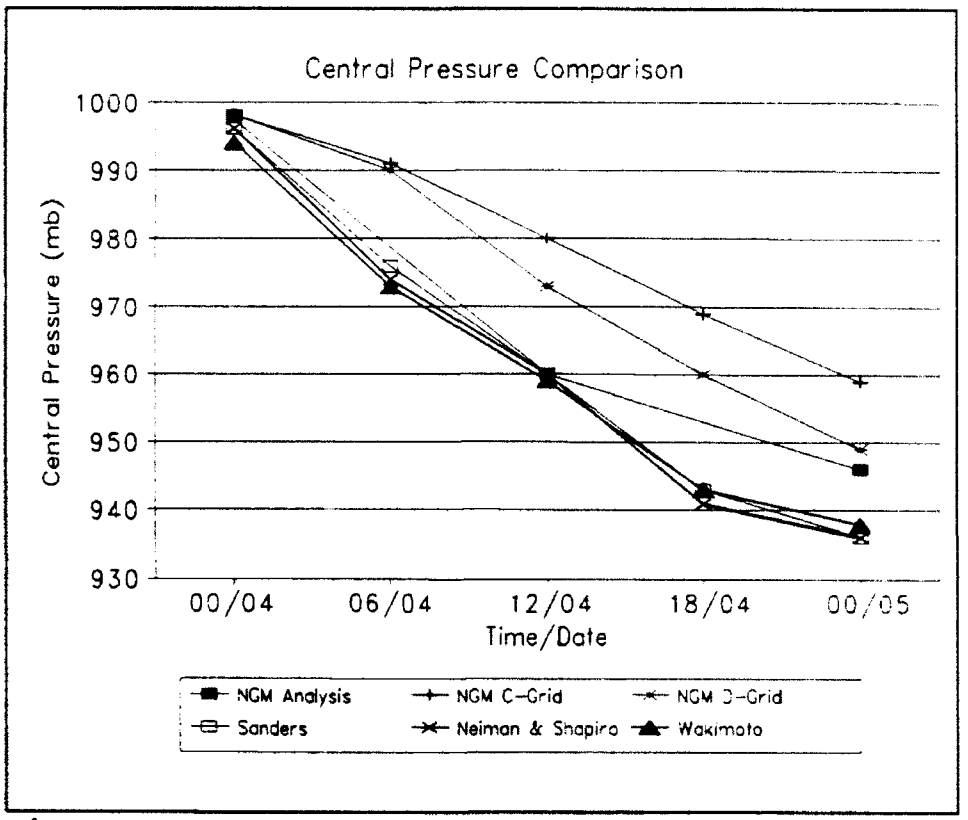

Figure 4.1. IOP-4 central pressure comparison for the NGM C- and D-grid 24 to 48 h forecasts and four verifying analyses.

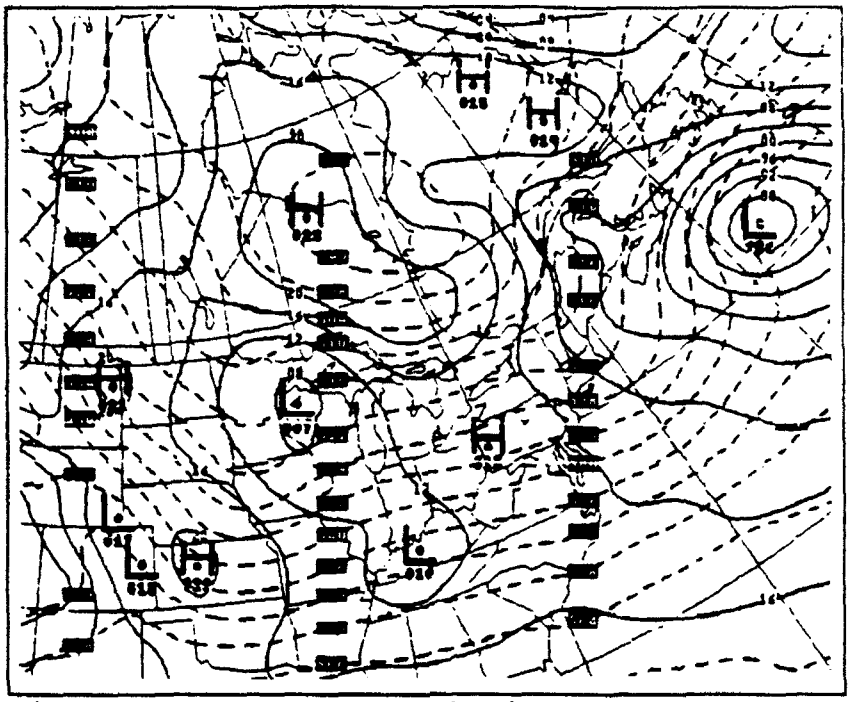

Figure 4.2a. NGM analysis of sea level pressure (solid, 4 mb increment) and 1000-500 mb thickness (dashed, 6 dm increment); at 12Z/03.

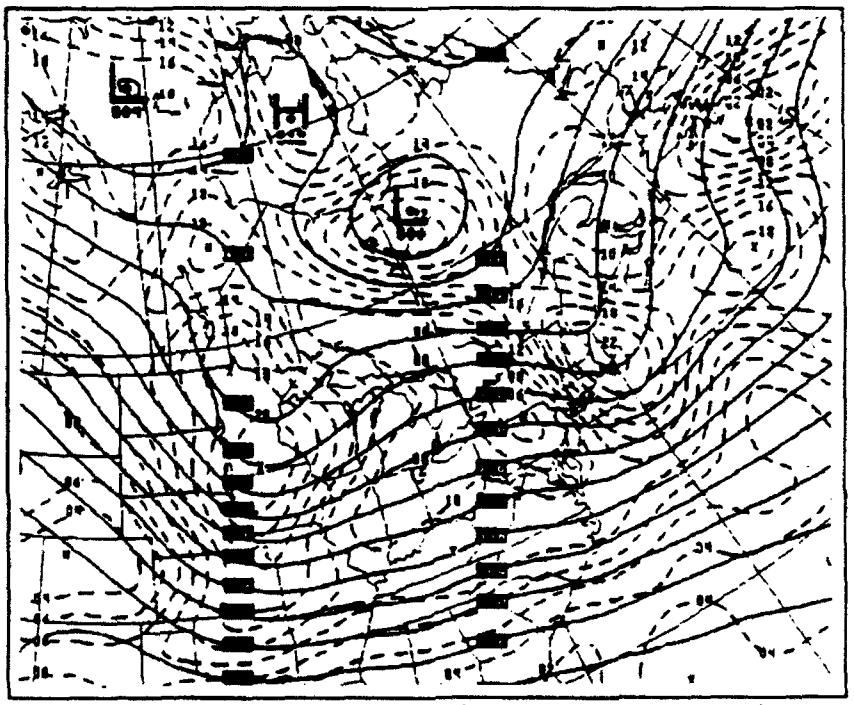

Figure 4.2b. NGM analysis of 500 mb heights (solid, 6 dm increment) and absolute vorticity (dashed, $2x10^{-5}$ s^{-1} increment); at 12Z/03.

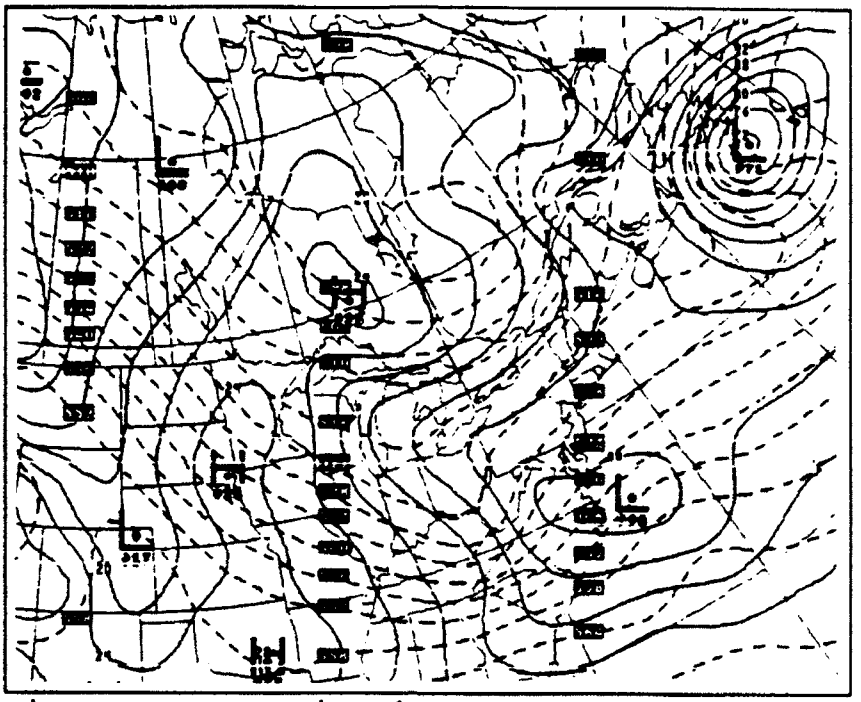

Figure 4.3a. As in Fig. 4.2a, except 00Z/04

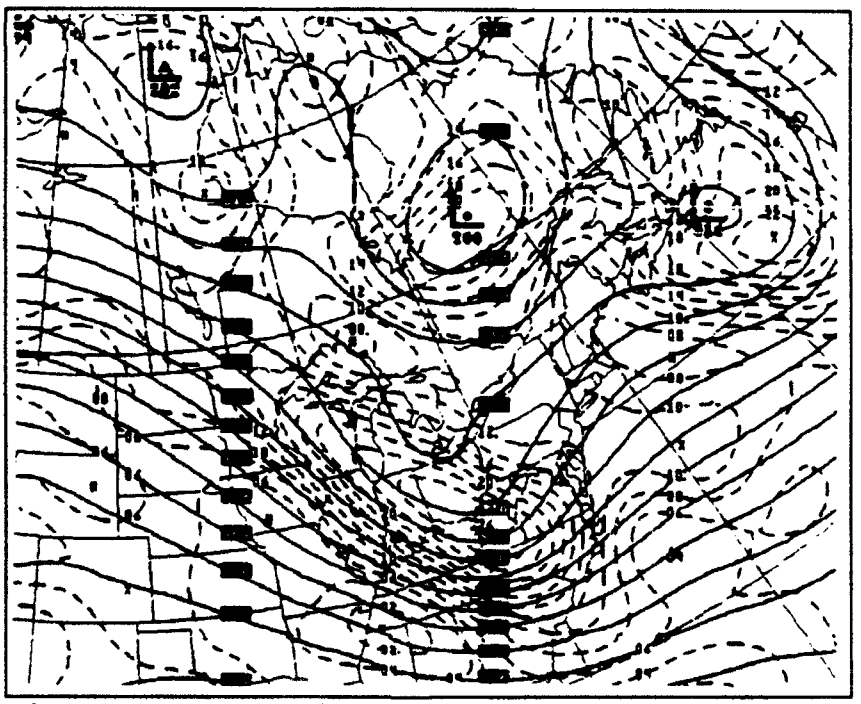

Figure 4.3b. As in Fig. 4.2b, except 00Z/04

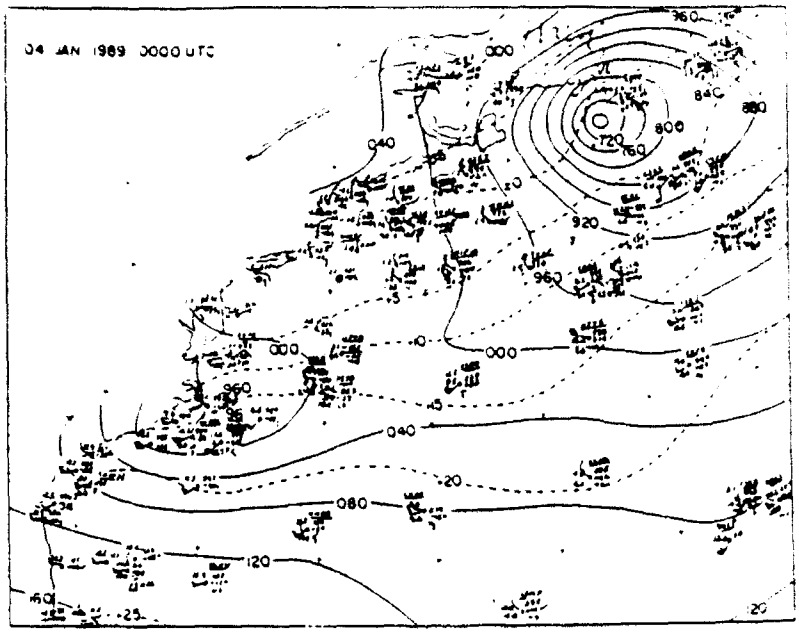

Figure 4.4a. Sanders' analysis of sea level pressure (solid, 4 mb increment) and surface air temperature (dashed, 5°C increment); at 00Z/04.

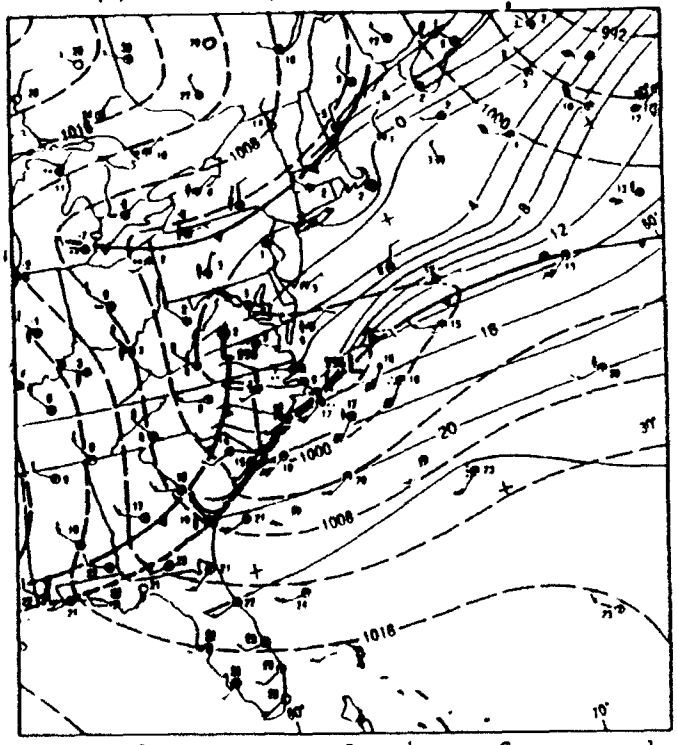

Figure 4.4b. NS analysis of sea level pressure (dashed, 4 mb increment) and surface air temperature (solid, 2°C increment); at 00Z/04.

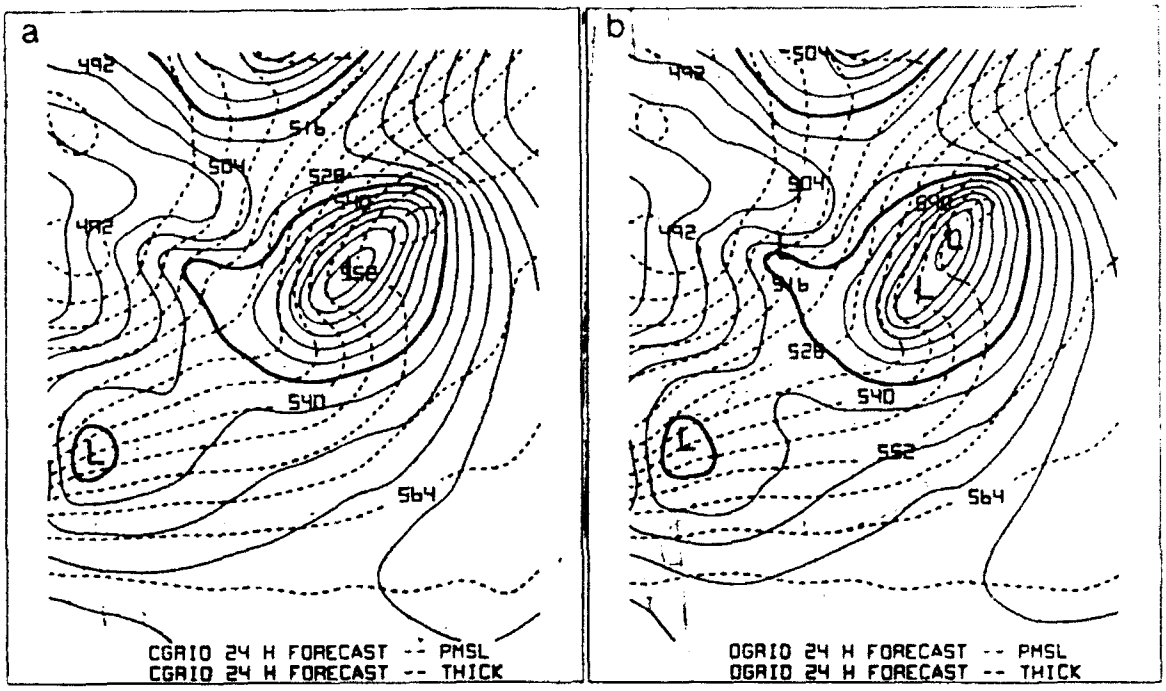

Figure 4.5. NGM 24 h forecast, verification time 00Z/04: (a) C-grid: sea level pressure, 4 mb increment (1000 mb bold contour), and 1000-500 mb thickness (dashed), 6 dm increment; (b) D-grid: as in (a).

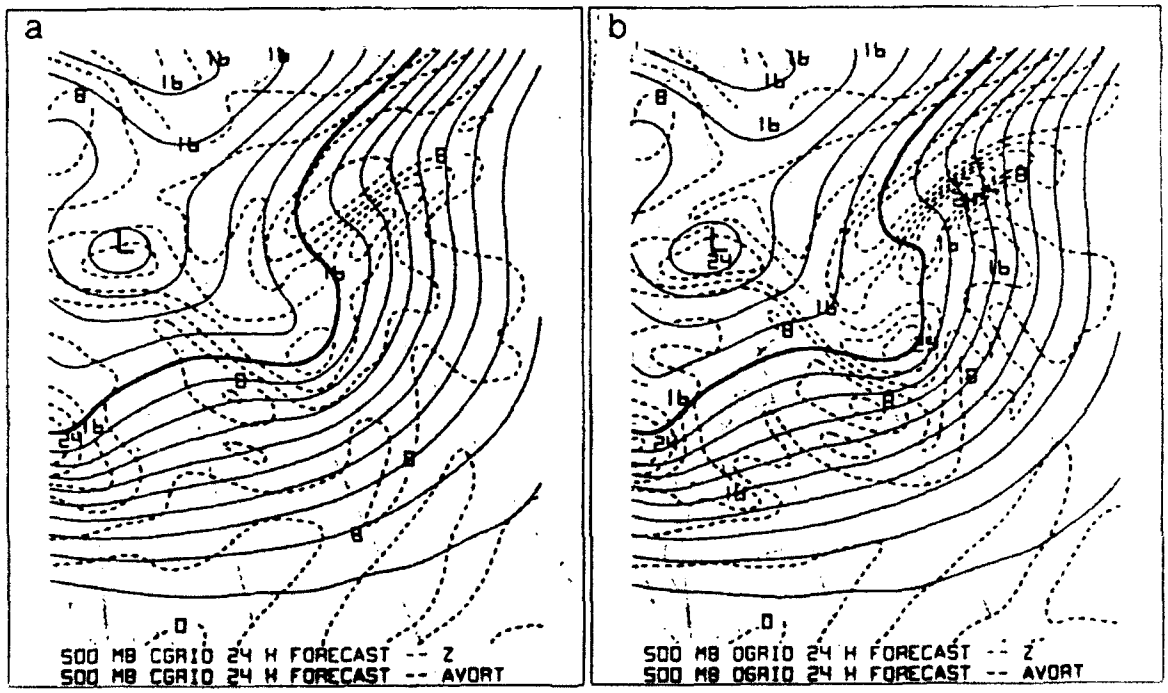

Figure 4.6. NGM 24 h forecast, verification time 00Z/04: (a) C-grid: 500 mb heights, 6 dm increment (528 dm bold contour), and absolute vorticity (dashed), 4×10^{-5} s^{-1} increment; (b) D-grid: as in (a).

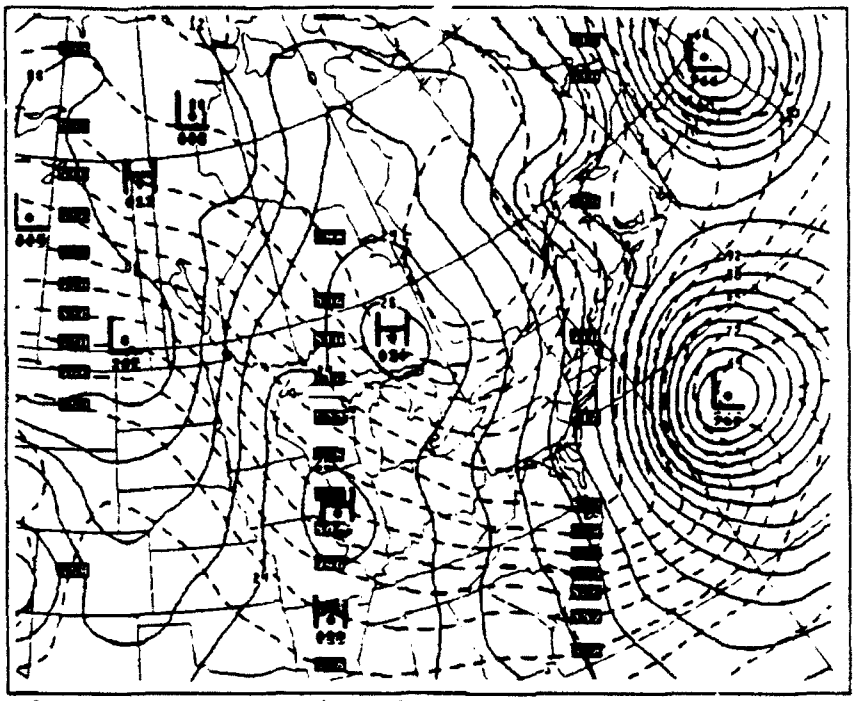

Figure 4.7a. As in Fig. 4.3a, except 12Z/04.

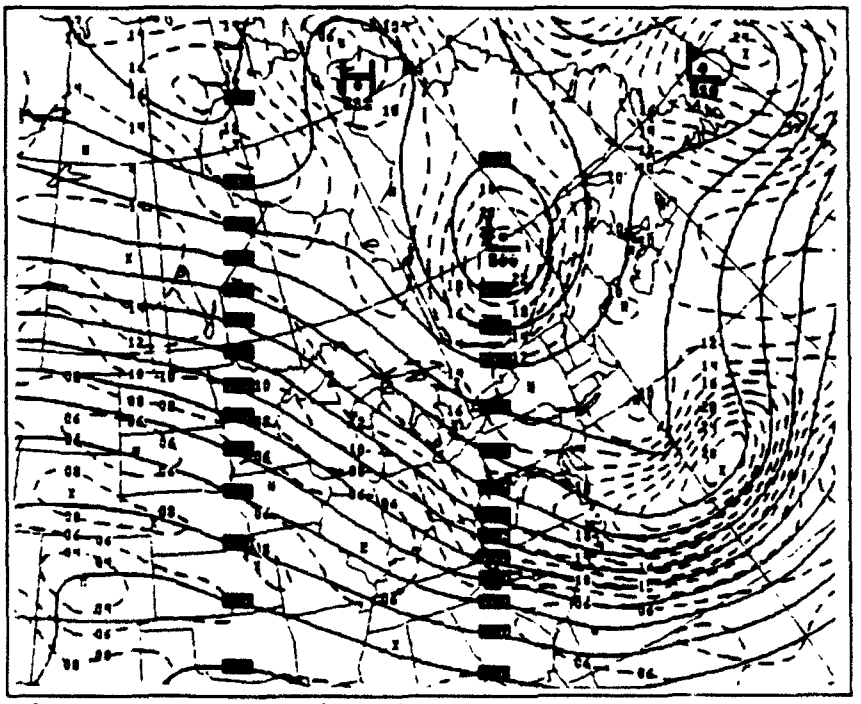

Figure 4.7b. As in Fig. 4.3b, except 12Z/04.

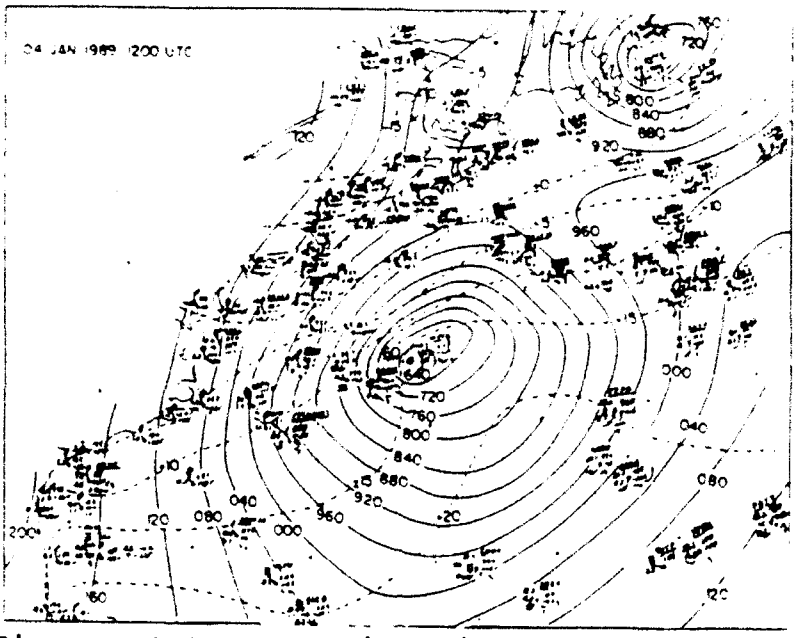

Figure 4.8a. As in Fig. 4.4a, except 12Z/04.

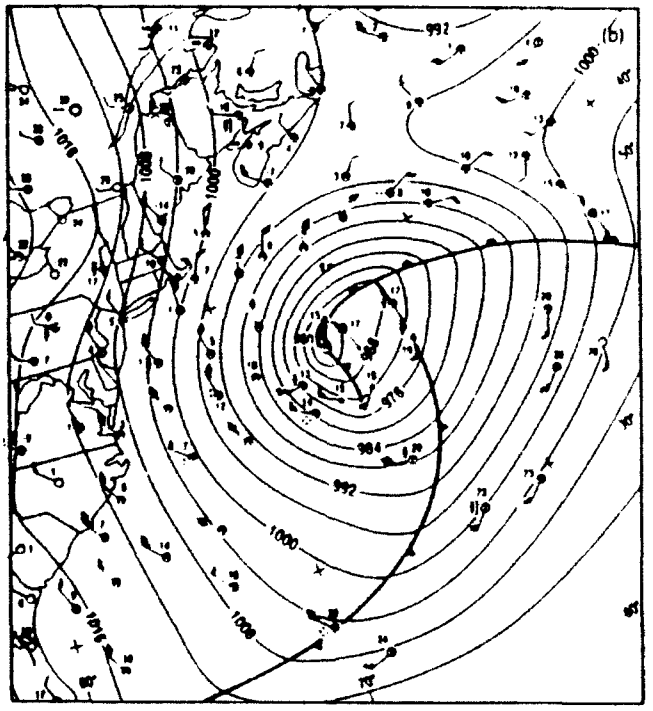

Figure 4.8b. NS analysis of sea level pressure, 4 mb increment; at 12Z/04.

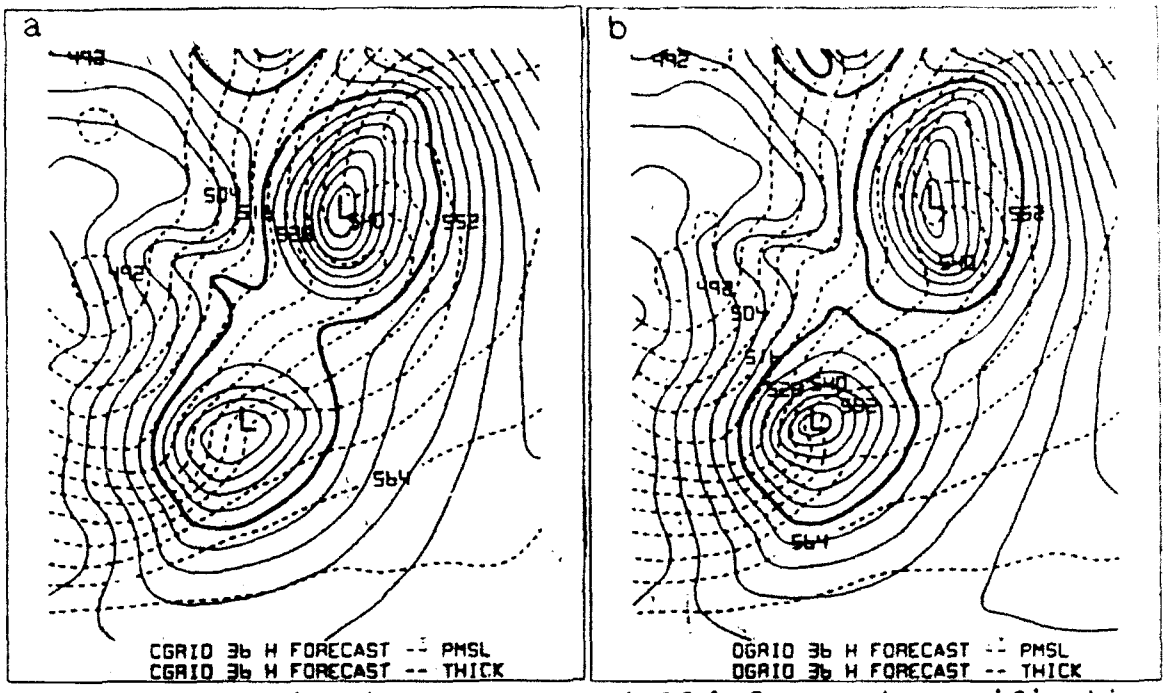

Figure 4.9. As in Fig. 4.5, except 36 h forecast, verification time 12Z/04.

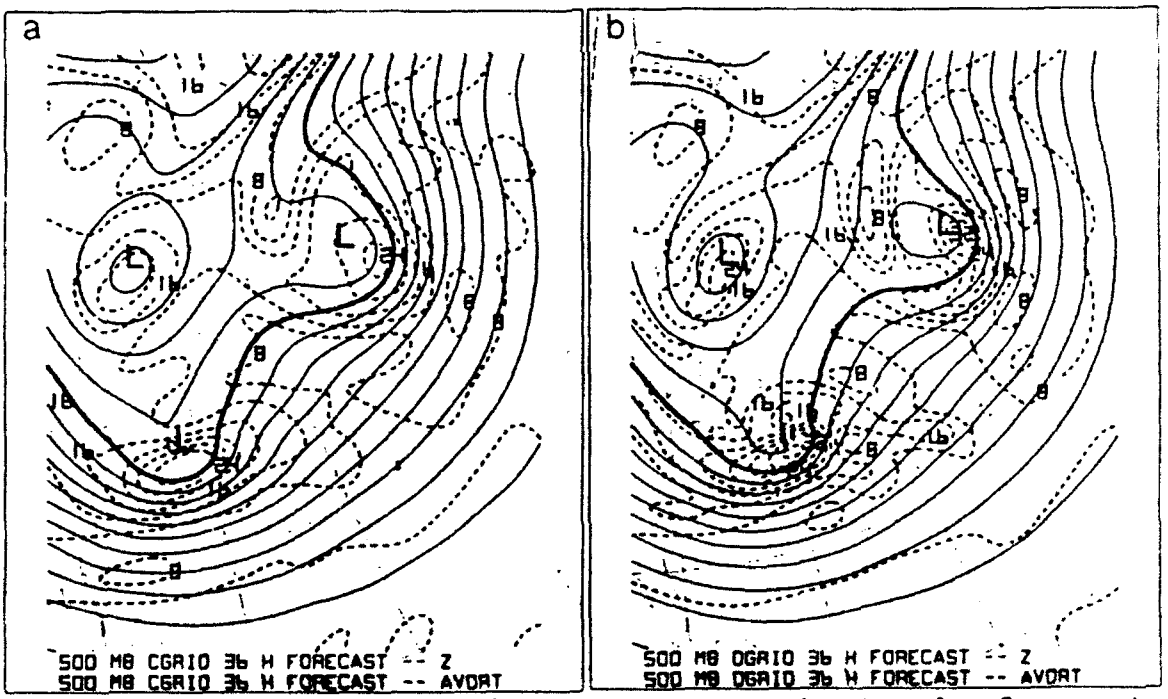

Figure 4.10. As in Fig. 4.6, except 36 h forecast, verification time 12Z/04.

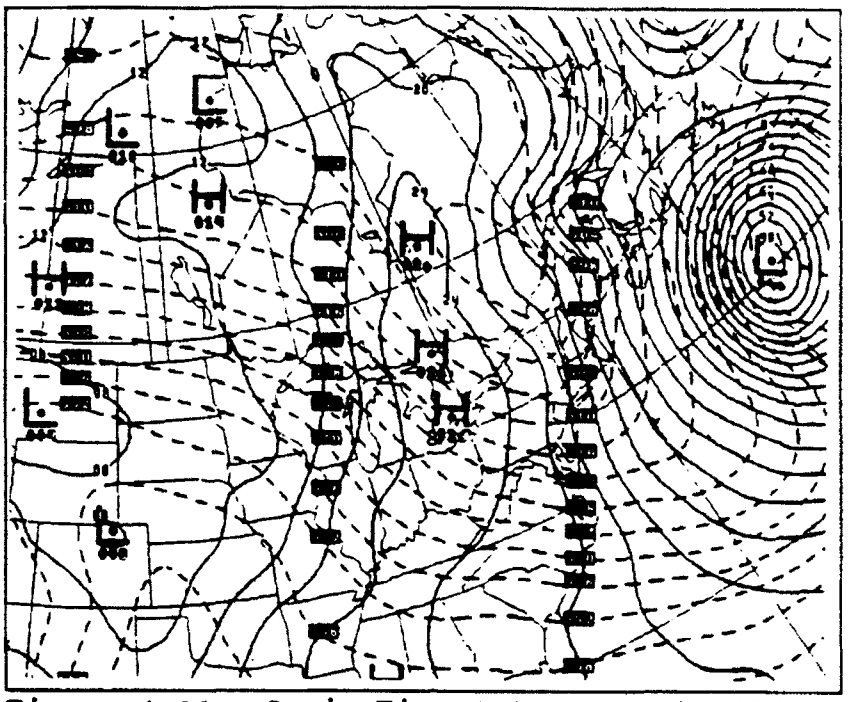

Figure 4.11a. As in Fig. 4.3a, except 00Z/05.

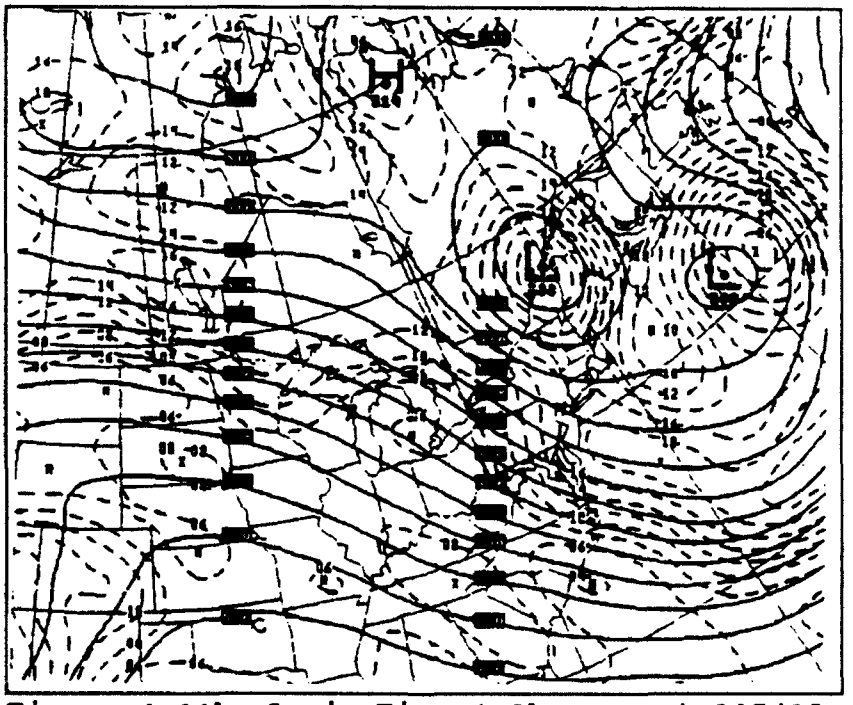

Figure 4.11b. As in Fig. 4.3b, except 00Z/05.

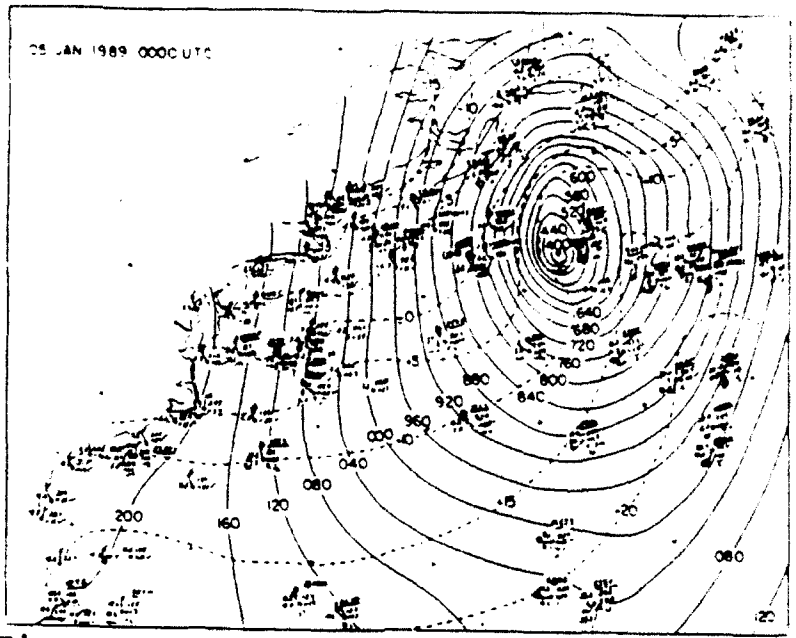

Figure 4.12a. As in Fig. 4.4a, except 00Z/05.

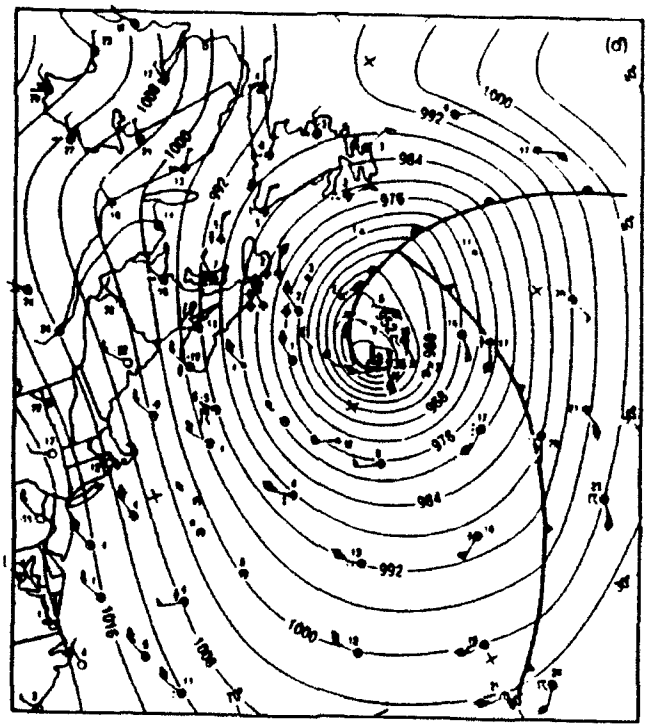

Figure 4.12b. As in Fig. 4.8b, except 00Z/05.

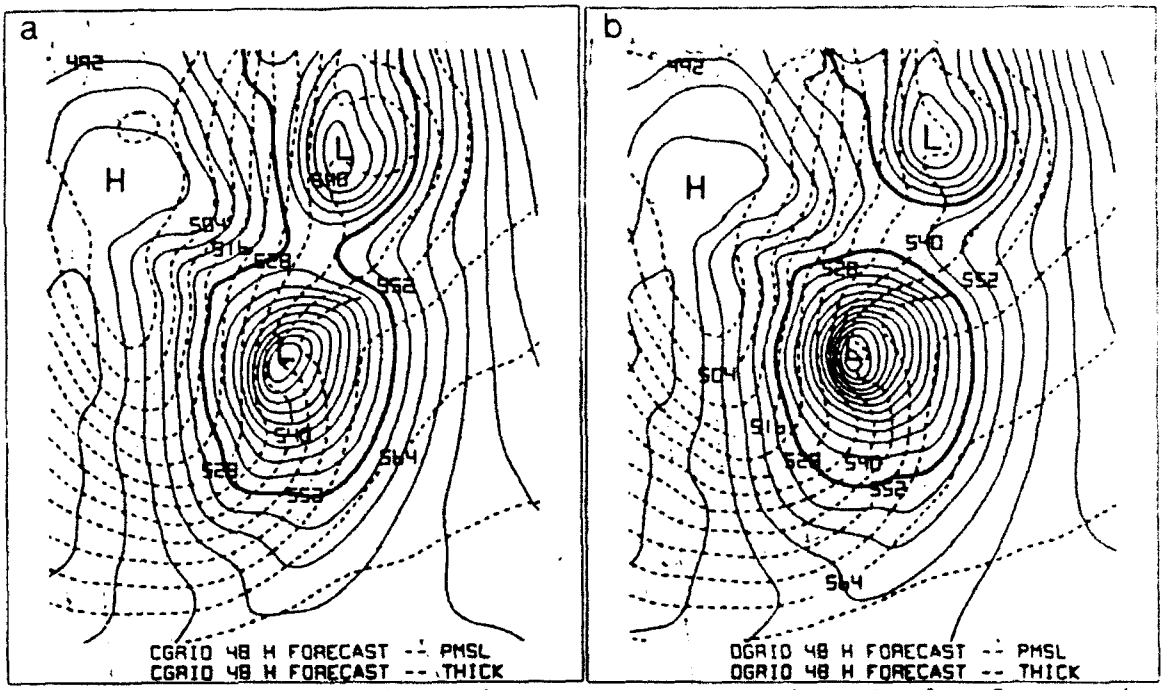

Figure 4.13. As in Fig. 4.5, except 48 h forecast, verification time 00Z/05.

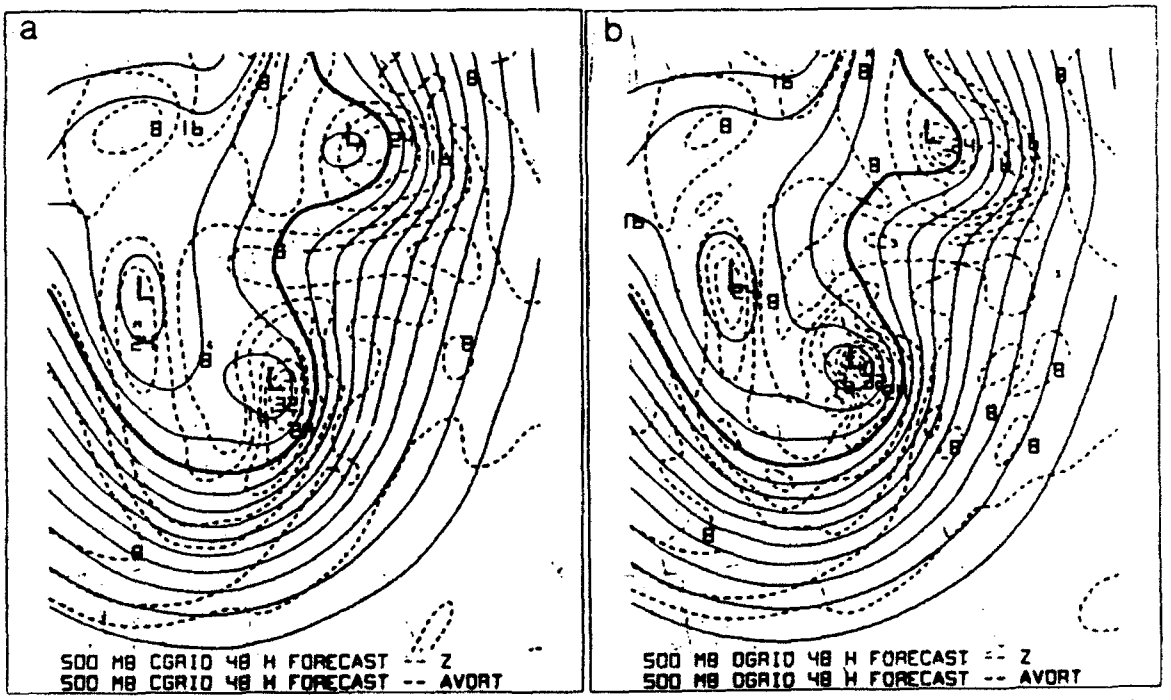

Figure 4.14. As in Fig. 4.6, except 36 h forecast, verification time 00Z/05.

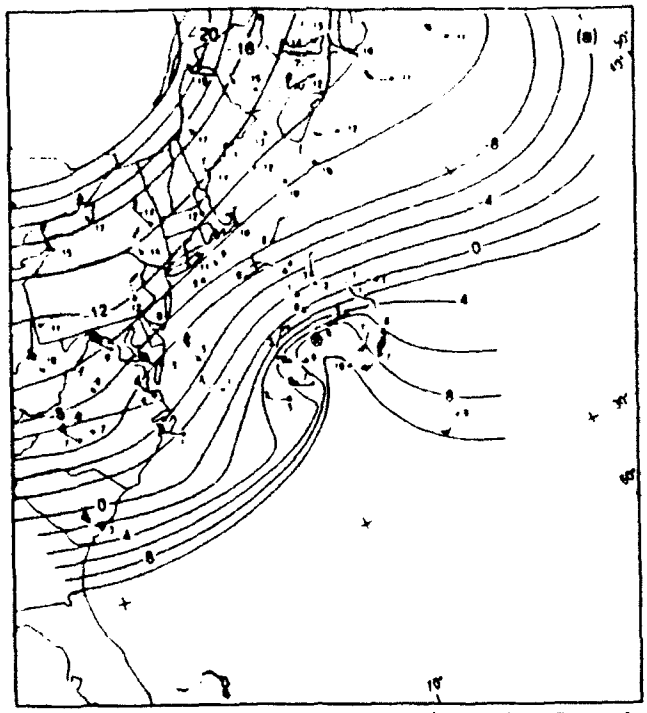

Figure 4.15. NS analysis of 850 mb temperature, 2°C increment; at 06Z/04.

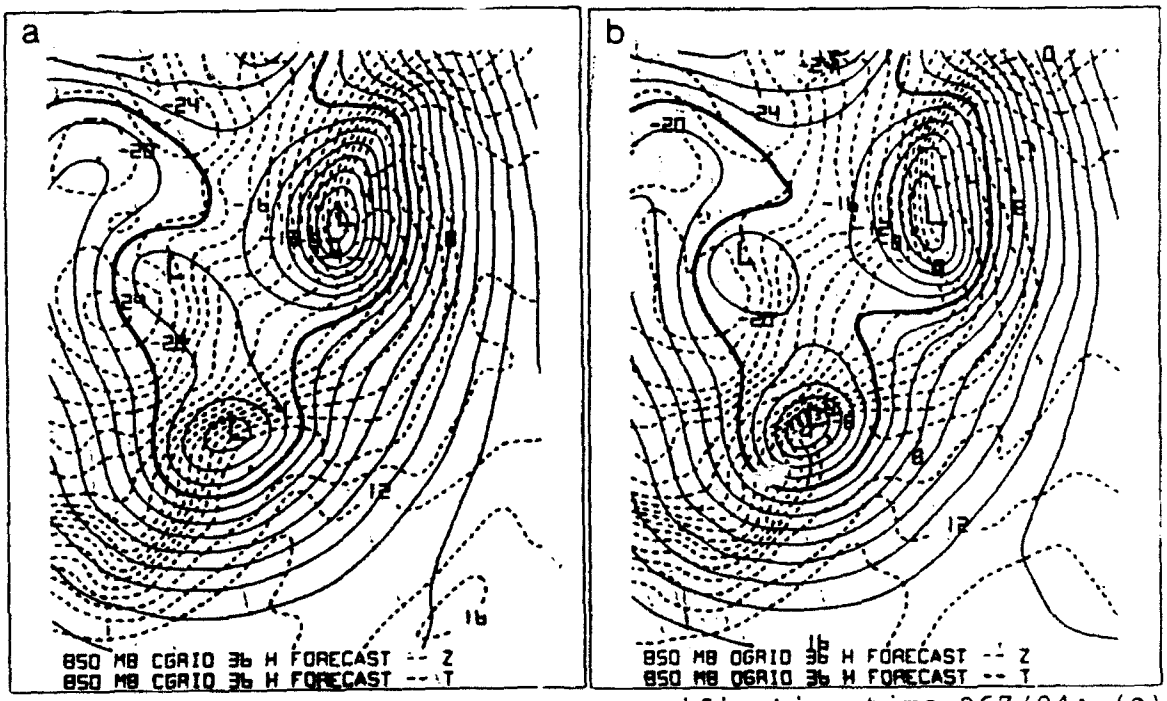

Figure 4.16. NGM 36 h forecast, verification time 06Z/04: (a) C-grid: 850 mb heights, 3 dm increment (129 dm bold contour) and 850 mb temperature, 2°C increment; (b) D-grid: as in (a).

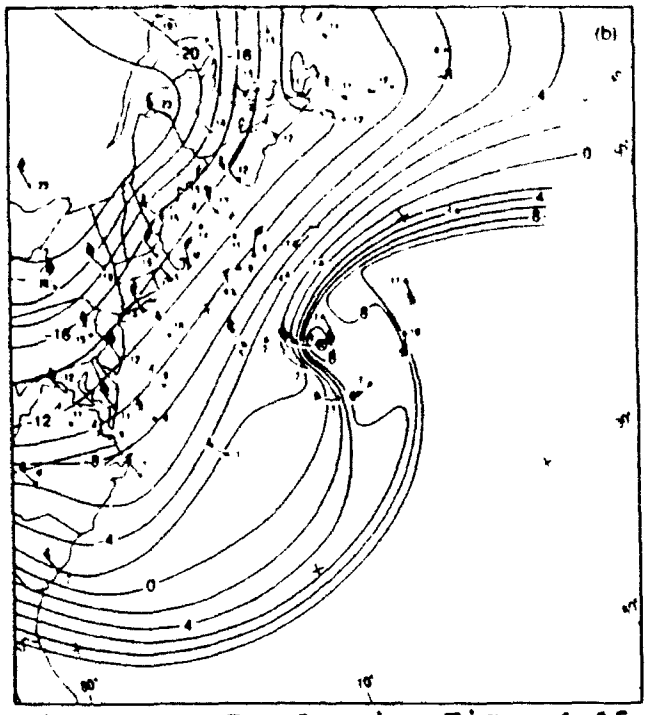

Figure 4.17. As in Fig. 4.15, except 12Z/04.

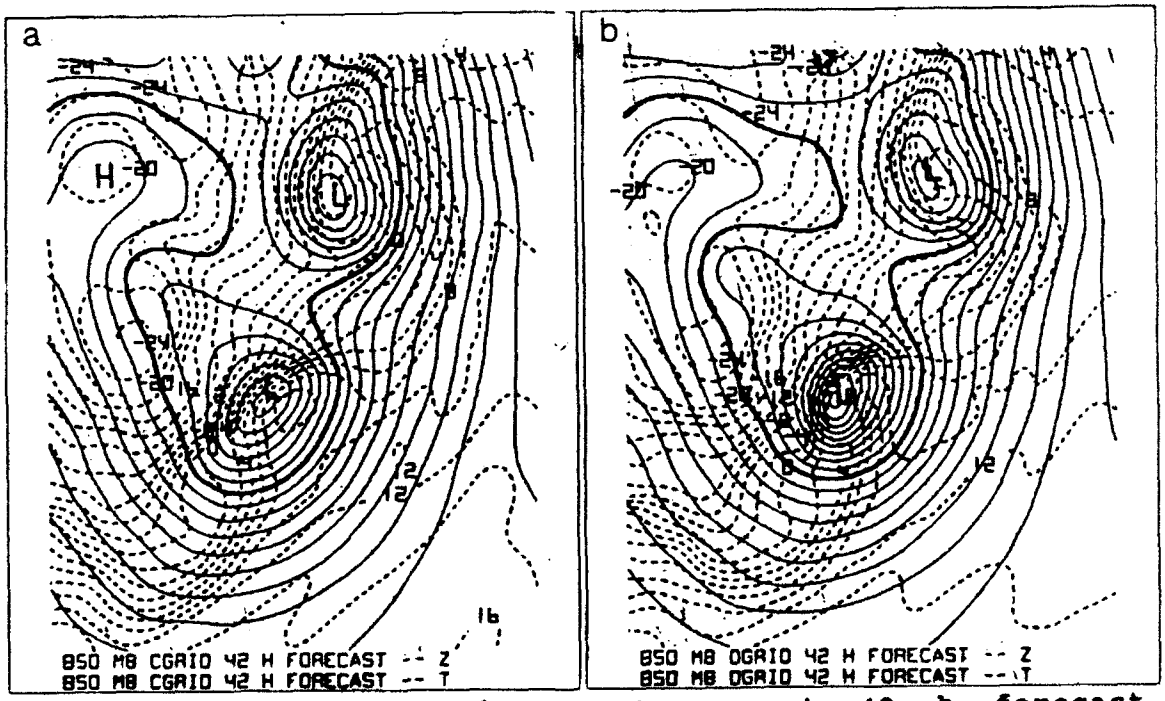

Figure 4.18. As in Fig. 4.16, except 42 h forecast, verification time 12Z/04.

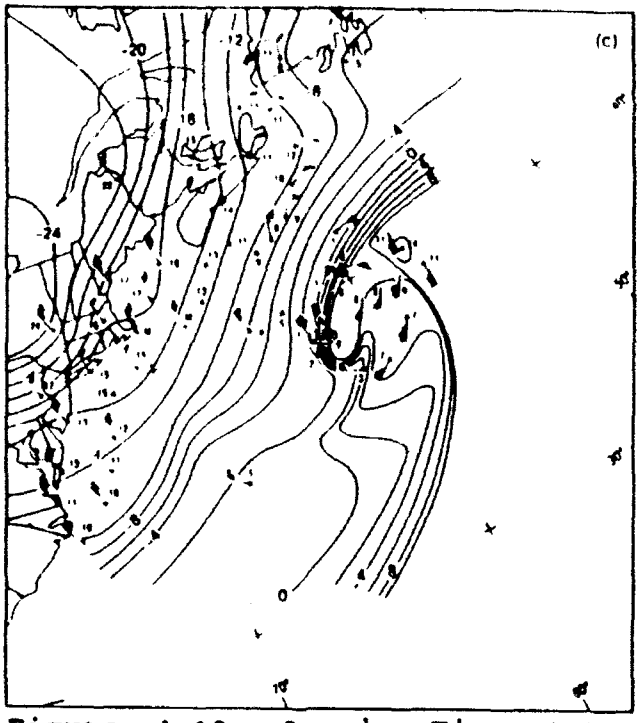

Figure 4.19. As in Fig. 4.15, except 18Z/04.

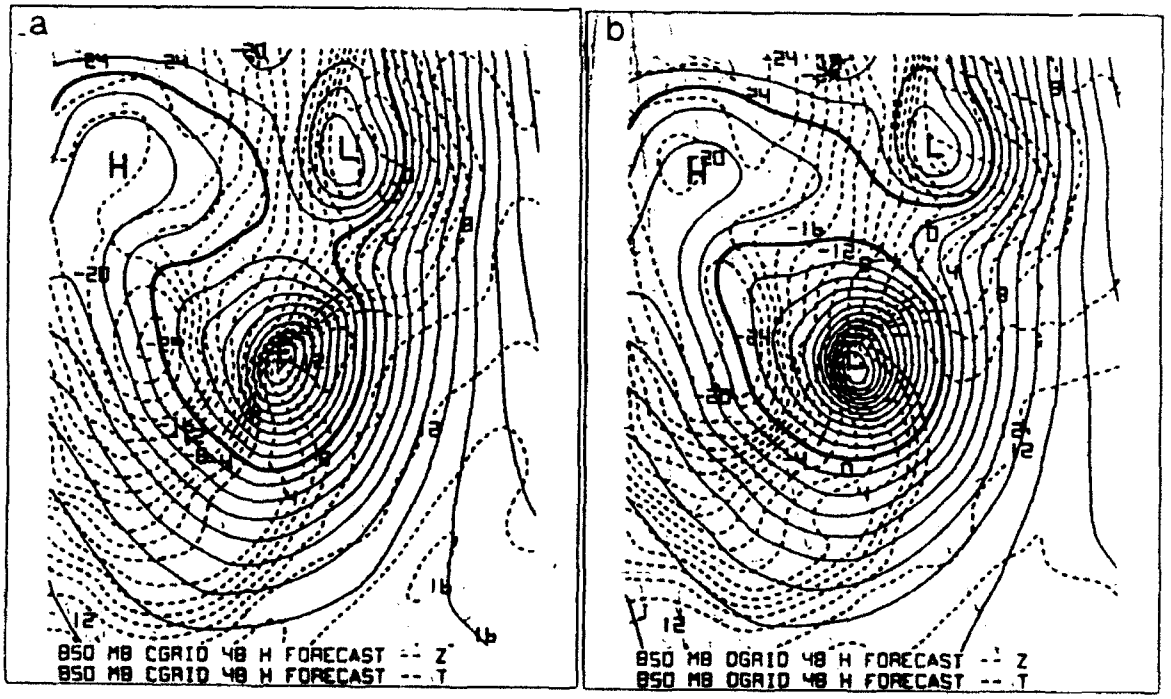

Figure 4.20. As in Fig. 4.16, except 48 h forecast, verification time 18Z/04.

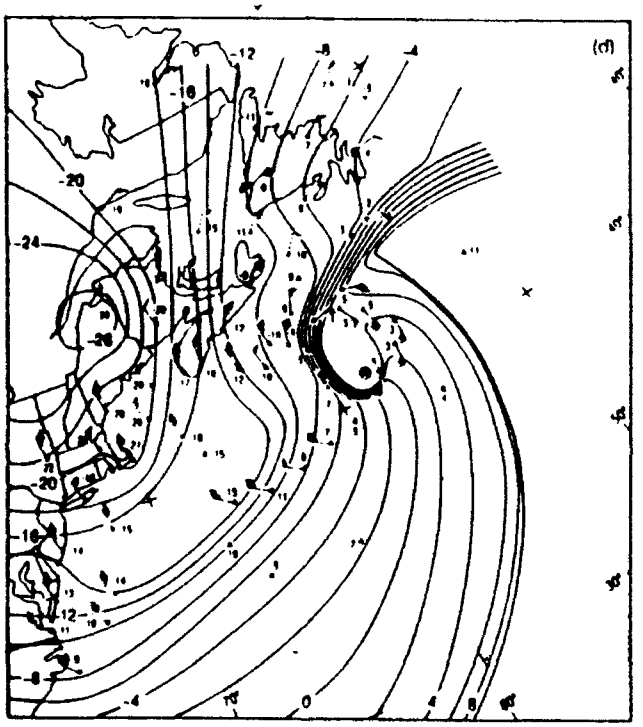

Figure 4.21. As in Fig. 4.15, except 00Z/05.

V. DIAGNOSTIC TECHNIQUES

To examine the influence of resolution on frontal dynamics and structure, psi-vector methodology is applied to diagnose vertical circulations as described by Keyser et al. (1989), and Loughe (1992). The theory underlying the technique as well as the procedures used in solving the equations are presented in this section. The first part of this section details the solution and statistics for the vertical circulation, whereas the second part focuses on the vertical motion calculation.

A. VERTICAL CIRCULATION COMPUTATION

In assuming f-plane geometry in isobaric coordinates, the geostrophic wind $\vec{V}_g$ is nondivergent, that is $\nabla \cdot \vec{V}_g \equiv 0$. The resulting ageostrophic wind can then be partitioned into divergent $\vec{V}_{agd}$ and rotational $\vec{V}_{agr}$ components (Helmholtz partitioning) by solving for the streamfunction ψ_r associated with the ageostrophic vorticity ζ_{ag} and the velocity potential χ_d associated with the ageostrophic (total) divergence $\nabla \cdot \vec{V}_{ag}$ (Lynch 1988). The equations governing this partitioning are given by

$$\zeta_{ag} = \nabla_p^2 \psi_r , \tag{5.1}$$

$$\vec{V}_{agr} = \vec{k} \times \nabla_p \psi_r \,, \tag{5.2}$$

and

$$\nabla \cdot \vec{V}_{ag} = \nabla_p^2 \chi_d \,, \tag{5.3}$$

$$\vec{V}_{agd} = \nabla \chi_d \,. \tag{5.4}$$

Using the divergent component of the ageostrophic wind to define the vertical circulation eliminates the possibility of internal cancellation between vertical velocity components in the cross- and along-front planes (Keyser et al. 1989). When the rotational ageostrophic wind component is included, the vertical integral of the horizontal mass flux for the circulations in the cross- and along-front planes may not necessarily vanish, and subsequently the vertical motion components in these planes can be large in magnitude and of opposite signs.

However, for a limited-area domain, the partitioning of the wind into rotational and divergent components is not unique, but rather depends on the boundary conditions for ψ_r and χ_d (Lynch 1989). The three-component partitioning proposed by Lynch (1989) is therefore employed. In this method, a harmonic component is computed in addition to the usual rotational and divergent components in such a way as to maintain the orthogonality of the three components and at the same time minimize the rotational and divergent components of kinetic energy.

Minimizing the rotational and divergent components of kinetic energy results when boundary values of zero are assigned in computing ψ_r and χ_d (Lynch 1989). Here, relaxation is used to obtain the solutions in the interior of the domain from (5.1) and (5.3), respectively, given values of ζ_{ag} and $\nabla \cdot \vec{V}_{ag}$. The rotational and divergent ageostrophic wind components are then computed from (5.2) and (5.4) using second-order centered finite differencing in the interior and one-sided differencing along the boundary, the same numerics as used earlier to compute the vorticity and divergence of the ageostrophic wind.

In this three-component partitioning, boundary effects are isolated in the harmonic component of the ageostrophic wind, $\vec{V}_{agh}$, which is both irrotational and nondivergent. This harmonic ageostrophic wind can be expressed in terms of either velocity potential or streamfunction (Lynch 1989), such that

$$\vec{V}_{agh} = \nabla_p \chi_h , \tag{5.5a}$$

$$\vec{V}_{agh} = k \times \nabla_p \psi_h , \tag{5.5b}$$

where

$$\nabla_p^2 \chi_h = 0 , \tag{5.6a}$$

$$\nabla_p^2 \psi_h = 0 . \tag{5.6b}$$

With a zero boundary condition used in computing χ_d and ψ_r, the normal and tangential ageostrophic wind components on the boundaries (Lynch 1989) are given by

$$v_{agn} = \vec{n} \cdot \vec{V}_{ag} = \frac{\partial \chi_d}{\partial n} + \left(-\frac{\partial \psi_h}{\partial s} + \frac{\partial \chi_h}{\partial n} \right), \qquad (5.7a)$$

$$v_{ags} = \vec{s} \cdot \vec{V}_{ag} = \frac{\partial \psi_r}{\partial n} + \left(\frac{\partial \psi_h}{\partial n} + \frac{\partial \chi_h}{\partial s} \right). \qquad (5.7b)$$

The harmonic ageostrophic wind $\vec{V}_{agh}$ can therefore be computed from either χ_h or ψ_h by solving either equations (5.7a) or (5.7b) for the boundary winds, thus allowing four possible methods.

The harmonic ageostrophic wind for this study was solved in terms of the velocity potential from (5.6a) with boundary values determined from (5.7b), corresponding to method 7 in Lynch (1989) and method 4 in Loughe (1992). As described by Loughe (1992), there is a need to first adjust the normal derivative $\partial \psi_r / \partial n$, in order for its line integral to match the domain averaged vorticity, via Stokes' theorem and (5.7b)

$$\iint \zeta_{ag} \, dx \, dy = \oint \vec{V}_{ags} ds = \oint \left(\frac{\partial \psi_r}{\partial n} + \frac{\partial \psi_h}{\partial n} + \frac{\partial \chi_h}{\partial s} \right) ds \, . \qquad (5.8)$$

Since the vorticity of the harmonic ageostrophic wind is zero, then $\oint (\partial \psi_h / \partial n) \, ds = 0$. Furthermore, $\oint (\partial \chi_h / \partial s) \, ds = 0$ by

definition for a line integral over a closed curve. Therefore the integral constraint that $\partial\psi_r / \partial n$ must satisfy is given by

$$\iint \zeta_{ag}\, dx\, dy = \oint \frac{\partial \psi_r}{\partial n}\, ds\,. \tag{5.9}$$

In order to meet this constraint, $\partial\psi_r / \partial n$ is modified by the constant c_ζ defined from

$$\iint \zeta_{ag}\, dx\, dy = \oint \left(\frac{\partial \psi_r}{\partial n} - c_\zeta \right) ds = \oint \frac{\partial \psi_r^*}{\partial n}\, ds\,, \tag{5.10a}$$

such that

$$c_\zeta \equiv \frac{\left(\oint \frac{\partial \psi_r}{\partial n}\, ds - \iint \zeta_{ag}\, dx\, dy \right)}{\oint ds}\,. \tag{5.10b}$$

The adjusted quantity is indicated by an asterisk. A second constraint is also implied by (5.8) to ensure that the line integral of the component of wind tangential to the boundary is consistent with the previous adjustment. This constraint can be written as

$$\oint (v_{ags} - c_s)\, ds = \oint \vec{V}_{ags}^{\,*}\, ds = \oint \frac{\partial \psi_r^*}{\partial n}\, ds\,, \tag{5.11a}$$

where

$$c_s = \frac{\oint v_{ags}\, ds - \oint \left(\frac{\partial \psi_r^*}{\partial n} \right) ds}{\oint ds} \,. \qquad (5.11b)$$

Assuming $\psi_h = 0$ along the boundary implies $\partial \psi_h / \partial n = 0$ since $\nabla_p^2 \psi_h = 0$ by definition. The Dirichlet boundary conditions for χ_h are determined from (5.7b) using adjusted values, such that

$$\frac{\partial \chi_h}{\partial s} = v_{ags}^* - \frac{\partial \psi_r^*}{\partial n} \,. \qquad (5.12)$$

Integrating (5.12) yields the boundary values for χ_h

$$\chi_h(s) = \int_0^s \left(v_{ags}^* - \frac{\partial \psi_r^*}{\partial n} \right) ds \,.$$

After the boundary values are determined, $\nabla_p^2 \chi_h = 0$ is solved in the interior of the domain using relaxation techniques, and $\vec{V}_{agh}$ is calculated from (5.5a).

To verify the accuracy of the partitioning of the ageostrophic wind, the root-mean-square differences (RMSD) between the original ageostrophic wind and the sum of the partitioned components are calculated and displayed in Figs. 5.1a,b and 5.2a,b. For both the C- and D-grid, peaks in RMSD occurred near the surface and near 350 mb, with RMSD values

everywhere less than 1 m s^{-1} and averaging 0.69 m s^{-1}. Only small vertical and temporal variations in RMSD are present. This exceeded the partitioning accuracy of Loughe (1992) for the Presidents' Day Storm of 1979, which had a minimum RMSD of 1.07 m s^{-1}. Note that an unstaggered grid was used in these calculations; a staggered grid would yield an exact recovery of the total ageostrophic wind from the partitioned components, and Figures 5.1 and 5.2 would yield zero (Loughe, personal communication).

Since the vertical motion ω is associated only with $\vec{V}_{agd}$ and not $\vec{V}_{agr}$ by virtue of continuity, an alternate definition of the velocity potential χ can be used, facilitating examination of the vertical circulation. The Eliassen (1984) form of χ, here denoted χ_e, is defined in terms of ω as

$$\omega = -\nabla_p^2 \chi_e . \tag{5.13}$$

By continuity,

$$\nabla \cdot \vec{V}_{agd} = -\frac{\partial \omega}{\partial p} . \tag{5.14}$$

Therefore, substituting (5.13) in for ω in (5.14) and reducing yields

$$\nabla \cdot \vec{V}_{agd} = \frac{\partial}{\partial p}\left(\nabla_p^2 \chi_e\right), \tag{5.15a}$$

which can be rewritten as

$$\nabla \cdot \vec{V}_{agd} = \nabla \cdot \nabla \left(\frac{\partial \chi_e}{\partial p} \right) . \qquad (5.15b)$$

It can be seen from this expression that the divergent ageostrophic wind can be defined in terms of χ_e as

$$\vec{V}_{agd} = \nabla_p \frac{\partial \chi_e}{\partial p} . \qquad (5.15c)$$

Note that χ_e and χ_d are related through the expression

$$\chi_d = \frac{\partial \chi_e}{\partial p} . \qquad (5.16)$$

Keyser et al. (1989) proposed describing the vertical circulation in terms of the vector $\vec{\Psi}$, defined as

$$\vec{\Psi} = - \nabla_p \chi_e . \qquad (5.17)$$

The divergent ageostrophic wind and the vertical motion are then rewritten in terms of $\vec{\Psi}$ as

$$\vec{V}_{agd} = - \frac{\partial \vec{\Psi}}{\partial p} , \qquad (5.18a)$$

and

$$\omega = \nabla_p \cdot \vec{\Psi} . \qquad (5.18b)$$

Since the vertical circulation is now written as a vector function, it can be projected onto any arbitrary plane by projecting $\vec{\Psi}$ onto that plane. For example, orientating a coordinate system parallel to a front yields along-front (n-

direction) and cross-front (s-direction) components of the vertical circulation, the latter of which can be compared to traditional 2-D frontal theory. The vertical circulation in the cross-front plane can then be expressed in the (n,p) plane from

$$v_{agdn} = - \frac{\partial \psi_n}{\partial p} , \qquad (5.19a)$$

and

$$\omega_n = \frac{\partial \psi_n}{\partial n} , \qquad (5.19b)$$

while the along-front components in the (s,p) plane are given by

$$v_{agds} = - \frac{\partial \psi_s}{\partial p} , \qquad (5.20a)$$

$$\omega_s = \frac{\partial \psi_s}{\partial s} . \qquad (5.20b)$$

For the calculation presented in this thesis, the velocity potential χ_e is calculated from the adjusted kinematic vertical motion ω by (5.13) using relaxation, as described before. The vertical circulation is calculated from χ_e in terms of the x and y components of $\vec{\psi}$, according to (5.17). The partial derivatives of $\vec{\psi}$ can then be used to compute $\vec{V}_{agd}$ and ω from (5.18). In addition, the vertical circulation can

be projected onto any arbitrary plane by first projecting $\vec{\Psi}$ onto that plane, then using (5.20) to compute $\vec{V}_{agds}$ and ω_s. Note that isopleths of $\vec{\Psi}_s$ describe streamlines for the vertical circulation in a cross-section.

Figures 5.3a,b and 5.4a,b show RMSD between the divergent ageostrophic winds computed from the horizontal divergence through χ_d and those computed from the vertical motion through $\vec{\Psi}$. A peak in the differences occurs above 300 mb with a maximum RMSD for the v-component of 0.9 m s^{-1} for the D-grid 42 h forecast. However, most RMSD values are less than 0.4 m s^{-1}. There are only slight temporal variations for these fields. Since the psi-vector technique requires a consistency between kinematic vertical motion ω and the divergent ageostrophic wind $\vec{V}_{agd}$, using the adjusted divergence along with an unstaggered grid eliminates the ability to fully recover the input ageostrophic wind. However, the RMSD values show that the recovery is very resonable.

B. VERTICAL MOTION COMPUTATION

In order to have vertical motion values which are consistent with the divergence computed on interpolated pressure surfaces, a kinematic omega calculation was performed rather than using the model-predicted values. An O'Brien (1970) adjustment was applied to remove the vertically integrated divergence, with the vertical motion constrained to

be zero at 1000 mb and 100 mb in this computation, and with both omega and divergence adjusted to maintain consistency. However, the omega adjustment process led only to small changes, as one would expect for a model-derived dataset. Figures 5.5a,b depict the mean magnitudes of the adjusted omega field for both the C- and D-grid to place the difference statistics in context. Figures 5.6a,b show that the RMSD between the adjusted and unadjusted omega increase linearly, as one would expect, for both the C- and D-grid with the D-grid differences being slightly greater. The maximum RMSD for these fields was 0.86 $\mu b\ s^{-1}$. Statistical analysis comparing the adjusted and unadjusted divergent ageostrophic winds indicates an almost constant RMSD in the vertical with slight variation in time. A maximum RMSD of .133 $m\ s^{-1}$ occurred in the C-grid 48 hr forecast (not shown). This indicates that the adjustment does not significantly change the divergent ageostrophic wind.

A comparison of adjusted omega and omega derived from Ψ, provides an estimate of numerical error for these calculations. The maximum RMSD occurs at mid-levels with peak values of 0.66 $\mu b\ s^{-1}$ for the C-grid and 0.72 $\mu b\ s^{-1}$ for the D-grid (Fig. 5.7a,b), comparable to the RMSD associated with the adjustment process. Furthermore, comparison of the adjusted kinematic omega with the model-predicted omega reveals small differences as well, which were primarily linear

with a maximum RMSD of 0.80 $\mu b\ s^{-1}$ near the surface (not shown).

Quasi-geostrophic (QG) vertical motions were also computed for comparison purposes using the Q-vector form (Hoskins et al. 1978; Hoskins and Pedder 1980). The QG vertical motion is calculated using three-dimensional simultaneous relaxation techniques with boundary conditions set to zero. As seen in Figures 5.8a,b, the RMSD between the adjusted kinematic omega and the QG omega are significantly larger than previous fields, with greater temporal fluctuations. Both the C-grid and the D-grid exhibit a double peak RMSD pattern with maxima at 900 mb and 450 mb as high as 5 $\mu b\ s^{-1}$.

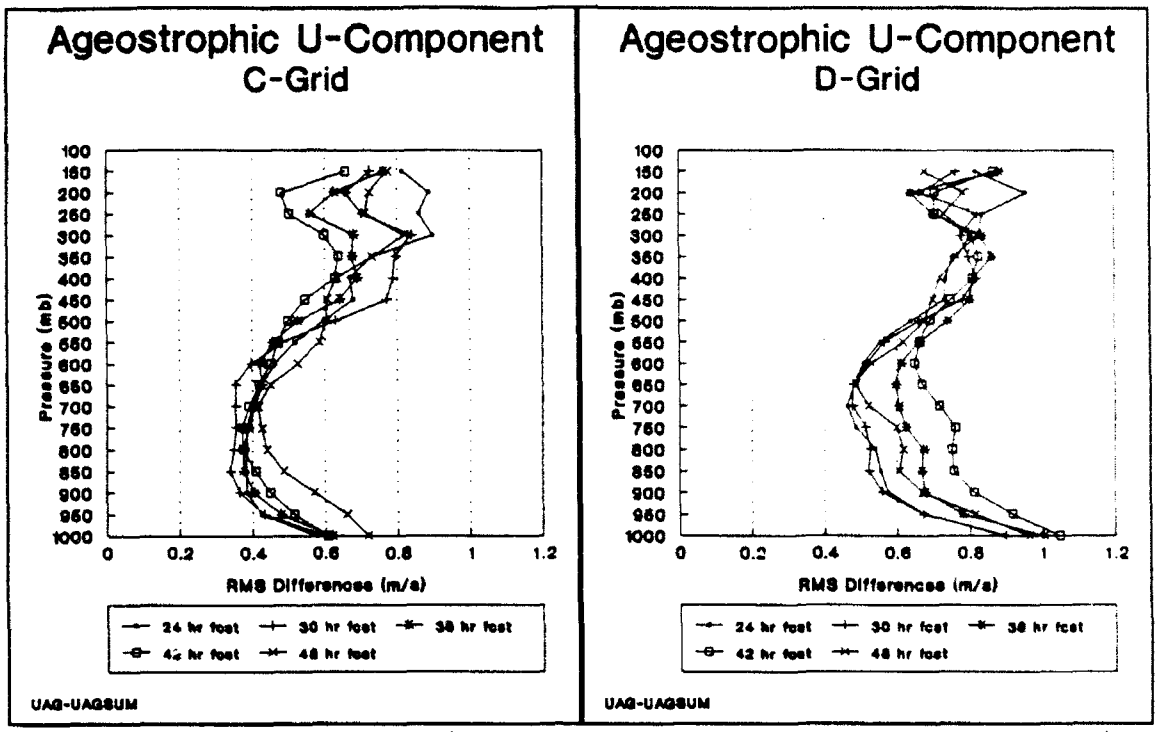

Figure 5.1. Ageostrophic Wind U-component RMSD:(a) C-grid: RMSD between original ageostrophic wind and sum of partioned components ($\vec{V}_{agd} + \vec{V}_{agr} + \vec{V}_{agh}$); (b) D-grid: as in (a)

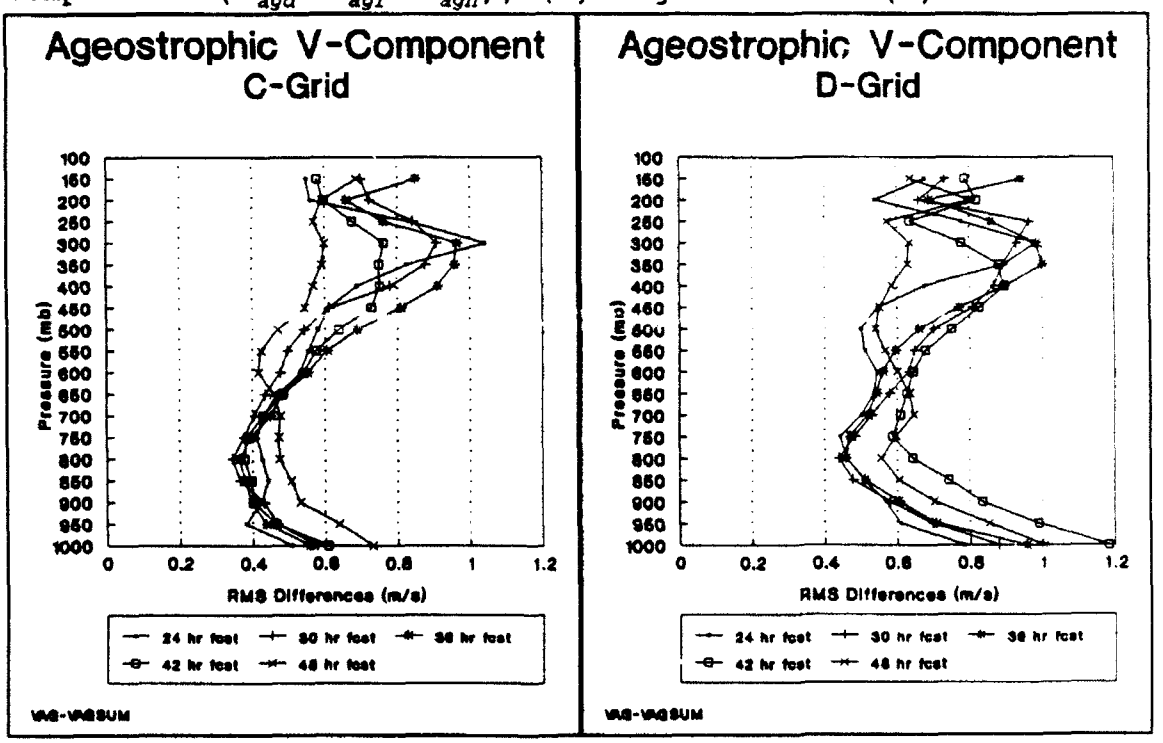

Figure 5.2. As in Fig. 5.1, except V-component

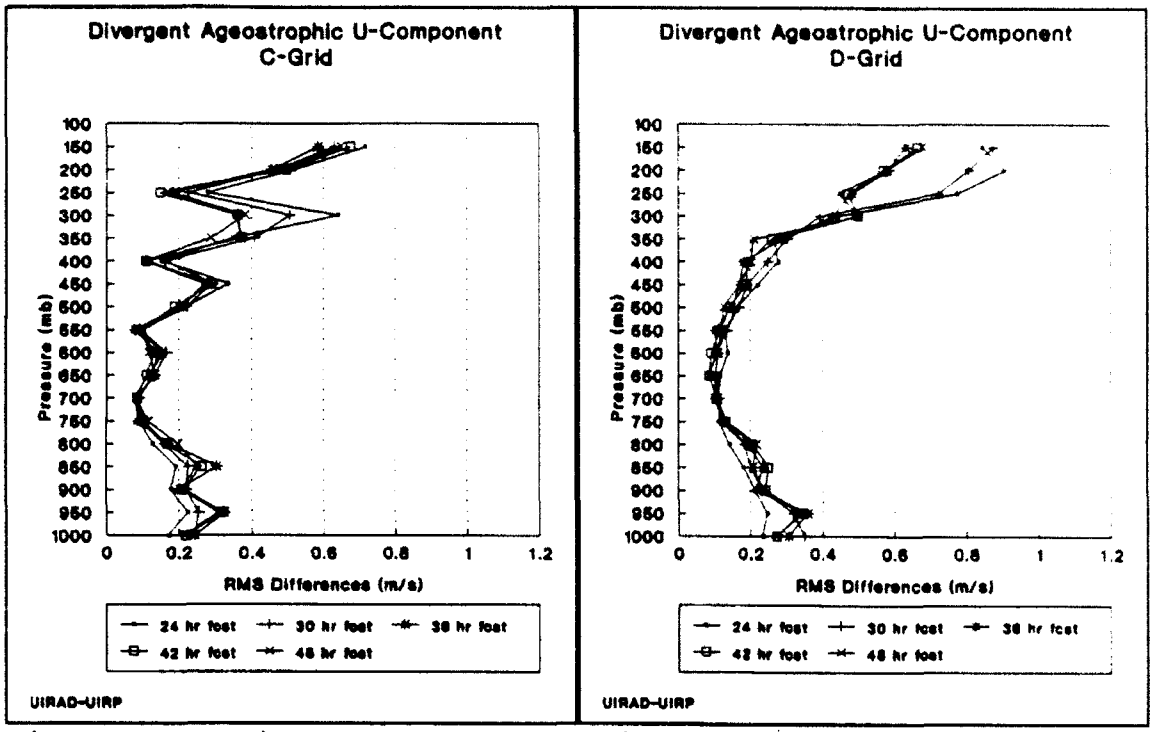

Figure 5.3. Divergent Ageostrophic Wind U-component RMSD: (a) C-grid: RMSD between divergent ageostrophic wind calculated from χ_d and those computed from Ψ; (b) D-grid: as in (a)

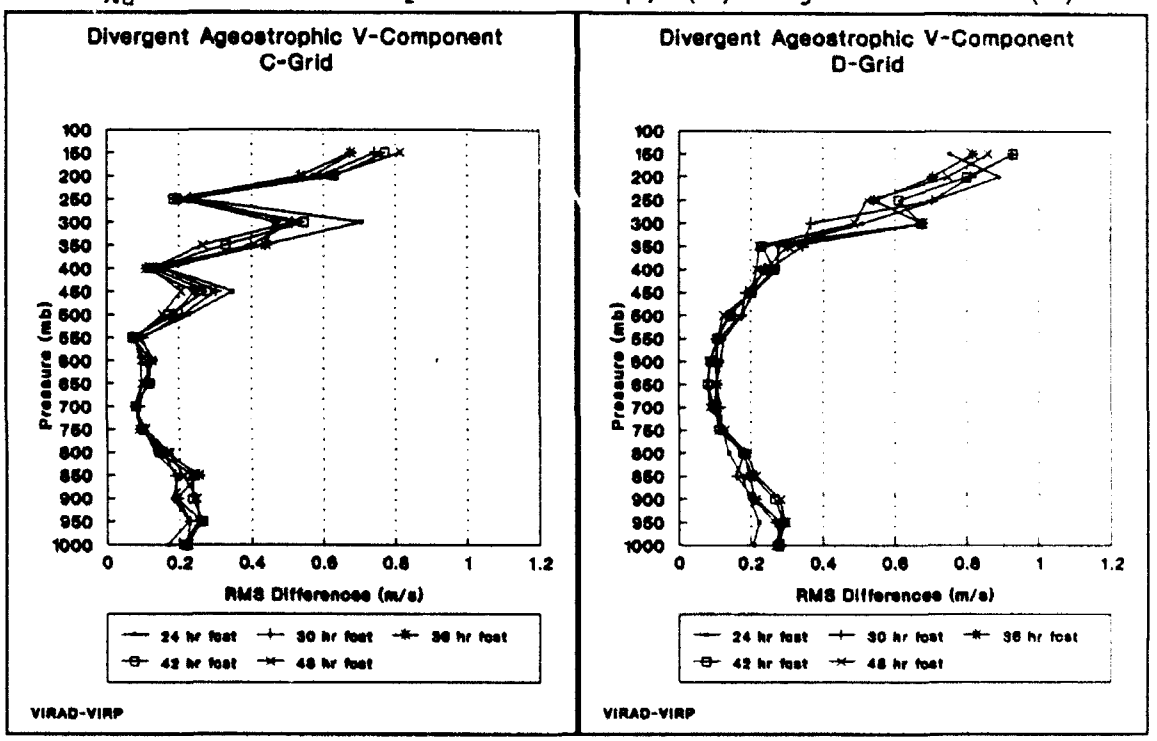

Figure 5.4. As in Fig. 5.3, except V-component

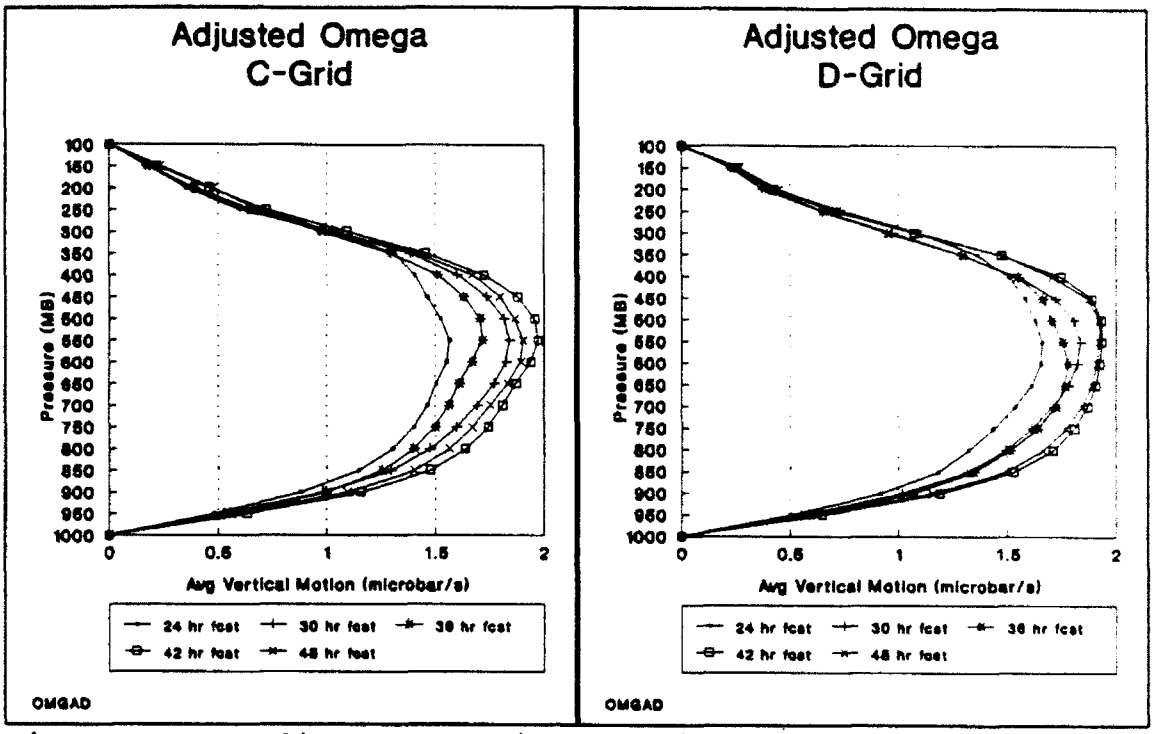

Figure 5.5. Adjusted vertical motion:(a) C-grid: Absolute avergage ω for NGM forecasts; (b) D-grid: as in (a)

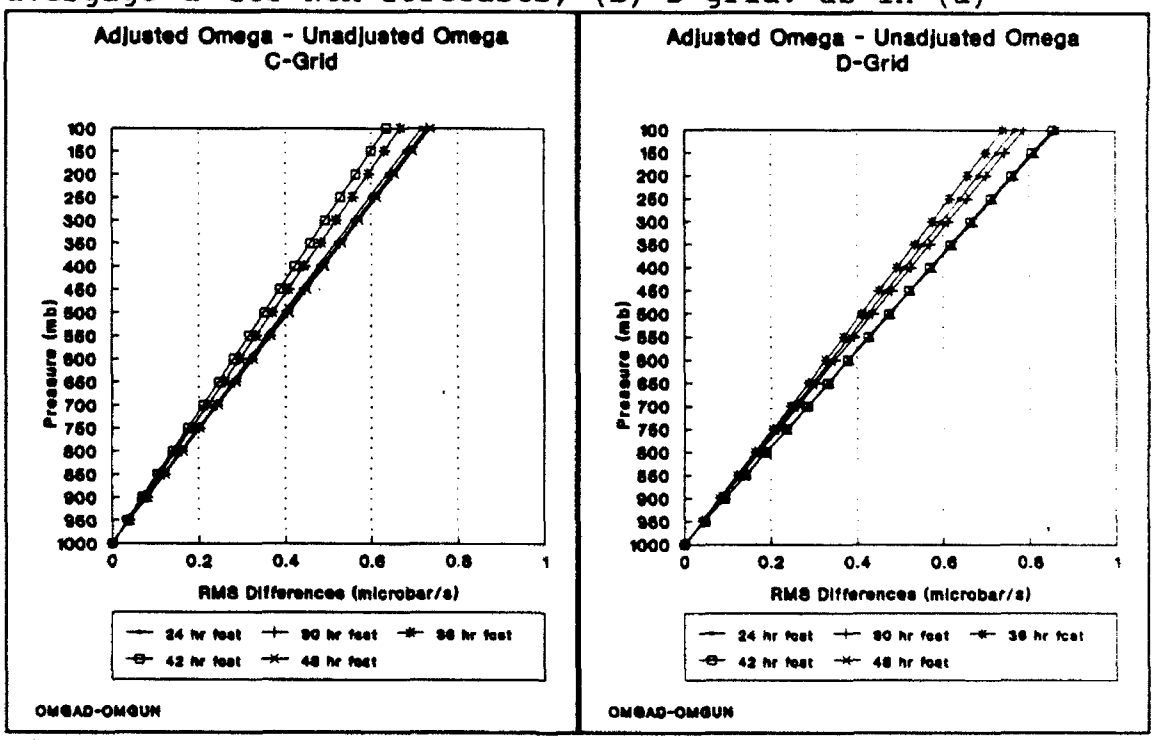

Figure 5.6. Vertical motion RMSD:(a) C-grid: RMSD between adjusted ω and unadjusted ω;(b) D-grid: As in (a)

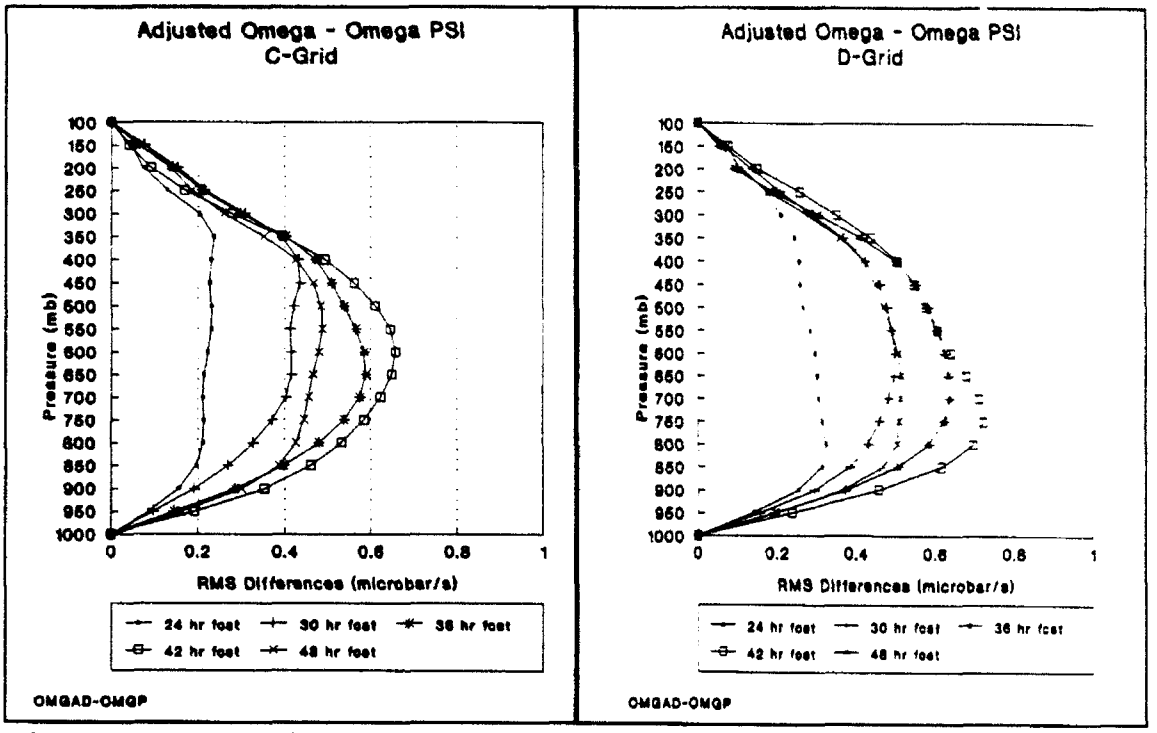

Figure 5.7. As in Fig 5.6, except RMSD between adjusted ω and ω derived from $\tilde{\psi}$

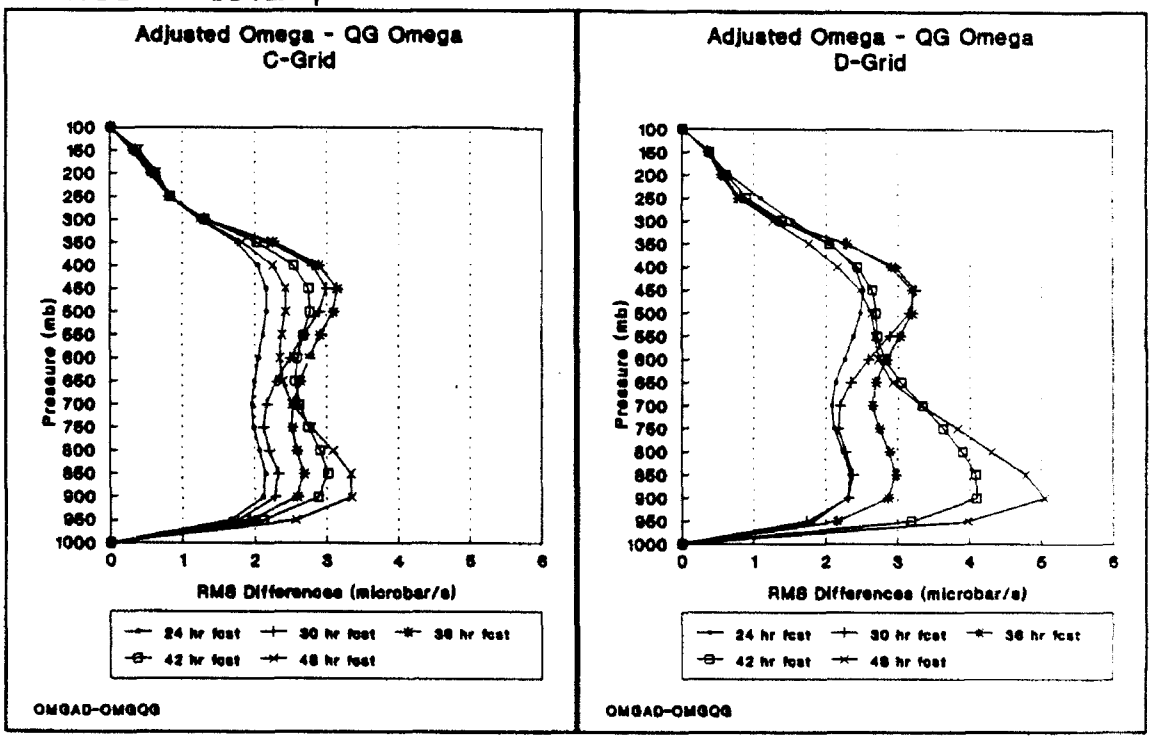

Figure 5.8. As in Fig 5.7, except RMSD between adjusted ω and Quasi-Geostrophic ω

VI. RESULTS

This chapter will examine the interaction of propagating jet streaks with the low-level cyclone as a possible contributing mechanism for explosive cyclogenesis in the IOP-4 storm. As seen previously, jet streak dynamics can influence the upper-level divergence and thus can play an important role in the intensification of surface cyclones. NGM C- and D-grid 300 mb forecasts are therefore compared for jet streak structure differences. Additionally, two vertical cross-sections are used to examine the contribution of longitudinal and transverse ageostrophic circulations to the vertical motion, in order to gain insight into the greater low-level spin-up in the D-grid forecast. The approximate position of the cross-sections are indicated on the 300 mb plots of height and windspeed. Each cross-section plot is labeled with the latitudes and longitudes of the end points. The distance between neighboring tick marks along the bottom corresponds to the grid length on the NGM C-grid; areas of the cross-section below ground are shaded. The model terrain over the Eastern United States appears raised in the shaded region. In addition, when the surface low pressure center is depicted over the ocean it also appear raised, since it has a lower pressure. The cross-section labeled JT1, is approximately

parallel to the flow at the trough and ridge lines, depicting the longitudinal ageostrophic circulations. The cross-section labeled JT2, is perpendicular to the flow (and to JT1), intersects the low-level vertical motion ascent maximum near the surface cyclone center, and passes through the exit region of the jet streak in the base of the trough and the entrance region of the jet streak that forms in the ridge. This cross-section portrays the transverse ageostrophic circulations.

A. 24 h FORECAST

At 00Z/04, the IOP-4 surface cyclone was located over North Carolina and Virginia and had a central pressure of 998 in both the C- and D-grid forecasts. A broad jet streak southwest of the surface low center with wind speeds in excess of 70 m s^{-1} at 300 mb is evident in both the C- and D-grid forecasts (Figs. 6.1a,b). However, the D-grid depicts a slightly weaker maximum value as indicated by the smaller area enclosed by the 70 m s^{-1} isotach, but a more elongated 65 m s^{-1} isotach that extends further east than that of the C-grid. The NGM 00Z/04 analysis has a similar jet structure, however the 70 m s^{-1} isotach is located further west than that of the C- or D-grid (Fig. 6.1c). Note that the NGM analysis was performed on the C-grid and interpolated to the LFM grid with a resolution of 190.5 km at 60° N. This analysis, therefore, suffers from resolution limitations itself, in addition to having sparse data over the North Atlantic.

The 300 mb ageostrophic wind field reveals that the upper-level trough west of the surface low center is characterized by substantial subgeostrophic flow in both forecasts (Fig. 6.2a,b). Transverse ageostrophic winds are directed toward higher geopotential heights in the jet-exit region for both the C- and D-grid, however with a greater magnitude in the D-grid. Figures 6.3a,b and 6.4a,b portray the divergent and rotational components of the total ageostrophic wind. Note that the scaling for the rotational component is double that of the divergent component. The ageostrophic wind south of the surface low center is both divergent and rotational for both the C- and D-grid forecasts. The harmonic ageostrophic component (not shown) is relatively small south of the surface low center.

Figure 6.5a,b is a depiction of the low-level ascent area in which the cross-sections, JT1 and JT2, will pass just south of the maximum ascent region. Both the C- and D-grid forecasts indicated a region of ascent over the surface cyclone, however only the D-grid depicts a secondary area of ascent to its southeast, off the coast of North Carolina. This secondary ascent area may be associated with secondary cyclogenesis off the coast of Cape Hatteras, as indicated in the NS analysis.

The first cross section (JT2) for the 24 h forecast, intersects the low-level ascent maximum near the surface cyclone center (Figs. 6.5a,b) and is approximately

perpendicular to the jet streak (Figs. 6.1a,b). Figures 6.6a,b depict cross-sections of potential temperature θ, and the component of the total wind normal to the cross-section V_n with the cyclone center, marked by a raised surface in the shaded area and a zero value for V_n toward the middle of the figures. The jet maximum occurs at approximately 200 mb for both the C- and D-grid with a greater windspeed maximum in the C-grid. Both figures reveal stronger tropospheric stability and a lower tropopause to the north of the surface low center with weaker stability and a higher tropopause south of the surface low center. The sloping isentropes in most of the troposphere implies large-scale baroclinicity, although no fronts are apparent.

Figures 6.7a,b depict the vertical circulation in terms of streamlines of the along-plane component and vectors composed of the divergent ageostrophic wind component V_{ds} and the vertical velocity ω_s within the plane. The D-grid circulation patterns are slightly stronger than the C-grid, with a thermally direct circulation to the north and a thermally indirect circulation to the south of the surface low center in both. Weak ascent is evident over the surface low center in both the C- and D-grid forecasts (Figs. 6.8a,b).

The second cross-section (JT1) is parallel to the flow in the trough and ridge and perpendicular to cross-section JT2 (Figs. 6.9a,b). East of the surface cyclone the isentropes

are relatively flat indicative of a weak horizontal temperature gradient. The winds normal to this plane are mostly light with weak vertical shear. West of the surface low center there is evidence of stronger northerly winds and a pool of cold air at low-level indicated by the raised isentropes.

Figures 6.10a,b portray the longitudinal circulations, formed in response to the subgeostrophic flow in the upper-level trough and supergeostrophic flow in the upper-level ridge. The longitudinal circulation associated with the trough is stronger than the one associated with the ridge in both forecasts. Stronger ascent east of the surface low center is present in the D-grid forecast compared to the C-grid forecast (Figs. 6.11a,b). However, both forecasts depict relatively weak ascent maxima in both the JT1 and JT2 plane, which contributed to the slow initial deepening rate of the surface cyclone in both forecasts.

B. 30 h FORECAST

During the ensuing 6 h, the system has continued to develop with central pressures in the C- and D-grid forecasts of 991 mb and 990 mb, respectively. The structure of the 300 mb jet streak to the west-southwest of the surface low center is similar in the two forecasts (Figs. 6.12a,b). The maximum winds, in excess of 75 m s^{-1} in both, remain upstream of the cyclone center near the base of the upper-level trough.

However, the formation of a windspeed minimum east of the surface low pressure center is evident only in the D-grid forecast, which also had a slightly higher amplitude upper-level ridge. No verifying analyses are available for this forecast time. Strong subgeostrophic flow is apparent in the base of the upper-level trough in the C- and D-grid forecasts with ageostrophic winds in excess of 30 m s^{-1} (Figs. 6.13a,b). Weak transverse ageostrophic flow, characterized by a cross-contour component toward higher geopotential heights, is most apparent in the C-grid due to a better-defined jet-exit region. The ageostrophic wind in this region is both divergent and rotational, with a greater rotational component as before (Figs. 6.14a,b and Figs. 6.15a,b). The divergent ageostrophic component is both transverse and longitudinal, whereas the rotational component is primarily longitudinal. The harmonic ageostrophic component (not shown) is relatively weak throughout these regions.

Figures 6.16a,b depict an area of maximum ascent southeast of the surface low center through which the JT1 and JT2 cross-sections pass. The maximum ascent is stronger in the D-grid forecast and is also more elongated to the southwest over the cold frontal zone.

The JT2 cross-section is again oriented passing through the low level upward motion maximum (Figs. 6.16a,b) and the exit region of the jet streak (Figs. 6.12a,b). The jet

maximum is located at approximately 150 mb for the D-grid and 200 mb for the C-grid with a slightly greater magnitude in the D-grid (Figs 6.17a,b). Large-scale baroclinicity is still apparent by the sloping isentropes in most of the troposphere. North of the surface cyclone the boundary layer is well-mixed to approximately 850 mb as indicated by the nearly vertical orientation of the isentropes in this region; this is likely a result of sensible heating from the warm ocean surface to the relatively cold air behind the surface cyclone.

The D-grid forecast indicates a stronger thermally direct circulation than the C-grid with stronger ageostrophic winds as implied by the vertical gradient of ψ_s (Figs. 6.18a,b). This also produces a tighter horizontal gradient of ψ_s between the adjacent transverse circulations and so greater ascent values than in the C-grid (Figs. 6.19a,b). The thermally direct and thermally indirect circulations in both the C- and D-grid forecasts have increased in magnitude from the previous forecast, as has the ascent.

The strengthening of the southerly flow at approximately 400 mb in the C-grid and 350 mb in the D-grid, east of the surface low center, is depicted in the second cross-section (JT1) (Figs. 6.20a,b). Behind the surface low, there is evidence of strong low-level northerly flow in both the C- and D-grid forecast. A low-level pool of cold air coming off the

continent west of the surface low is depicted by the raised isentropes in both forecasts.

Figures 6.21a,b indicates the longitudinal circulation associated with the trough is stronger in this plane than the thermally direct circulation in plane JT2 and again stronger than the longitudinal circulation in the ridge. The ascent in the D-grid forecast has a maximum of approximately 10 $\mu b\ s^{-1}$ at 750 mb as compared to the C-grid forecast whose maximum is smaller and occurs at approximately 600 mb (Figs. 6.22a,b). The position and magnitude of the maximum ascent in the D-grid will cause greater spin-up of the low-level cyclone as can be inferred from $\partial\omega/\partial p$. Both the C- and D-grid forecasts depict the longitudinal circulations have strengthened from the previous forecast. In response to this, the vertical ascent has also increased from previous, especially in the D-grid whose upward motion maximum in this plane more than doubled in magnitude. The ascent maxima in JT1 are approximately equal to those in the JT2 plane, implying both curvature effects and jet streak dynamics are important.

C. 36 h FORECAST

The C-grid forecast has deepened the cyclone by 11 mb to a central pressure of 980 mb between the 30 h and 36 h forecasts, while the D-grid deepened the system by 17 mb to a central pressure of 973 mb. By this time, there are two distinct jet streaks at 300 mb in both the C- and D-grid

forecasts (Figs. 6.23a,b). The original jet streak continues to propagate eastward and remains south of the surface low center; it will hereafter be referred to as the southern jet. The new jet streak northeast of the surface low center will be referred to as the northern jet. The southern jet streak is located just upstream of the upper-level trough, with the maximum windspeed gradient to the southwest of the surface low center, with maximum wind speeds in excess of 65 m s^{-1} for both forecasts. The northern jet streak is oriented cross-contour to the upper-level ridge that is northeast of the surface low center. The D-grid northern jet streak is stronger than the C-grid, with winds in excess of 60 m s^{-1}, and is more elongated. The two jet streaks are in a favorable alignment to induce laterally interacting transverse ageostrophic circulations, which act to focus ascent in the region between the two jet streaks (previously discussed in chapter II). The NGM 12Z/04 analysis also depicts both a northern and southern jet streak, with the northern jet streak closely resembling the C-grid forecast (Fig. 6.23c). However, this jet structure is not certain, since the jet streak is almost entirely over the ocean, where data were sparse, and since the resolution of the analysis is relatively coarse.

The upper-level trough/ridge system is characterized by strong subgeostrophic flow in the trough and moderate supergeostrophic flow in the ridge for both the C- and D-grid

forecasts (Figs. 6.24a,b). As expected, the cross-contour ageostrophic flow is directed toward higher geopotential heights near the southern jet's exit region and directed toward lower geopotential heights near the northern jet's entrance region. Figures 6.25a,b and 6.26a,b indicate that the ageostrophic wind in the vicinity of the southern jet is both rotational and divergent, whereas the ageostrophic wind in the vicinity of the northern jet is predominately divergent. The harmonic ageostrophic component (not shown) is again relatively weak in these regions.

The low-level ascent maximum is now located east of the surface cyclone center in both the C- and D-grid forecasts, with a greater magnitude in the D-grid (Figs. 6.27a,b). The maximum ascent area extends eastward associated with the warm front in both forecasts, however, the D-grid forecast also shows evidence of strong vertical motion extending southwest associated with the cold front. The JT1 and JT2 cross-sections pass through the region of maximum ascent along the warm front.

As before, cross-section JT2 depicts the southern jet at approximately 150 mb for both the C- and D-grid forecasts, with a slightly greater windspeed maximum in the C-grid (Figs. 6.28a,b). The northern jet occurs at 300 mb in the D-grid forecast, approximately at tropopause level. As previously noted, the jet streak is not as elongated or extended as far west in the C-grid forecast (Figs 6.23a,b), therefore, it is

not as apparent in this cross-section. To the northwest of low center there is a strong low-level temperature gradient associated with the warm-front in both the C- and D-grid forecasts. A nearly adiabatic boundary-layer exists over the ocean northwest of the low center depicted by the vertical isentropes in both forecasts. Low-level easterly flow northwest of low center is present in both forecasts, but is stronger in the D-grid forecast reflecting the more intense low-level circulation.

The adjacent thermally direct and thermally indirect circulations in this plane continue to increase in magnitude in both the C- and D-grid forecasts, and are greater in the D-grid (Figs. 6.29a,b). In addition, the maximum ascent continues to increase in both forecasts. The C-grid ascent maximum occurs at approximately 550 mb, while the stronger D-grid maximum has dropped to 650 mb, implying a greater low-level spin-up (Figs. 6.30a,b).

The strong southerly flow just east of the surface low center in the JT1 cross-section has moved up to approximately 300 mb in the C- and D-grid at the 36 h forecast (Figs. 6.31a,b). The cold dome continues to be present in the northerly flow behind the low center in both forecasts. A more pronounced low-level southerly flow is evident east of the low center in the D-grid forecast than in the C-grid. This is producing a larger windspeed gradient and providing

greater horizontal shear, reflecting increased vorticity in the D-grid.

Figure 6.32a,b depicts the longitudinal circulation patterns, which have continued to strengthen in association with the increases in subgeostrophic flow in the trough and the supergeostrophic flow in the ridge. The circulation centers are in closer proximity to each other and at a lower level in the D-grid forecast. In response, the area of ascent east of the surface low center has strengthened in both forecasts with a slightly greater ascent maximum in the D-grid (Figs. 6.33a,b). The ascent maxima in the C- and D-grid forecasts are strong in both the JT1 and JT2 plane, but slightly stronger in the JT2 plane, indicating an increasing influence by the jet streaks. The ascent maximum in the D-grid forecast is also slightly stronger and lower in the atmosphere for both planes, thereby producing greater spin-up of the low-level cyclone, as implied by the vertical gradient of ω.

D. 42 h FORECAST

The C- and D-grid forecasts have continued to deepen the cyclone to central pressures of 969 mb and 960 mb, respectively. The northern 300 mb jet streak has propagated eastward and become more elongated in both forecasts by this time (Figs. 6.34a,b). The D-grid northern jet streak parallels the upper-level contours near the entrance region

north of the surface low, then becomes more cross-contour further downstream. However, the C-grid northern jet streak remains entirely cross-contour and does not extend as far west. The jet streak in both forecasts remains parallel to the upper-level trough south of the surface low. The D-grid forecast has a stronger windspeed gradient on the cyclonic shear side of the jet streaks to the northwest and to the southeast of the surface low center compared to the C-grid. The two jet streaks continue to be positioned favorably to induce laterally interacting transverse ageostrophic circulations. In addition, the upper-level trough/ridge system has increased in amplitude slightly more in the D-grid forecast than in the C-grid.

As in 36 h forecast, strong subgeostrophic flow is evident in the trough with moderate supergeostrophic flow in the ridge for both forecasts (Figs. 6.35a,b). Both also continue to indicate cross-contour ageostrophic flow toward higher geopotential heights near the southern jet's exit region and toward lower geopotential heights near the northern jet's entrance region. The ageostrophic wind in the vicinity of the southern jet is again largely rotational (Figs. 6.37a,b) with a small divergent component in the C- and D-grid (Figs. 6.36a,b). However, the ageostrophic wind component in the vicinity of the northern jet is again predominantly divergent, and slightly greater in the D-grid forecast. Also as before,

the harmonic ageostrophic component (not shown) is relatively weak in these regions.

An area of maximum low-level ascent continues to be located east of the surface low center in both forecasts associated with the warm front. A secondary area of maximum low-level ascent is located south of the surface low center in the C-grid, and south-southwest of the surface low center in the D-grid and is associated with the cold front (Figs. 6.38a,b). As before, the cross-sections intersect at the warm-frontal ascent maximum.

The JT2 cross sections for this forecast hour depict the maximum winds in the southern jet at a lower altitude than before, approximately 300 mb, with secondary maxima further southeast at approximately 200 mb in both the C- and D-grid forecasts (Figs. 6.39a,b). Both forecasts place the northern jet at approximately 300 mb, with the D-grid being substantially stronger. There is also an indication in the D-grid forecast of easterly flow at 300 mb above the cyclone center. Both forecasts indicate strong low-level easterly flow northwest of the low center with a stronger magnitude in the D-grid forecast. The low-level temperature gradient in both forecasts continue to strengthen as the bent-back warm front matures northwest of the low center.

Figure 6.40a depicts the thermally indirect circulation in the C-grid forecast as having weakened from the 36 h forecast, in contrast to the direct circulation which has strengthened.

The maximum ascent increased slightly in this region for the C-grid forecast (Fig. 6.41a). The magnitudes of the D-grid thermally direct and indirect circulations remained virtually unchanged; however, the circulation centers moved closer to each other which tightened the horizontal streamfunction gradient between them (Fig. 6.40b). Therefore, the magnitude of the ascent over the surface low center increased dramatically from the 36 h D-grid forecast (Figs. 6.41b). This strong ascent maximum will generate much more low-level spin-up in the D-grid forecast.

The second cross-section (JT1) which is normal to the first cross-section, indicates a much stronger windspeed gradient near the surface low center for the D-grid forecast, reflecting a much stronger low-level circulation (Figs. 6.42a,b). This stronger circulation is associated with the strong low-level northerly winds at approximately 900 mb, just southwest of the cyclone center in the D-grid forecast. This feature is not as prominent in the C-grid and is displaced further southwest than in the D-grid. The cold dome of air continues to persist west of the low center in both forecasts, with a stronger bent-back warm front in the D-grid forecast just west of the low center.

Figures 6.43a,b depict a stronger gradient between the adjacent circulations in the D-grid, due to the greater magnitudes and closer proximity of the circulations. The magnitude of the C-grid longitudinal circulations have

remained virtually unchanged in this plane, however, the circulation centers have dropped to approximately 550 mb. The ascent region northeast of the surface cyclone in the D-grid is stronger than the C-grid and at a lower level (Figs. 6.44a,b). A prominent descent maximum exists southwest of the surface cyclone in the D-grid, likely a reflection of the stronger frontal circulation associated with the bent-back warm front. The ascent maxima are considerably stronger in the JT2 plane than those in the JT1 plane, which indicate that the influence from the jet streak dynamics are dominant at this time.

E. 48 h FORECAST

The IOP-4 cyclone attained its maximum intensity at this forecast time. The deepening rates over the past 6 h for both forecasts were almost equal. The C-grid forecast deepened the storm to a central pressure of 959 mb, while the D-grid forecast deepened the system to a central pressure of 949 mb. Figures 6.45a,b depict the C- and D-grid 300 mb height and windspeed forecast fields. The southern jet streak continues to propagated easterly and is located in the base of the upper-level trough, with the maximum windspeed gradient oriented south of the surface low center for both forecasts. The C-grid has a broad area of maximum winds to the south of the low center, whereas, the D-grid has a smaller, more concentrated area of maximum winds south-southeast of the

surface low center, and a much broader area of maximum wind speeds south of the surface low center at 200 mb (not shown). The northern jet streak continues to be oriented perpendicular to the upper-level ridge in both forecasts and has weakened in magnitude. The C-grid forecast maximum windspeed area is smaller than the D-grid and is oriented east-northeast of the surface low center, whereas, the jet streak in the D-grid forecast is more elongated and has greater curvature. The NGM 00Z/05 analysis (Fig. 6.45c) depicts the northern jet streak with a stronger windspeed maximum than the C- or D-grid forecasts, however the structure continues to more closely resemble the C-grid forecast. The southern jet's exit region appears to be better defined in the analysis than in the forecasts.

The surface low center is in the divergent quadrant for both the northern and southern jet streaks. The upper-level trough south of the surface low center is characterized by strong subgeostrophic flow, with a slight cross-stream ageostrophic component near the southern jet-exit region in both the C- and D-grid forecasts (Figs. 6.46a,b). As before, the upper-level ridge north of the low center is characterized by supergeostrophic flow, with the ageostrophic wind directed toward lower geopotential heights near the northern jet-entrance region. Figures 6.48a,b indicate that the ageostrophic wind component south of the surface low center is primarily rotational and associated with the upper-level

trough. However, the ageostrophic wind north of the surface low center is predominantly divergent and associated with the northern jet's entrance region (Figs. 6.47a,b). The harmonic ageostrophic component (not shown) continues to be relatively small in these regions.

The low-level ascent maximum is located northeast of the surface cyclone center in both the C- and D-grid forecast (Figs. 6.49a,b). The maximum ascent region extends eastward in both forecasts indicative of the vertical motion associated with the warm front. Secondary maxima associated with the cold front and bent-back warm front are also evident.

The JT2 cross-section continues to depicts the northern jet at approximately 300 mb for both forecasts, with a slightly greater maximum in the D-grid forecast (Figs. 6.50a,b). However, the C-grid jet increased slightly in magnitude, while the D-grid jet magnitude was virtually unchanged from the previous time. The southern jet occurs at approximately 350 mb in both forecasts. The secondary southeastern 200 mb jet continues to be evident in the D-grid forecast, however in no longer present in the C-grid. The D-grid also shows a small easterly flow component at 300 mb just northwest of the low center that is not present in the C-grid. A strong low-level circulation about the low center and a strong horizontal windspeed gradient are evident in both forecasts.

Figures 6.51 a,b depict the thermally direct and indirect circulation in this plane to have decreased slightly in magnitude in both forecasts. Both circulations continue to be stronger in the D-grid forecast than in the C-grid. In response to the decrease in the transverse circulations, the ascent just north of the surface low center has decreased in magnitude in both forecasts. However, the D-grid ascent remains stronger and at a lower altitude than the C-grid implying stronger spin-up (Figs. 6.52a,b).

The JT1 cross-section reveals a much stronger windspeed gradient southwest of the surface low center in the D-grid forecast compared to the C-grid (Figs. 6.53a,b). The low-level northerly wind that was apparent in the D-grid at 42 h forecast is now also present in the C-grid, although not as strong. The longitudinal circulations have increased in strength in the C-grid (Fig. 6.54a), however the ascent maximum has remained relatively constant (Fig. 6.55a). The magnitude of the longitudinal circulations are virtually unchanged for the D-grid, however, the centers have moved farther apart, thereby weakening the gradient between them (Fig. 6.54b). In response, the ascent maximum has decreased in magnitude (Fig. 6.55b). The weakening of the ascent in both forecasts and both cross-section planes implies less low-level spin-up of the surface cyclone.

Throughout the forecast period, the curvature effects associated with the upper-level trough/ridge system led to

significant longitudinal ageostrophic circulations which acted to develop the surface cyclone through low-level convergence and spin-up as well as upper-level divergence and mass removal aloft. In addition, laterally interacting jet streaks produced transverse ageostrophic circulations which were critical to the deepening of the low-level cyclone. Since the D-grid transverse and longitudinal circulations produced for the most part larger ascent values at lower levels, this yielded greater low-level convergence and spin-up of the low-level cyclone as well as greater upper-level mass divergence compared to the C-grid forecast.

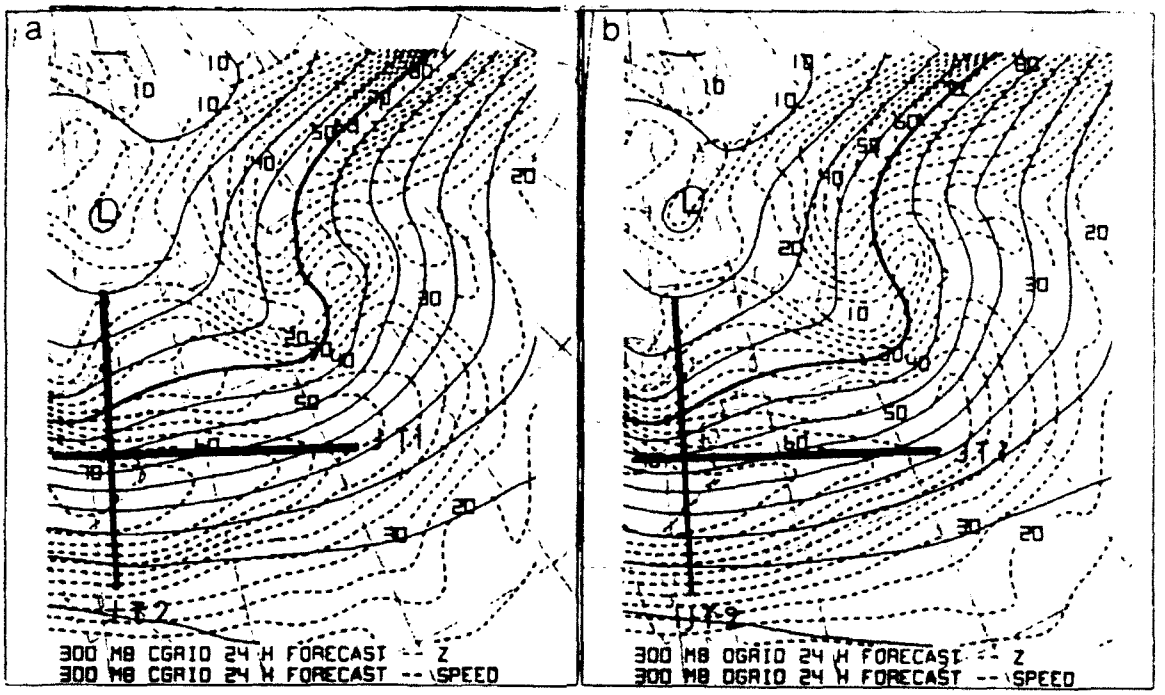

Figure 6.1. NGM 24 h forecast, verification time 00Z/04: (a) C-grid: 300 mb heights, 100 dm increment (880 dm bold contour), and wind speed, 5 m s^{-1} increment; (b) D-grid: as in (a).

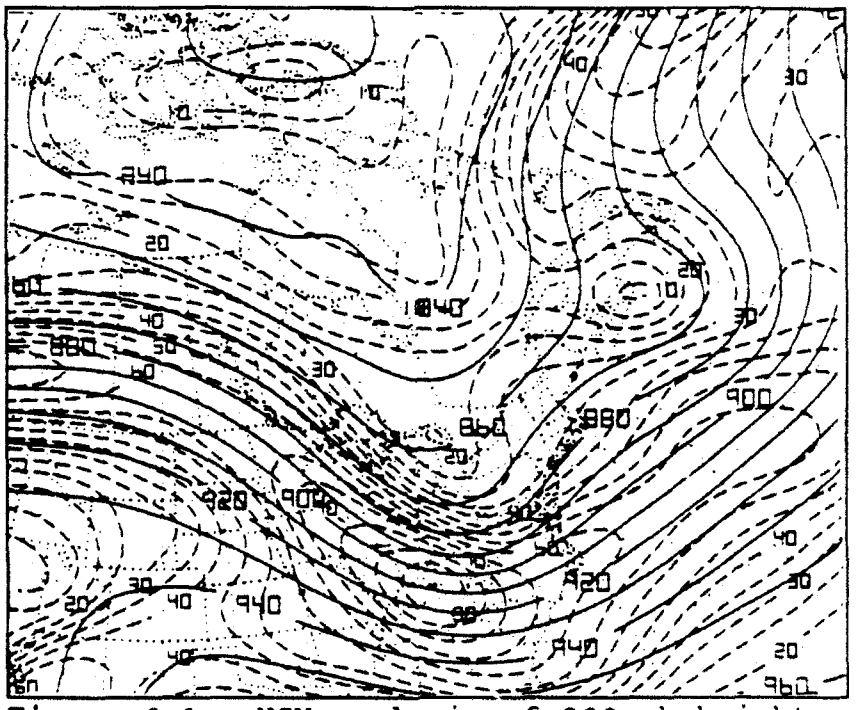

Figure 6.1c. NGM analysis of 300 mb heights, 10 dm increment, and windspeed, 5 m s^{-1} increment; at 00Z/04.

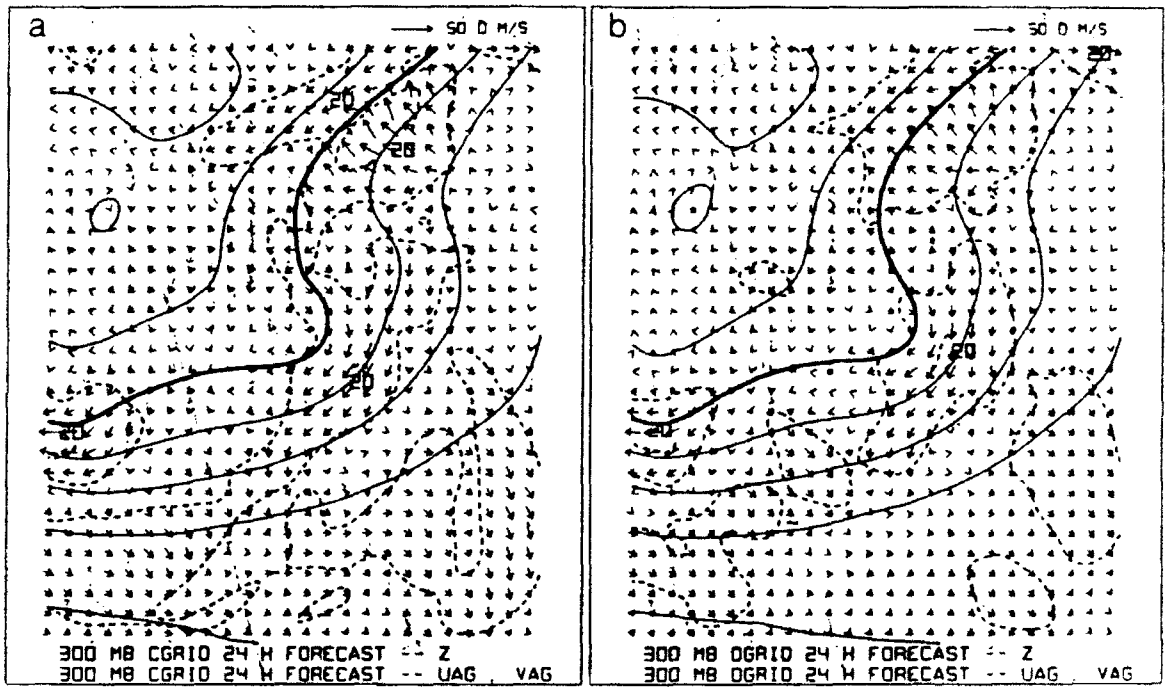

Figure 6.2. NGM 24 h forecast, verification time 00Z/04: (a) C-grid: 300 mb heights, 100 dm increment (880 dm bold contour), and ageostrophic wind speed, 50 m s^{-1} scale; (b) D-grid: as in (a)

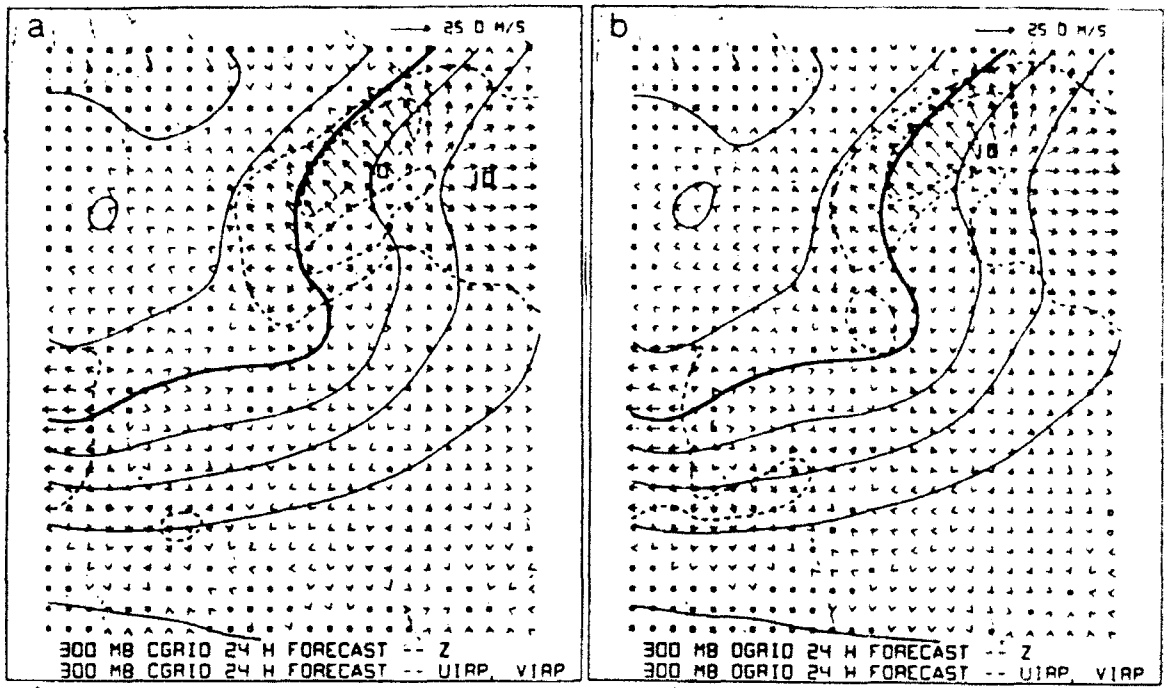

Figure 6.3. NGM 24 h forecast, verification time 00Z/04: (a) C-grid: 300 mb heights, 100 dm increment (880 dm bold contour), and divergent ageostrophic wind component, 25 m s^{-1} scale; (b) D-grid: as in (a).

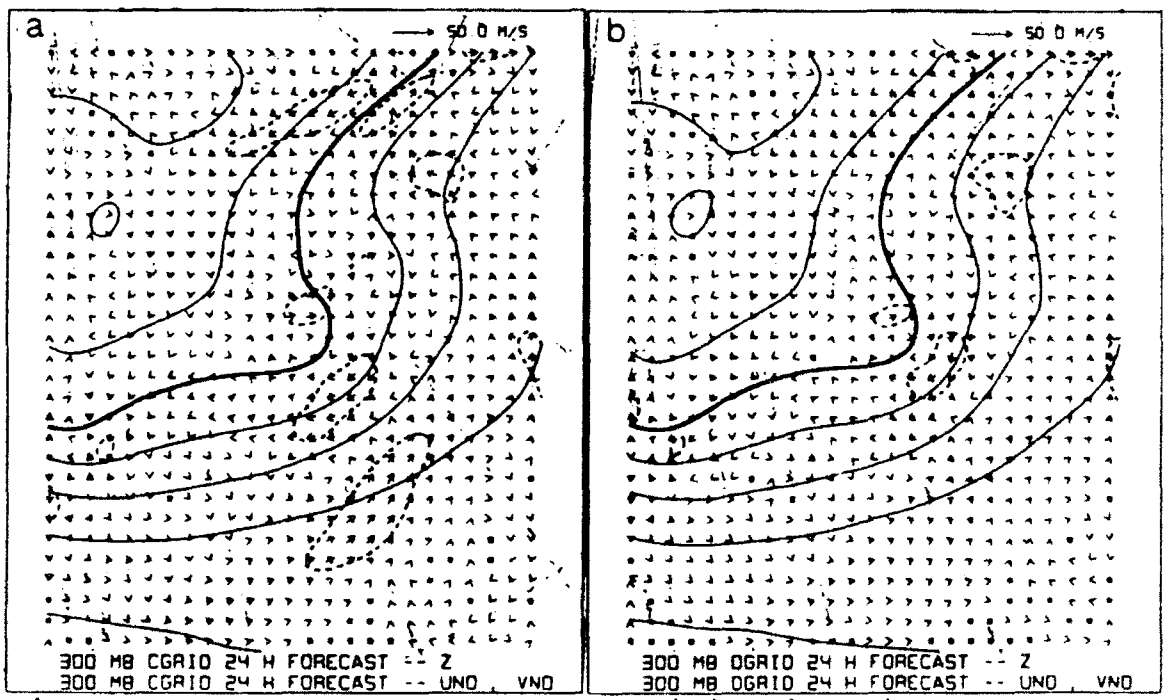

Figure 6.4. NGM 24 h forecast, verification time 00Z/04: (a) C-grid: 300 mb heights, 100 dm increment (880 dm bold contour), and rotational ageostrophic wind component, 50 m s^{-1} scale; (b) D-grid: as in (a).

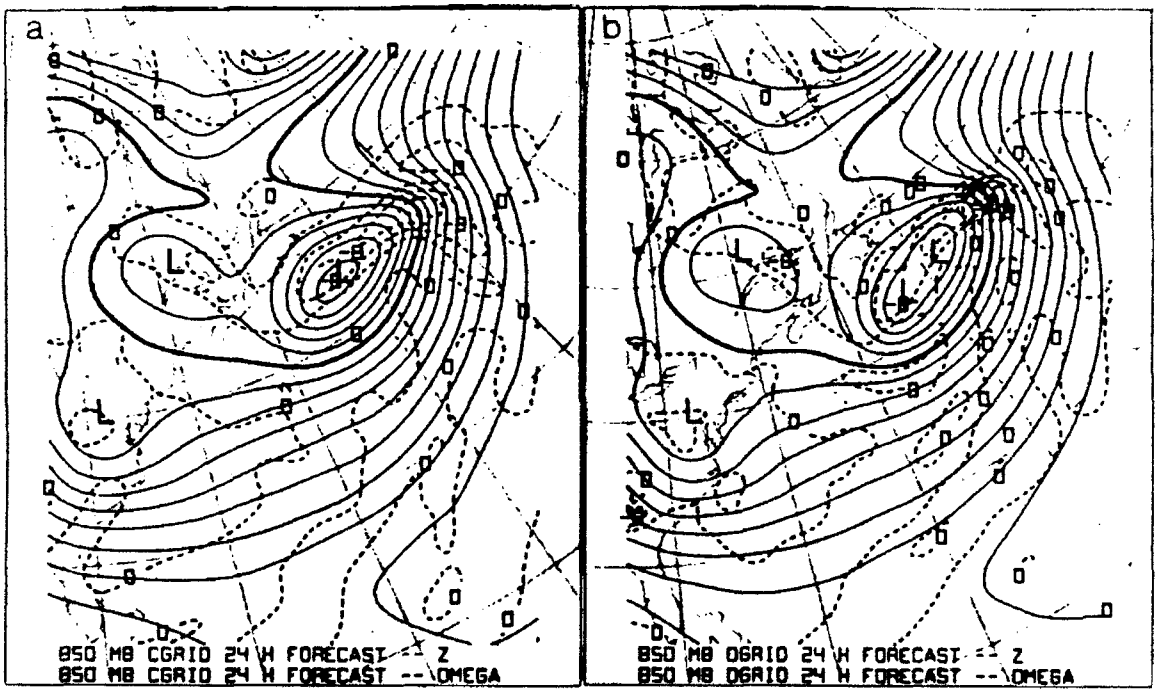

Figure 6.5. NGM 24 h forecast, verification time 00Z/04: (a) C-grid: 300 mb heights, 100 dm increment (880 bold contour), and vertical motion, 4 μb s^{-1} increment; (b) D-grid: as in (a)

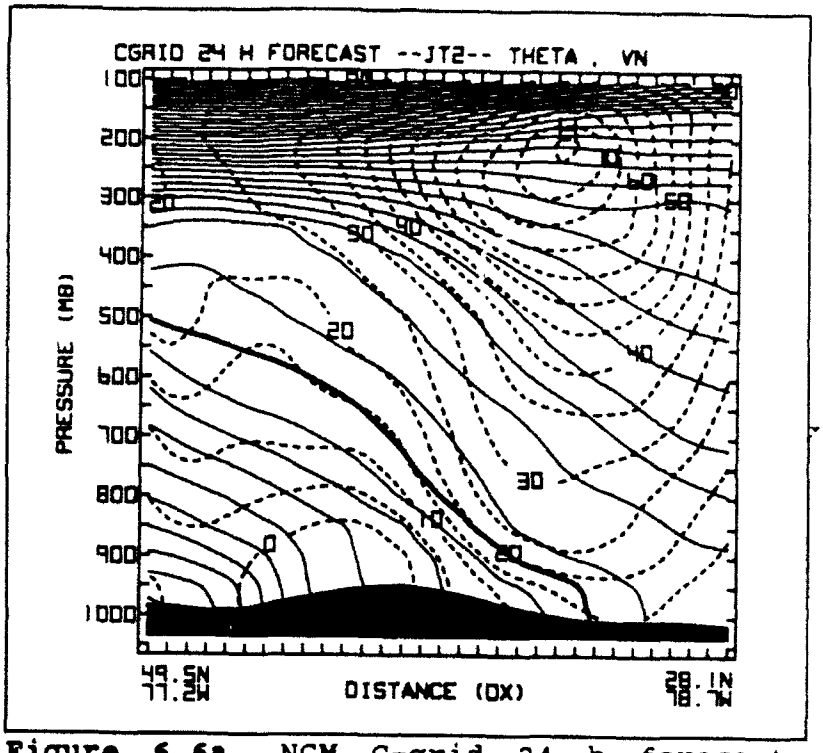

Figure 6.6a. NGM C-grid 24 h forecast, verification time 00Z/04: Potential temperature, 5 K increment (290 K bold contour), and normal component of the total wind, 5 m s^{-1} increment

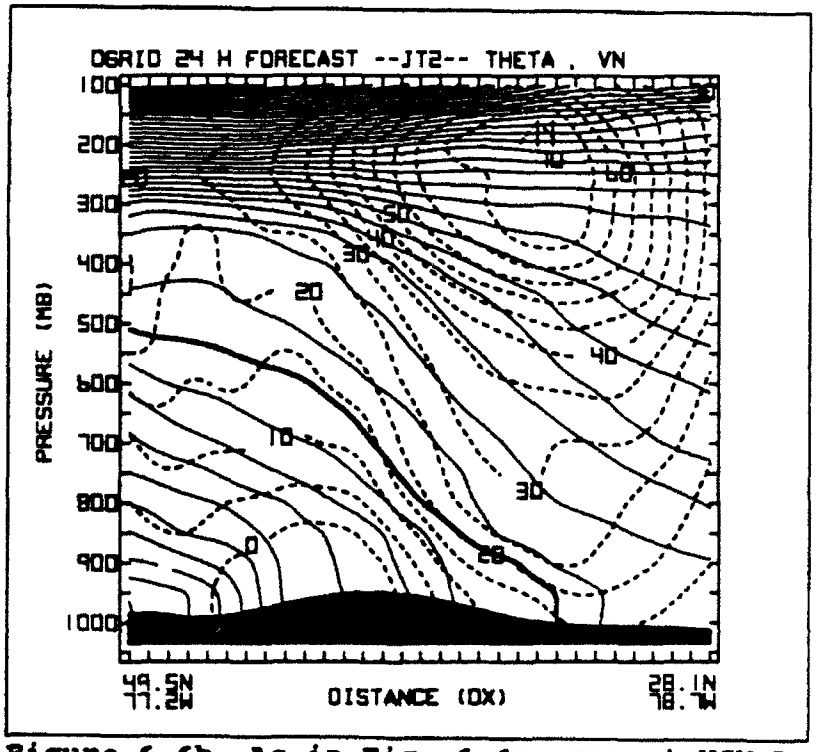

Figure 6.6b. As in Fig. 6.6a, except NGM D-grid 24 h forecast

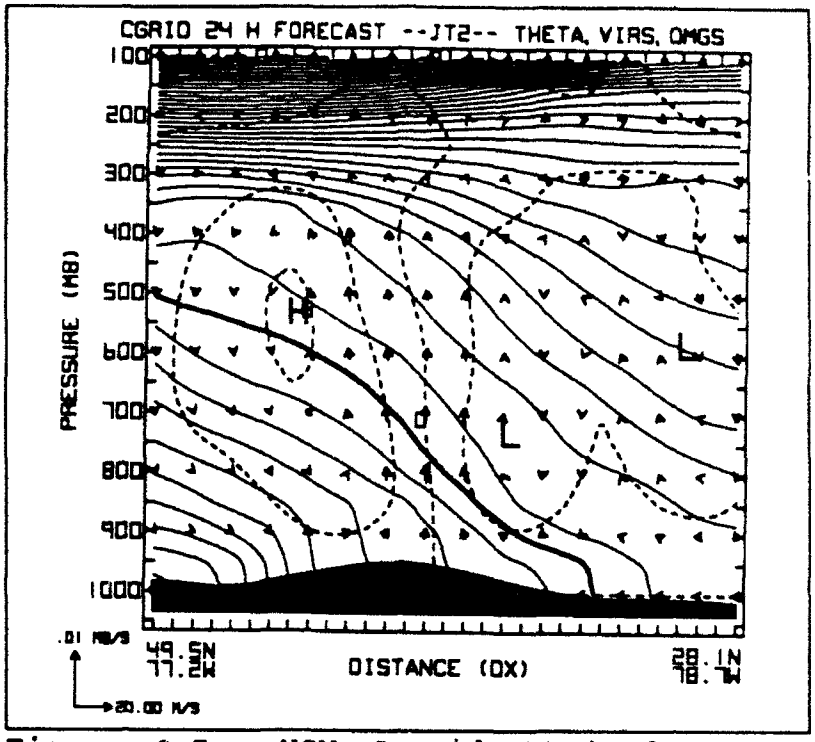

Figure 6.7a. NGM C-grid 24 h forecast, verification time 00Z/04: Potential temperature, and vectors composed of the divergent ageostrophic wind component and vertical velocity within JT2

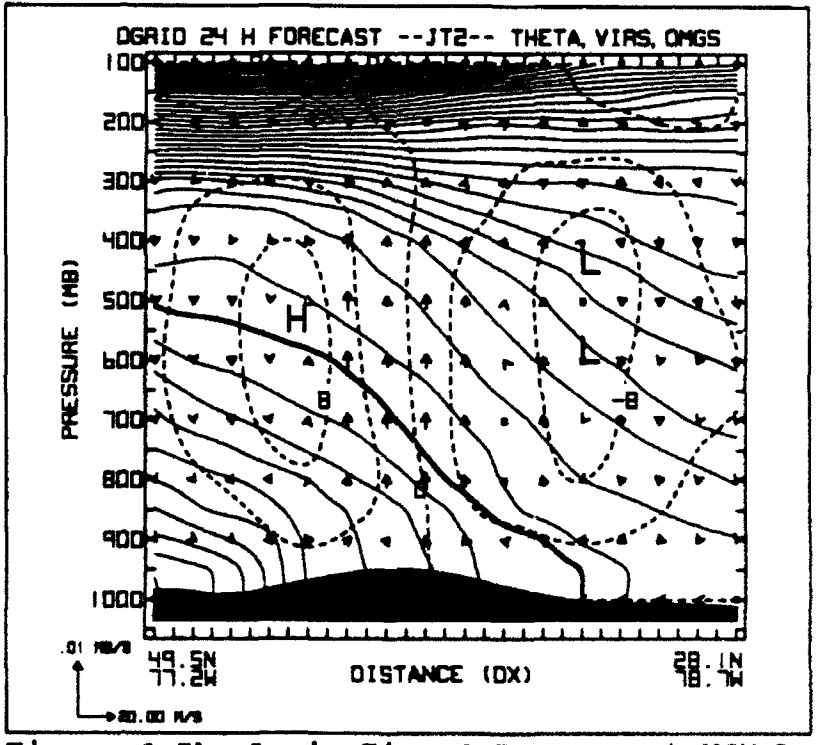

Figure 6.7b. As in Fig. 6.7a, except NGM D-grid 24 h forecast

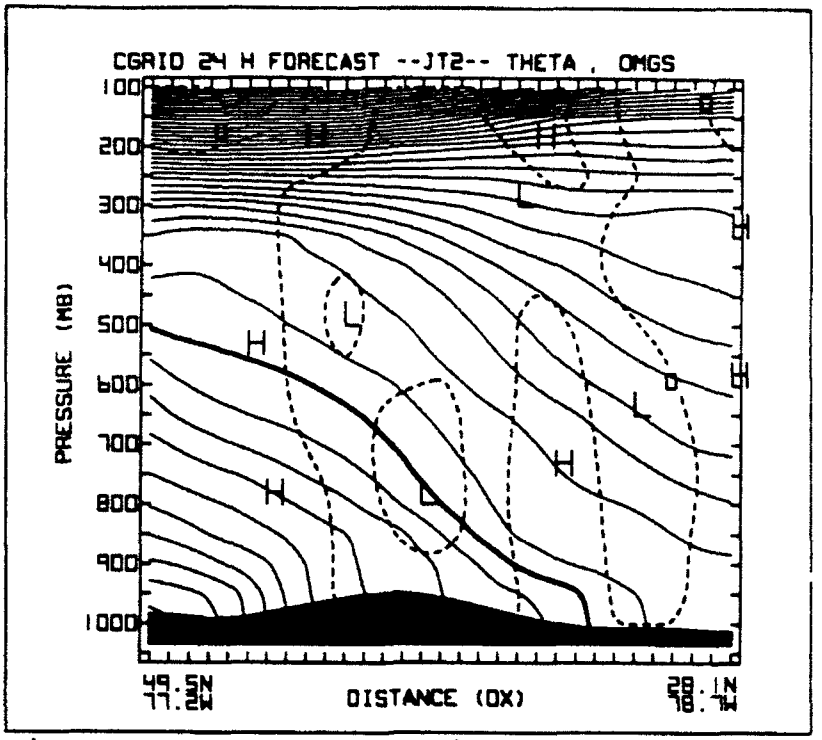

Figure 6.8a. NGM C-grid 24 h forecast, verification time 00Z/04: Potential temperature, and vertical velocity, 2 μb s^{-1} increment within the JT2 cross-section

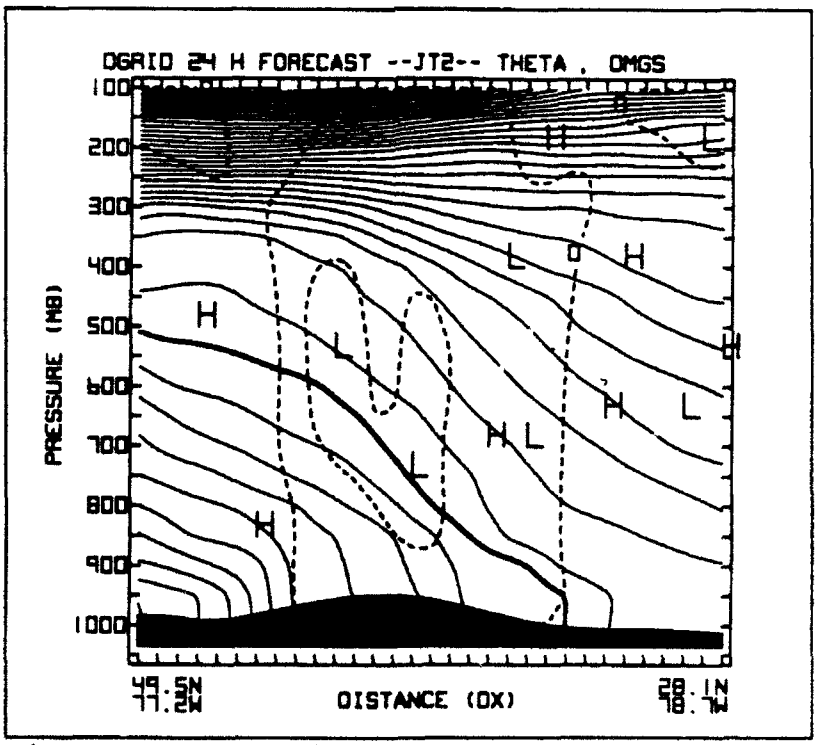

Figure 6.8b. As in Fig. 6.8a, except NGM D-grid 24 h forecast

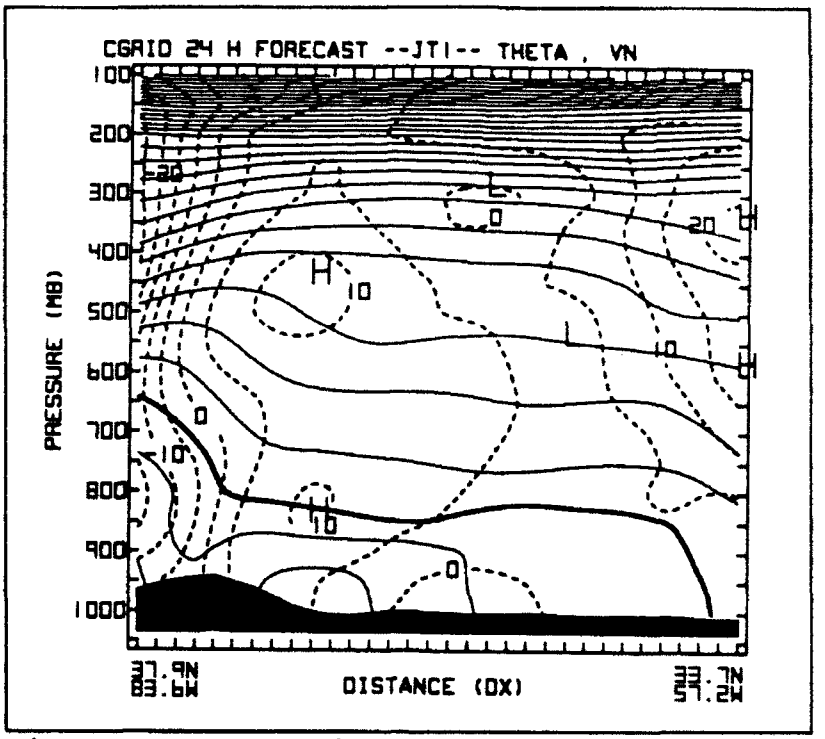

Figure 6.9a. As in Fig. 6.6a, except JT1 cross-section

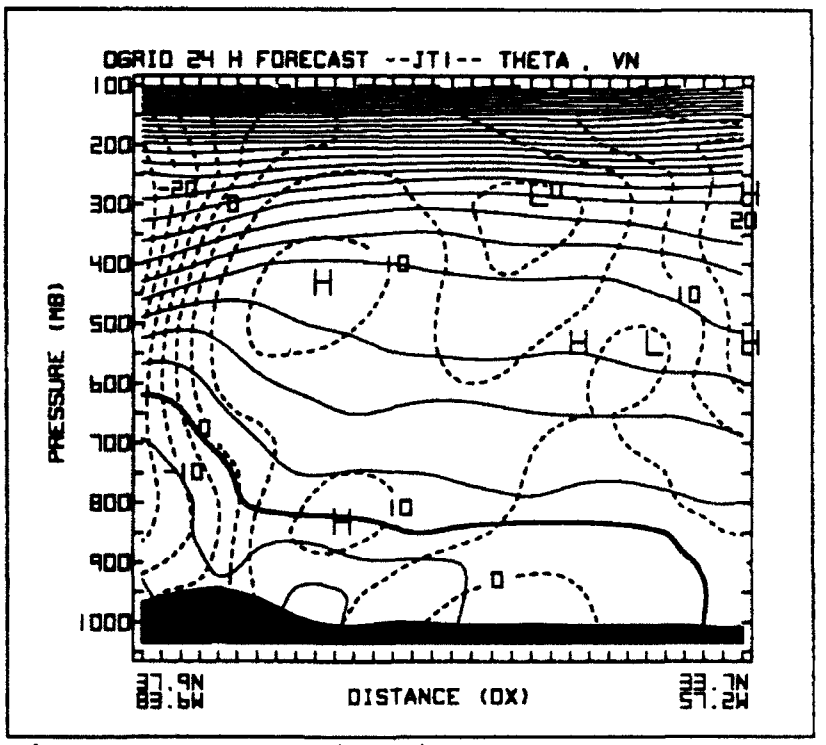

Figure 6.9b. As in Fig. 6.6b, except JT1 cross-section

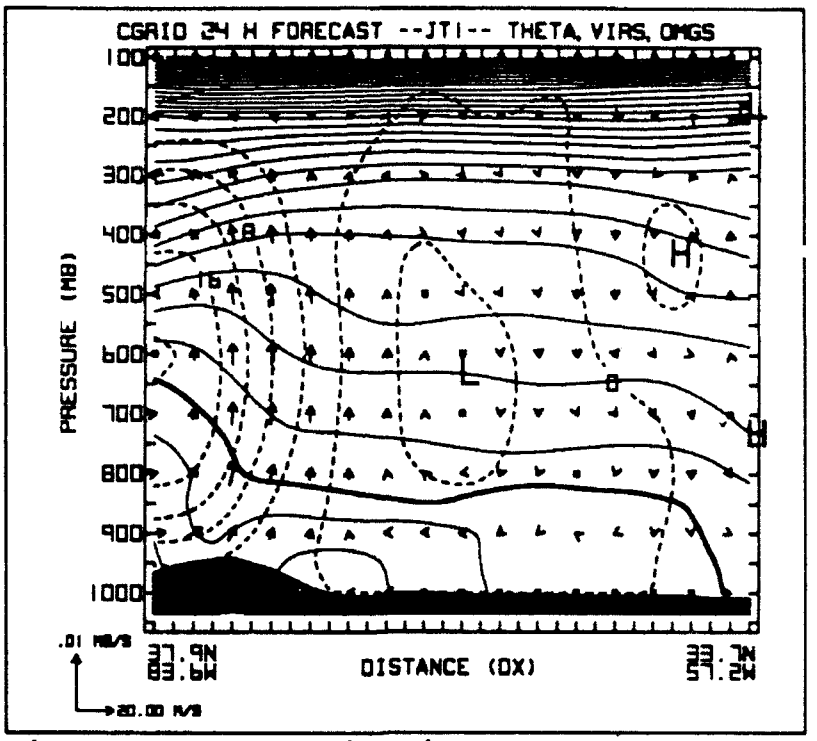

Figure 6.10a. As in Fig. 6.7a, except JT1 cross-section

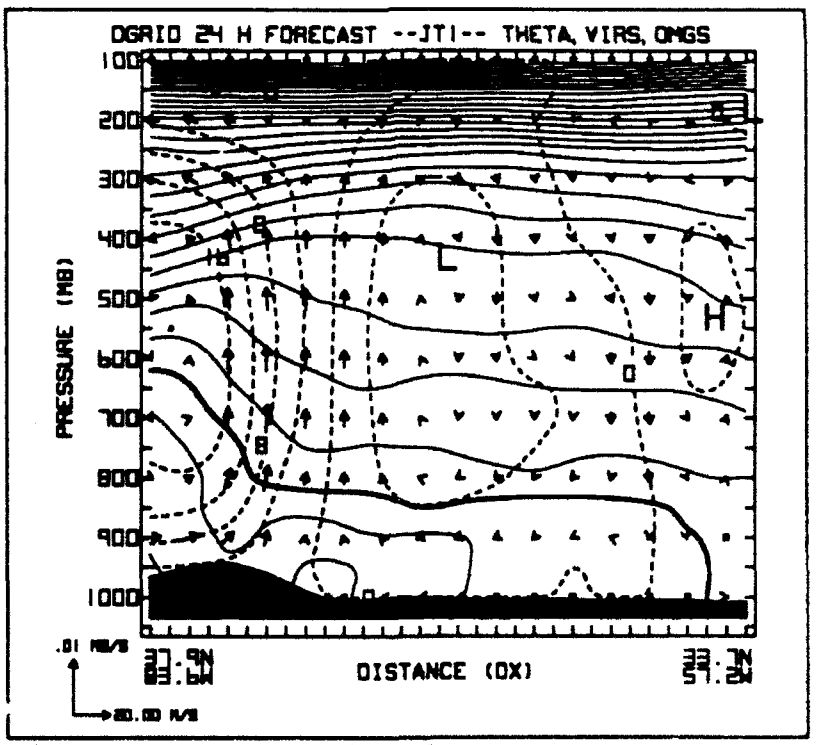

Figure 6.10b. As in Fig. 6.7b, except JT1 cross-section

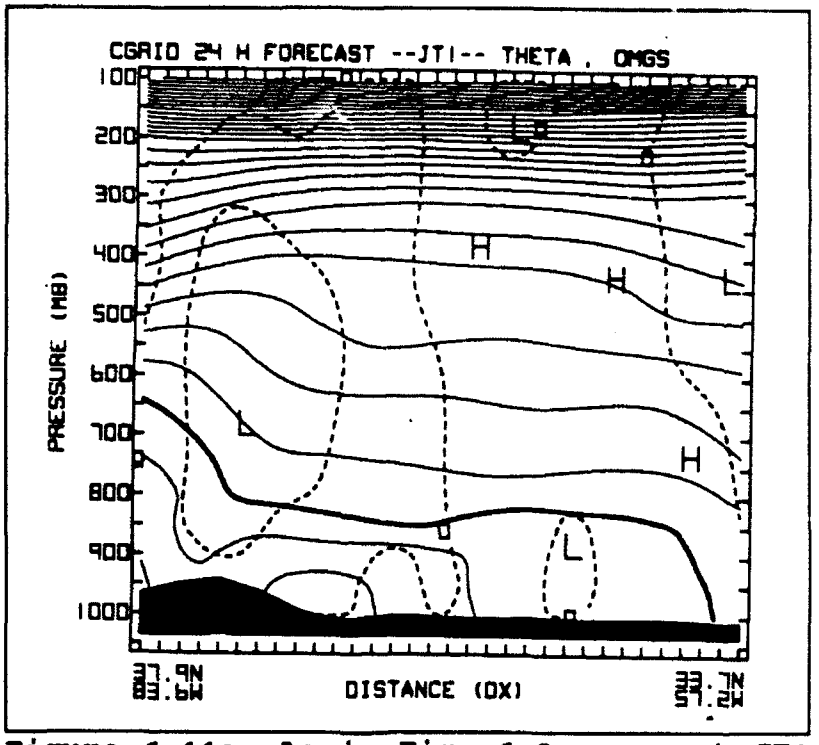

Figure 6.11a. As in Fig. 6.8a, except JT1 cross-section

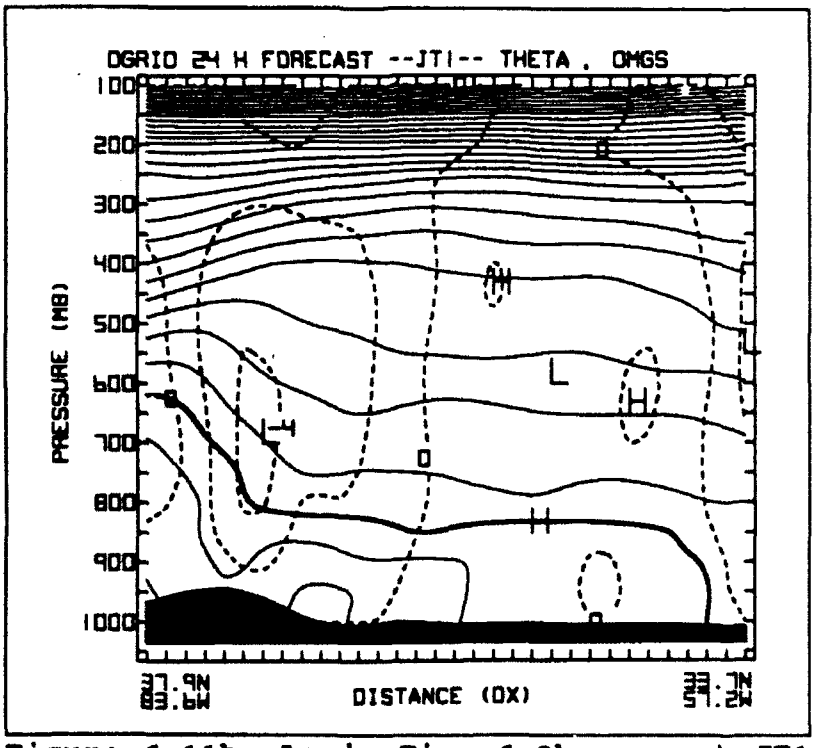

Figure 6.11b. As in Fig. 6.8b, except JT1 cross-section

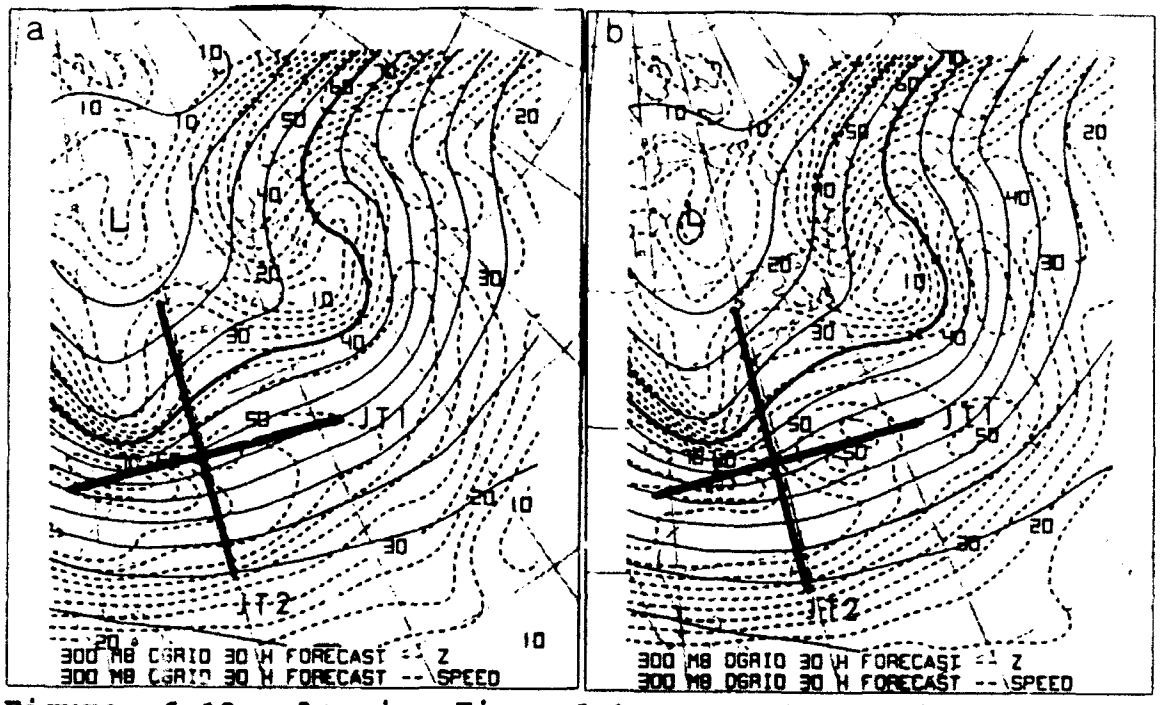

Figure 6.12. As in Fig. 6.1, except 30 h forecast, verification time 06Z/04

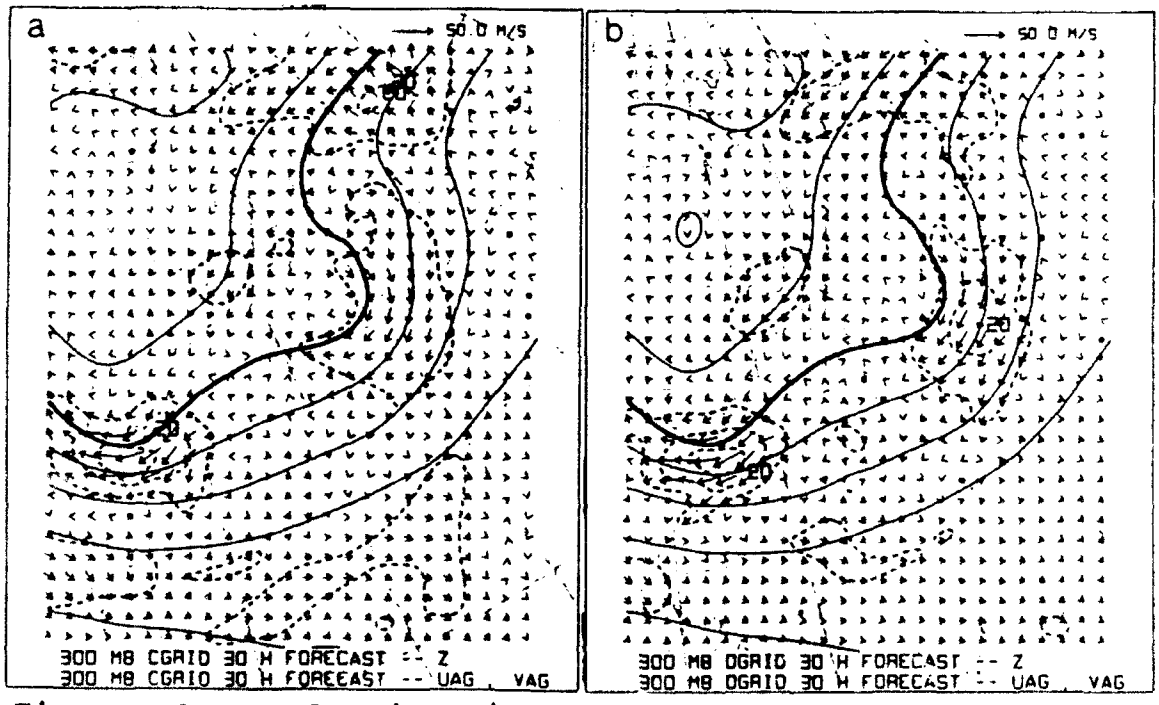

Figure 6.13. As in Fig. 6.2, except 30 h forecast, verification time 06Z/04

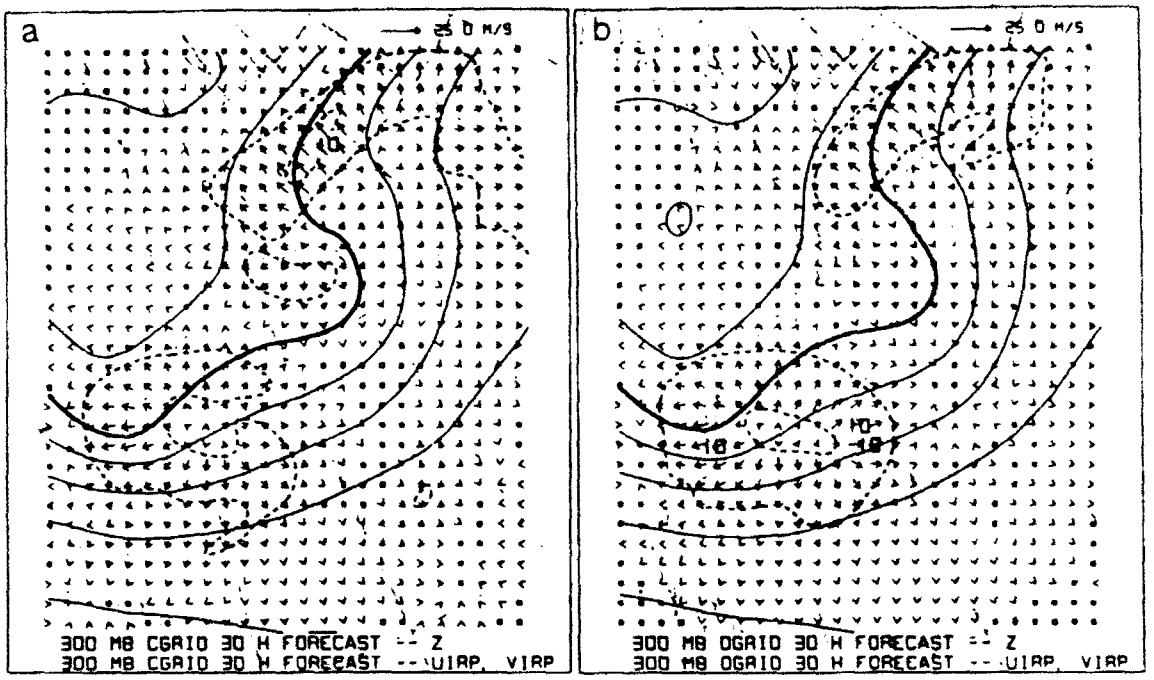

Figure 6.14. As in Fig. 6.3, except 30 h forecast, verification time 06Z/04

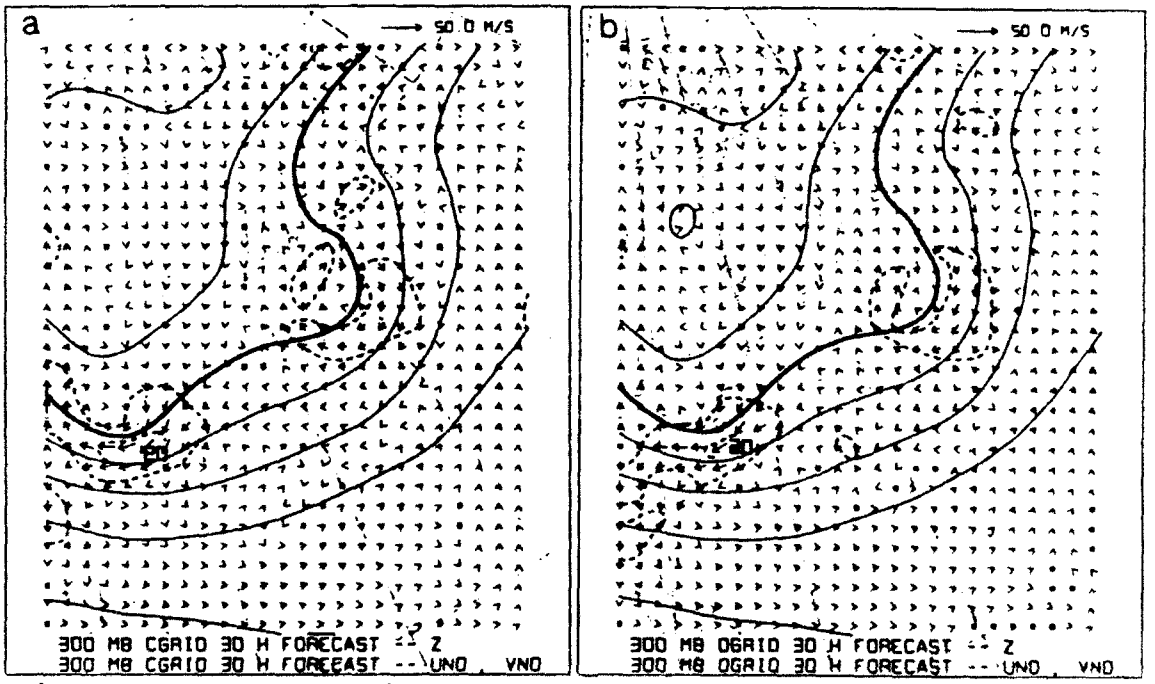

Figure 6.15. As in Fig. 6.4, except 30 h forecast, verification time 06Z/04

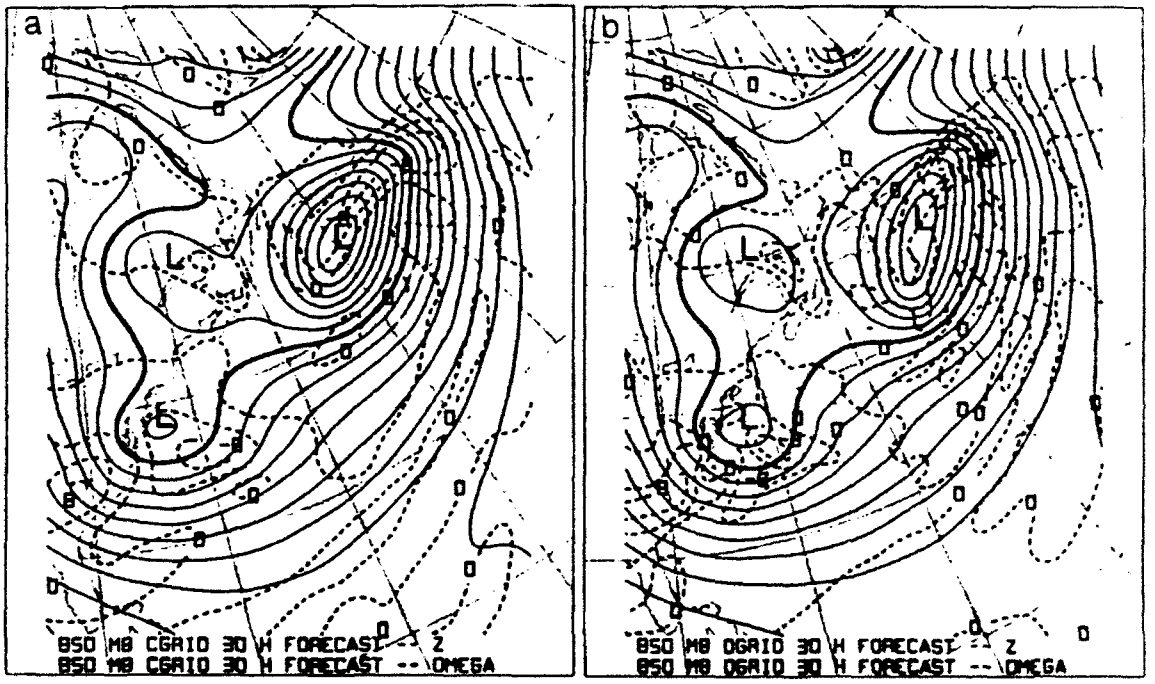

Figure 6.16. As in Fig. 6.5, except 30 h forecast, verification time 06Z/04

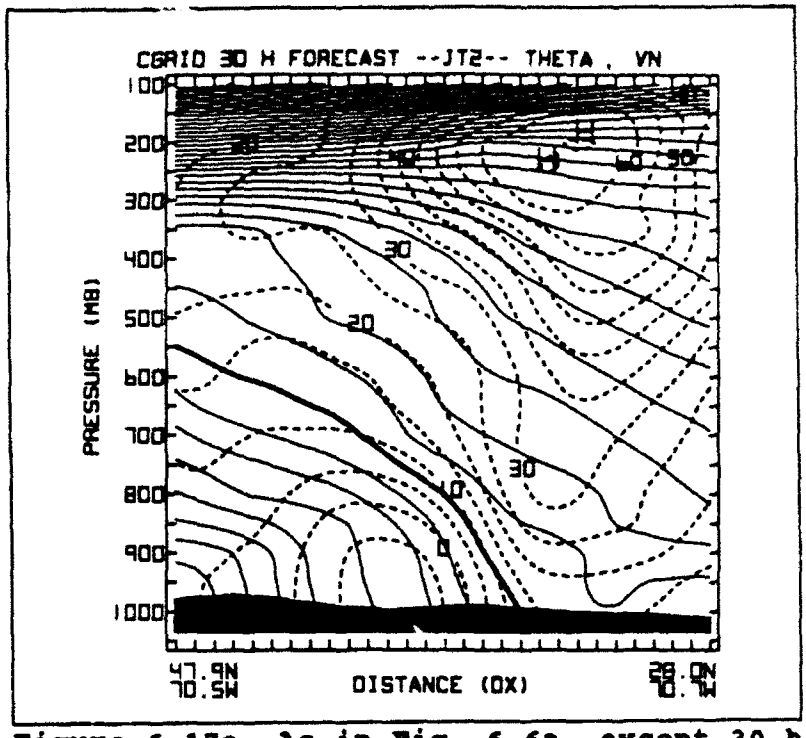

Figure 6.17a. As in Fig. 6.6a, except 30 h forecast, verification time 06Z/04

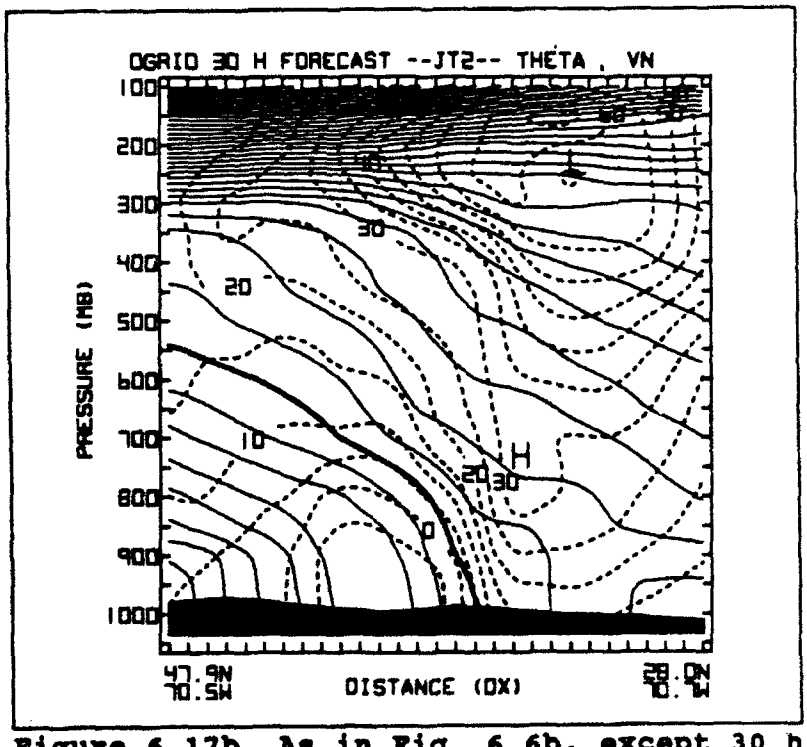

Figure 6.17b. As in Fig. 6.6b, except 30 h forecast, verification time 06Z/04

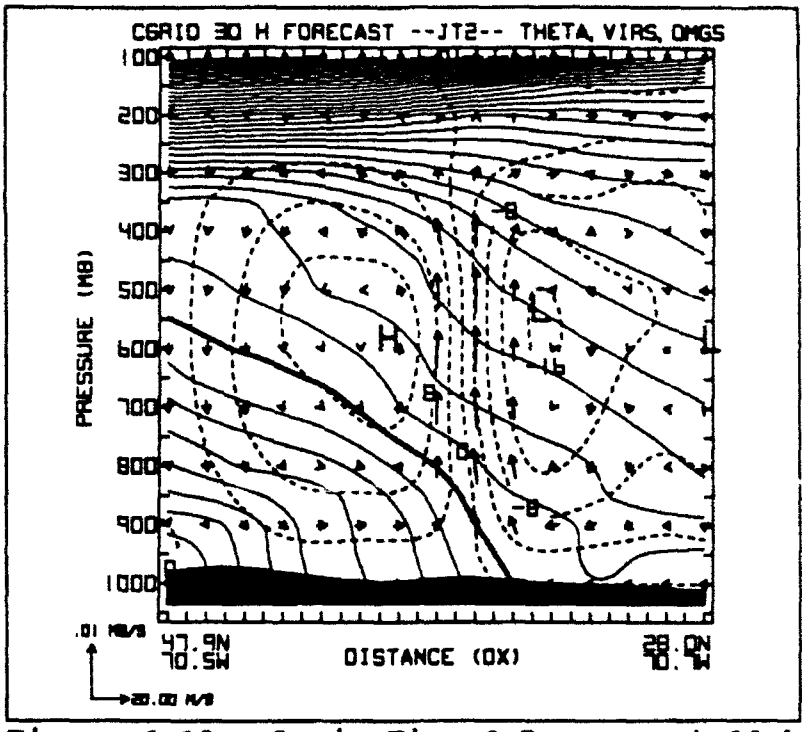

Figure 6.18a. As in Fig. 6.7a, except 30 h forecast, verification time 06Z/04

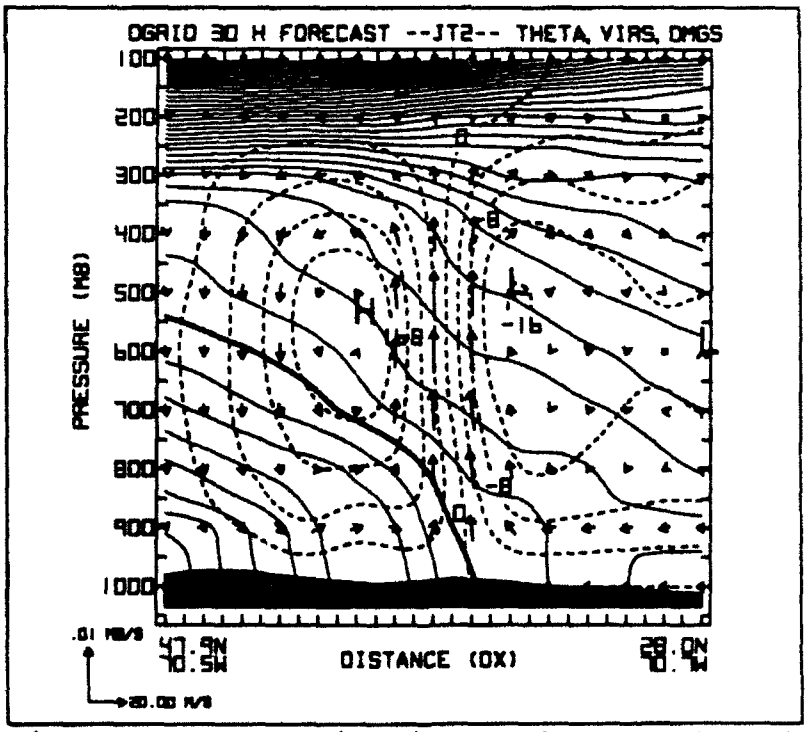

Figure 6.18b. As in Fig. 6.7b, except 30 h forecast, verification time 06Z/04

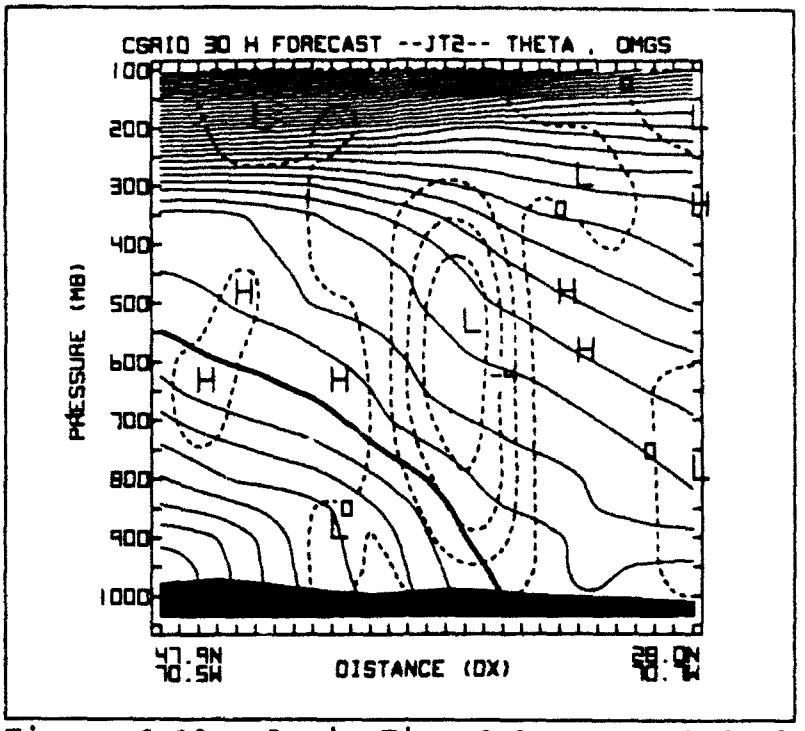

Figure 6.19a. As in Fig. 6.8a, except 30 h forecast, verification time 06Z/04

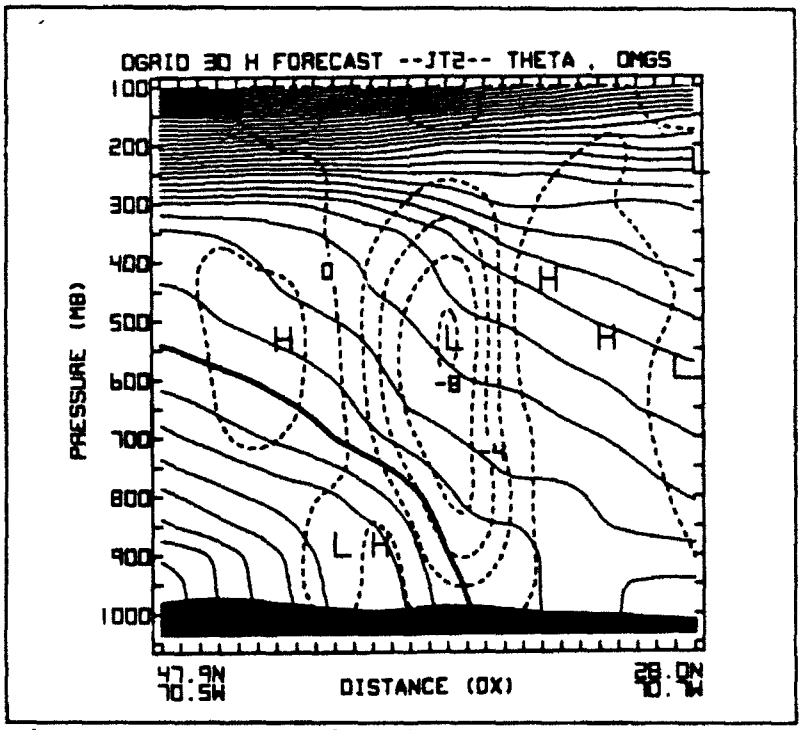

Figure 6.19b. As in Fig. 6.8b, except 30 h forecast, verification time 06Z/04

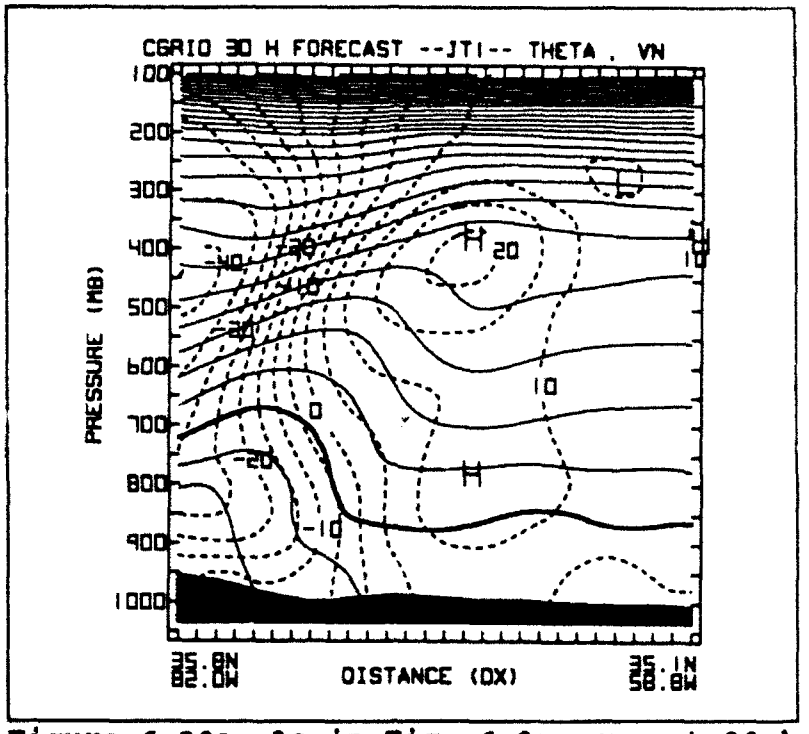

Figure 6.20a. As in Fig. 6.9a, except 30 h forecast, verification time 06Z/04

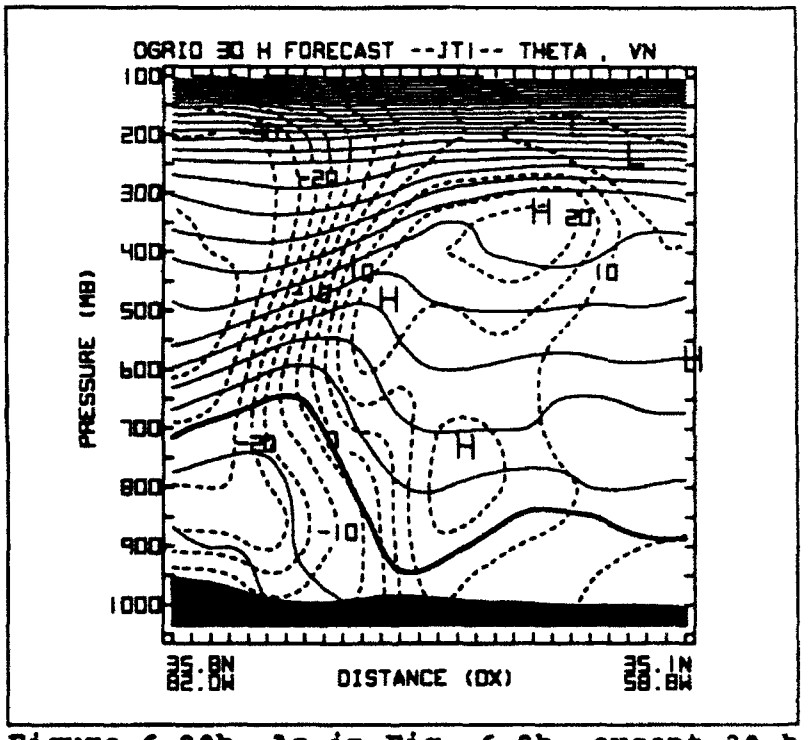

Figure 6.20b. As in Fig. 6.9b, except 30 h forecast, verification time 06Z/04

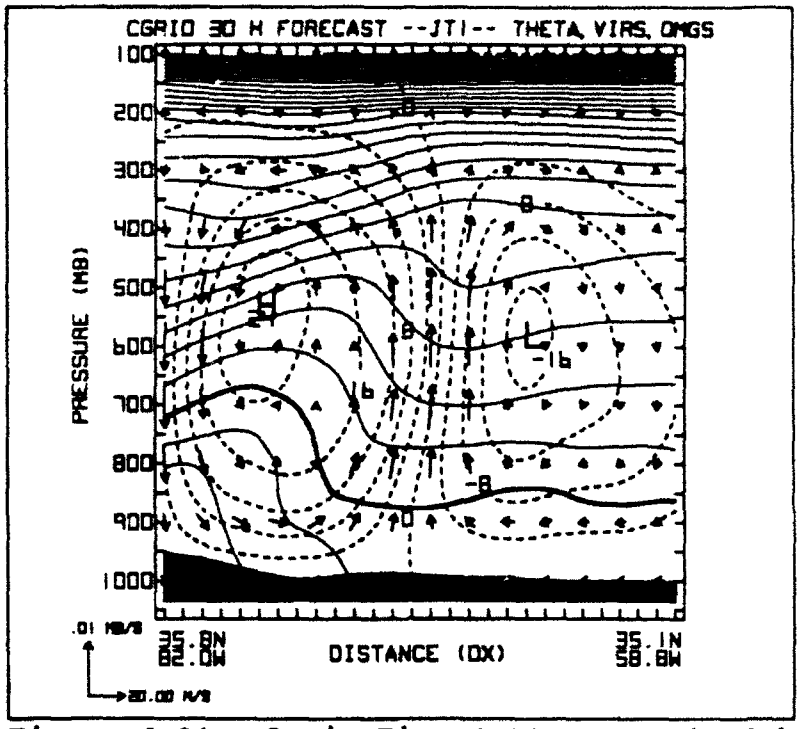

Figure 6.21a. As in Fig. 6.10a, except 30 h forecast, verification time 06Z/04

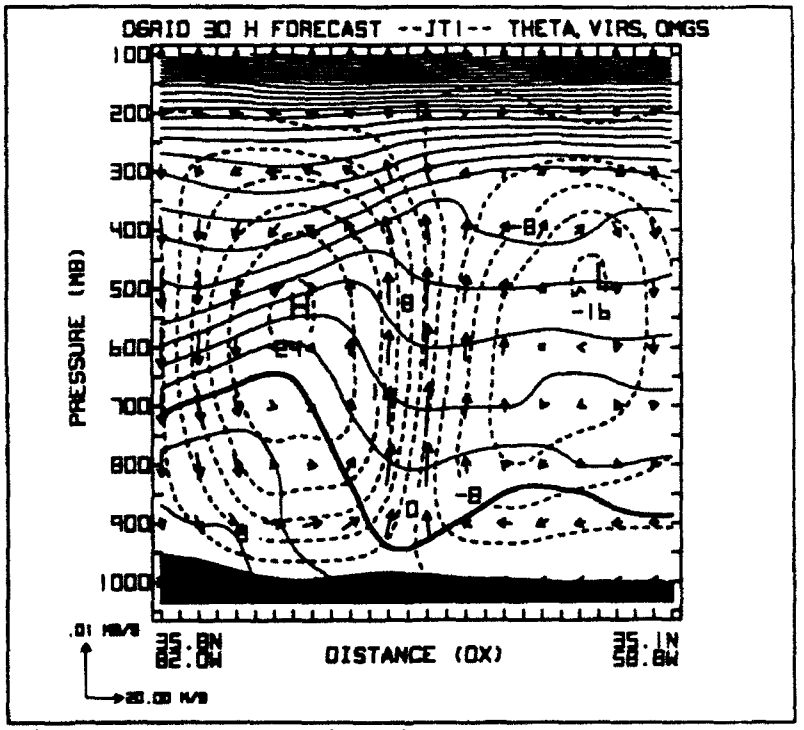

Figure 6.21b. As in Fig. 6.10b, except 30 h forecast, verification time 06Z/04

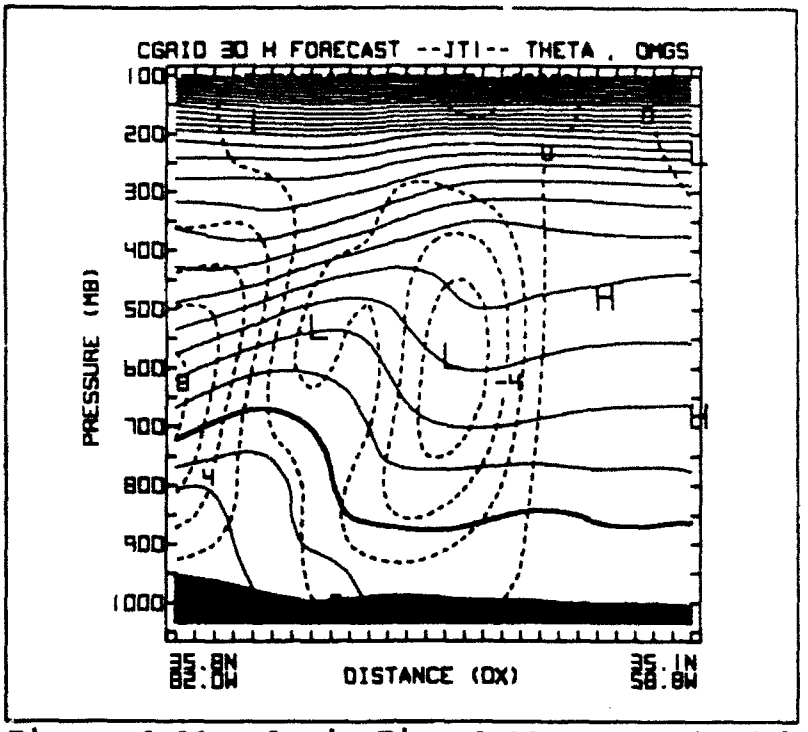

Figure 6.22a. As in Fig. 6.11a, except 30 h forecast, verification time 06Z/04

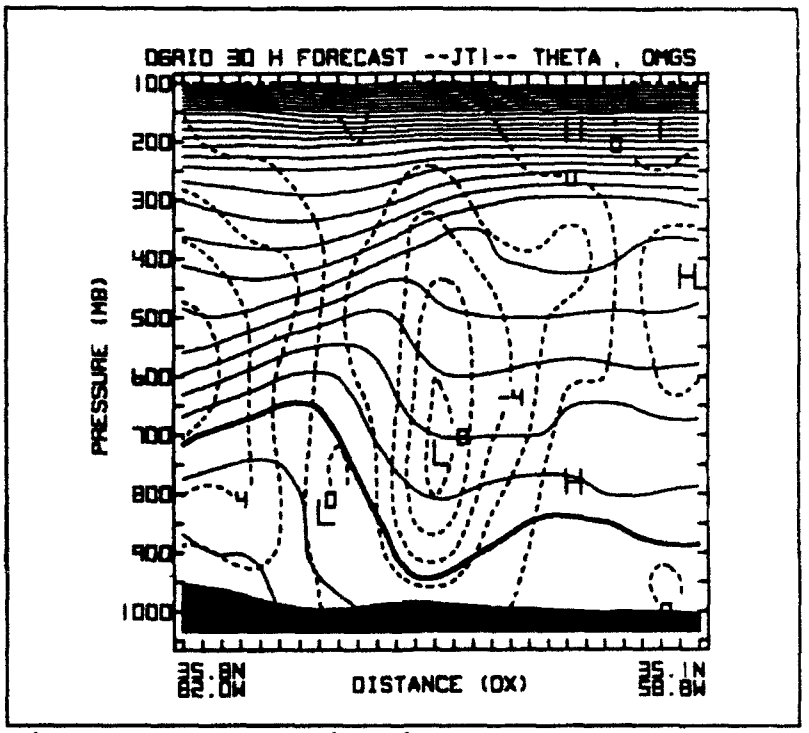

Figure 6.22b. As in Fig. 6.11b, except 30 h forecast, verification time 06Z/04

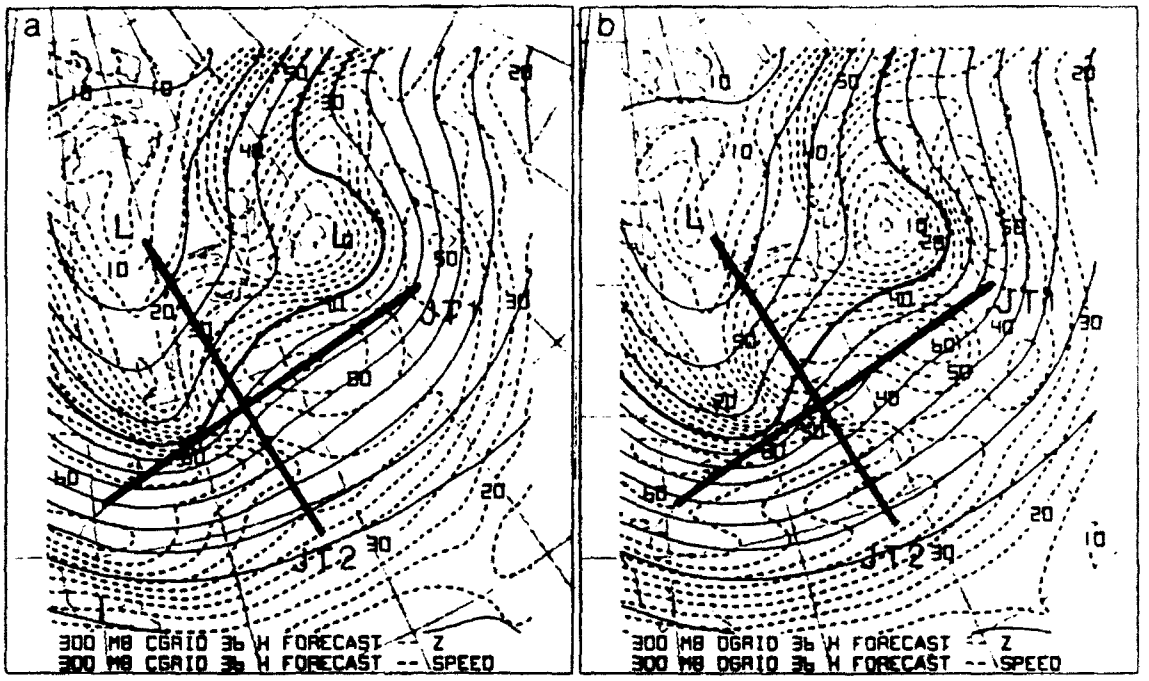

Figure 6.23. As in Fig. 6.1, except 36 h forecast, verification time 12Z/04

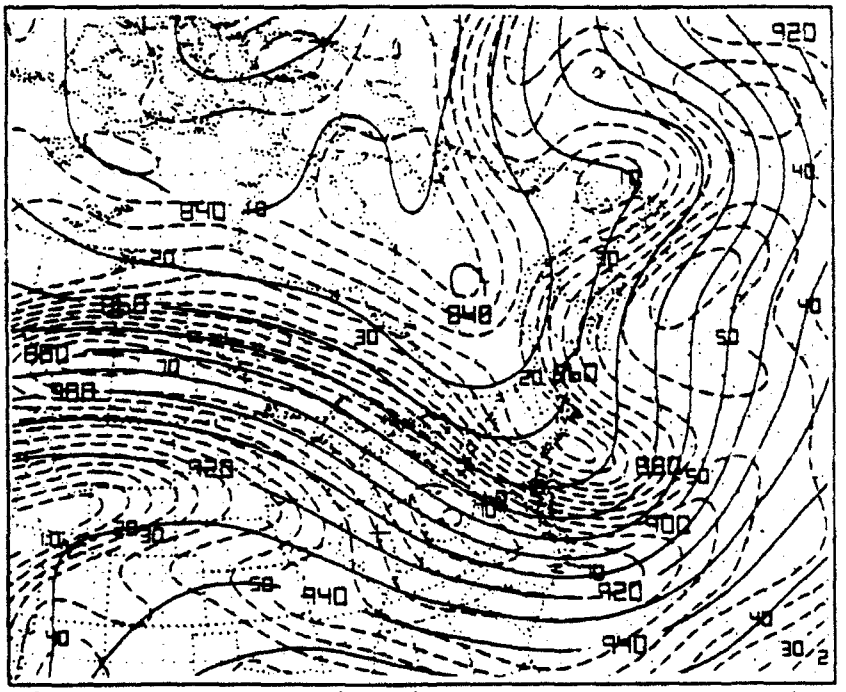

Figure 6.23c. As in Fig. 6.1c, except 12Z/04

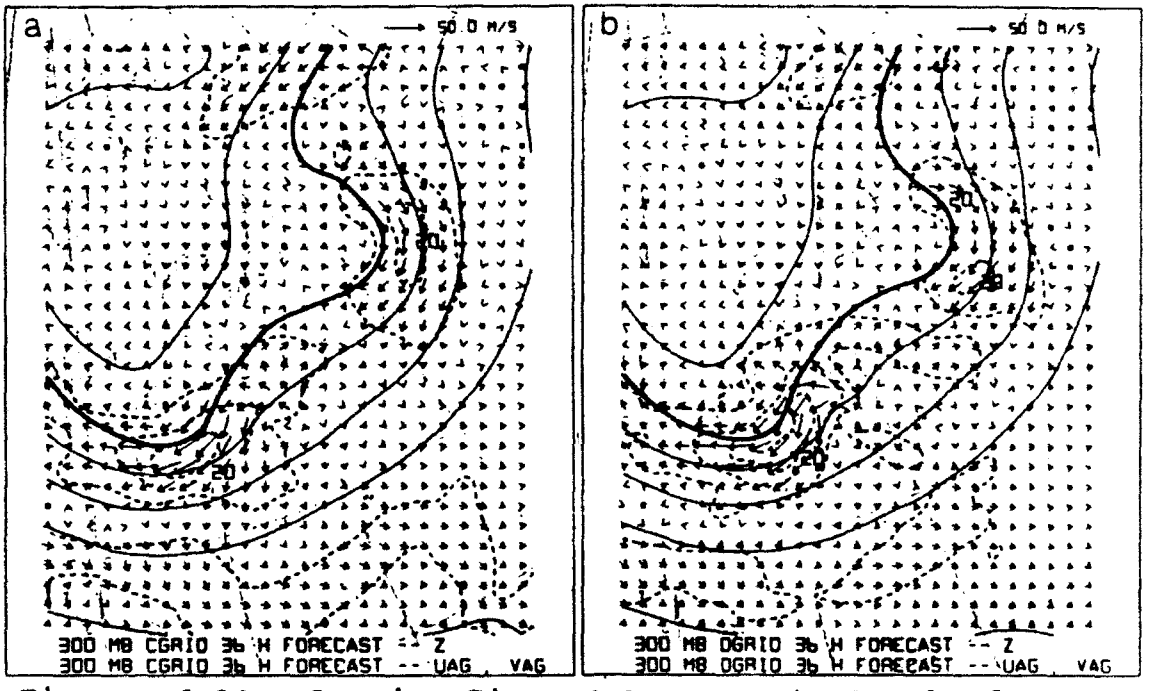

Figure 6.24. As in Fig. 6.2, except 36 h forecast, verification time 12Z/04

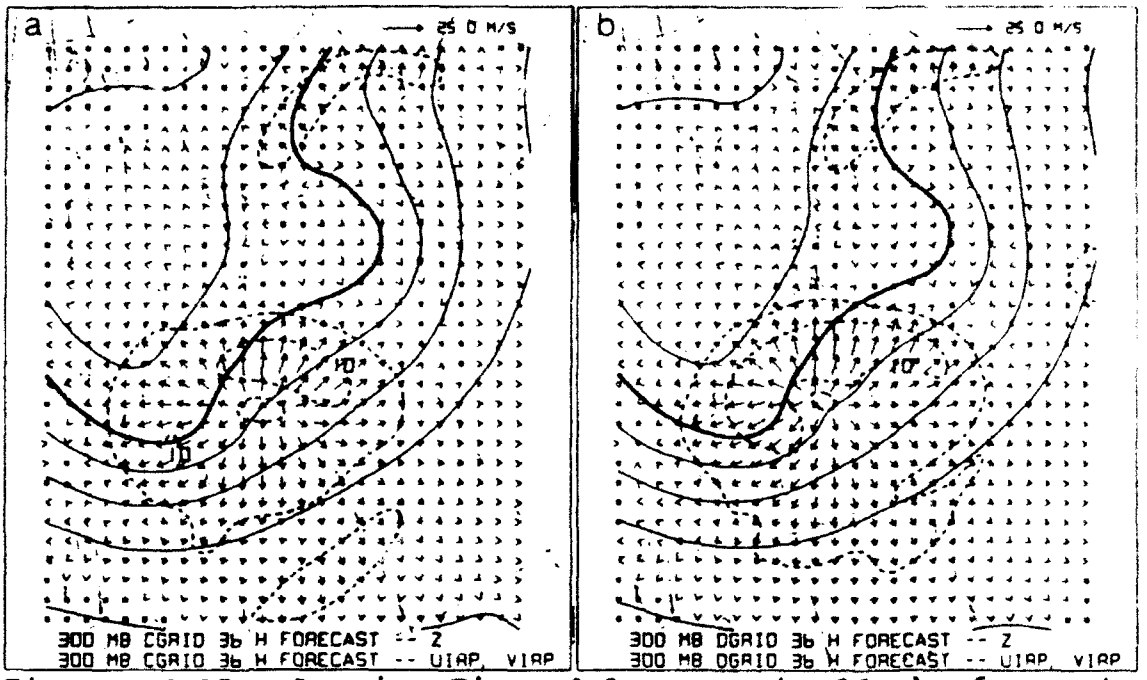

Figure 6.25. As in Fig. 6.3, except 36 h forecast, verification time 12Z/04

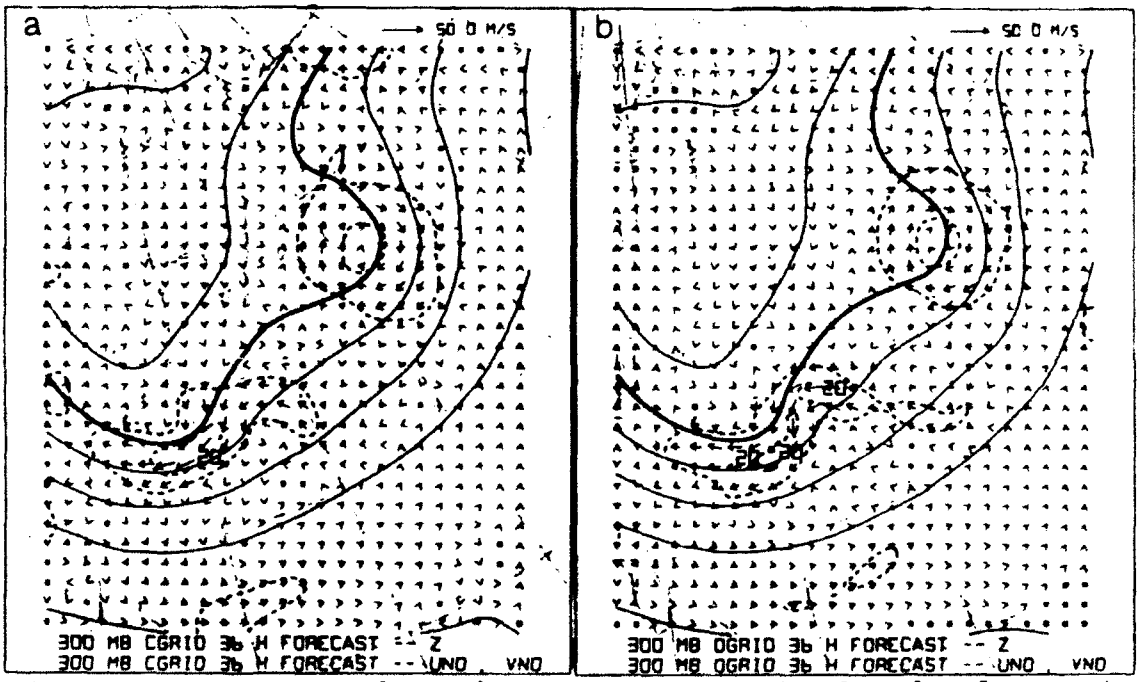

Figure 6.26. As in Fig. 6.4, except 36 h forecast, verification time 12Z/04

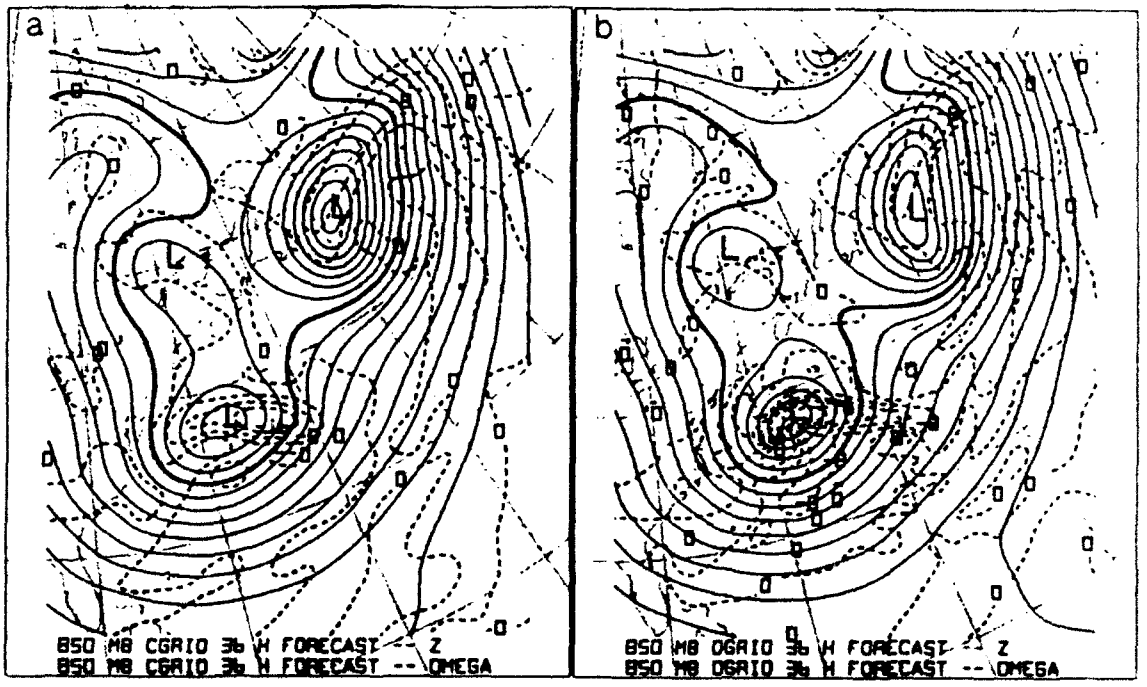

Figure 6.27. As in Fig. 6.5, except 36 h forecast, verification time 12Z/04

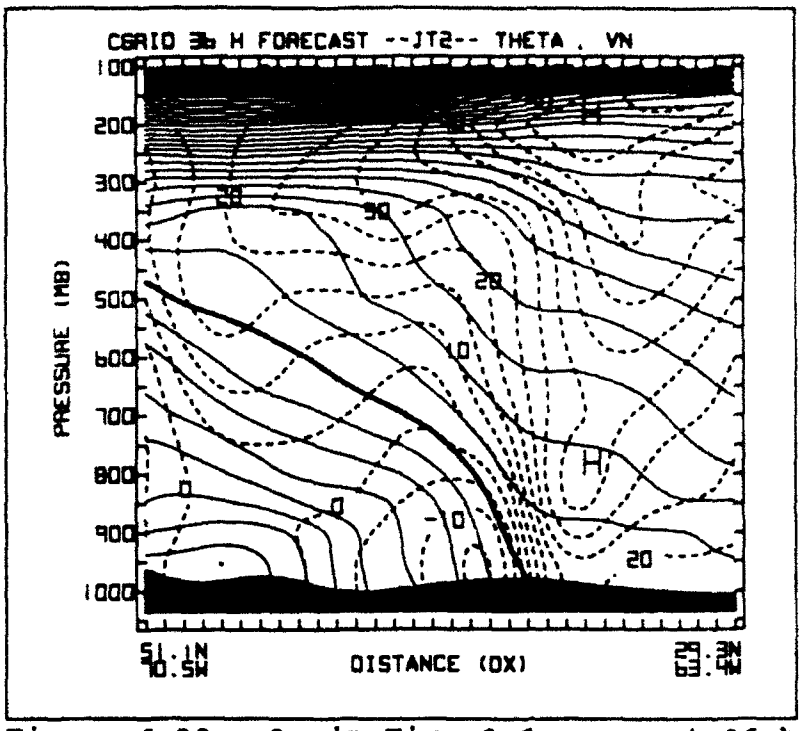

Figure 6.28a. As in Fig. 6.6a, except 36 h forecast, verification time 12Z/04

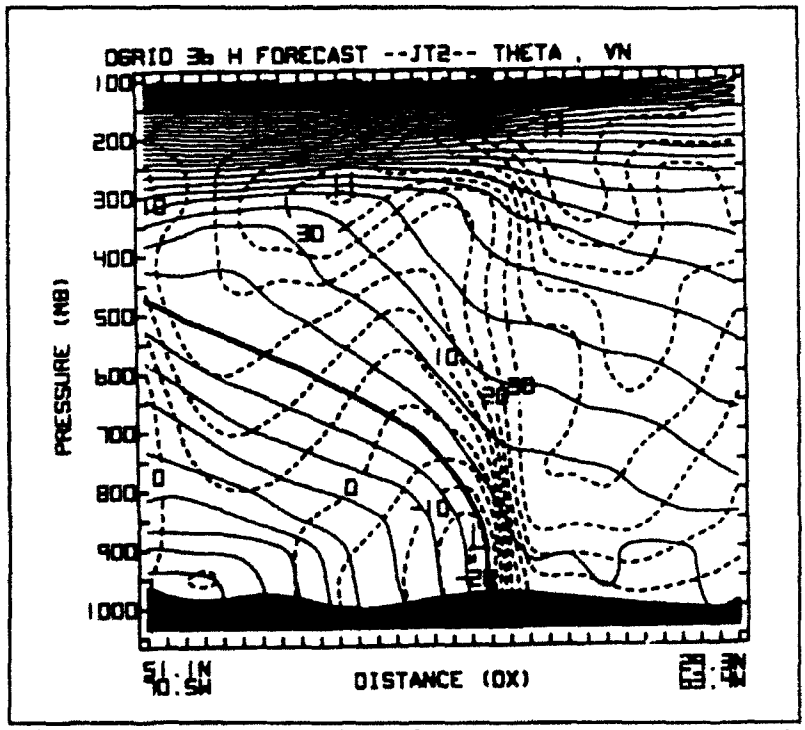

Figure 6.28b. As in Fig. 6.6b, except 36 h forecast, verification time 12Z/04

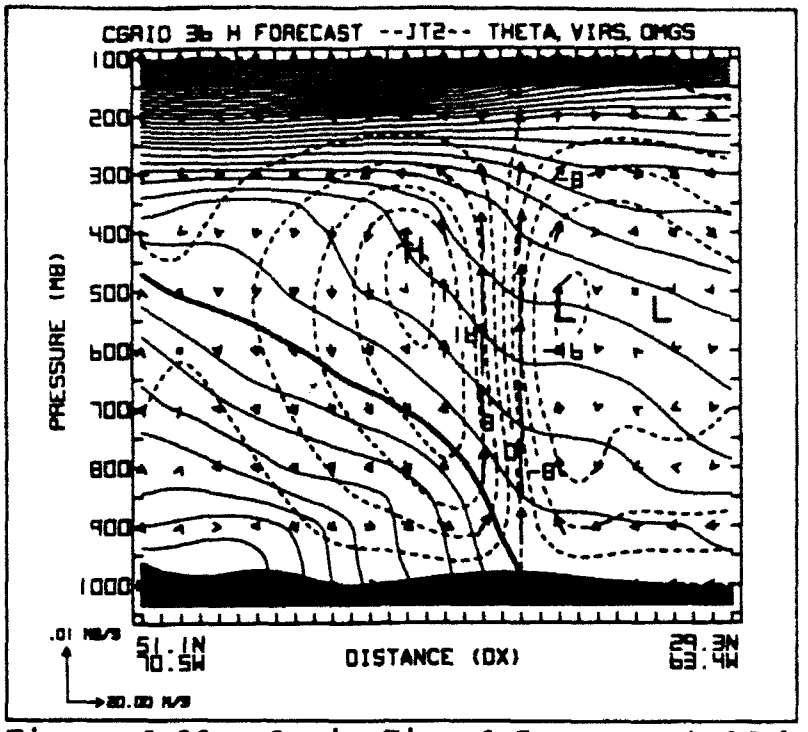

Figure 6.29a. As in Fig. 6.7a, except 36 h forecast, verification time 122/04

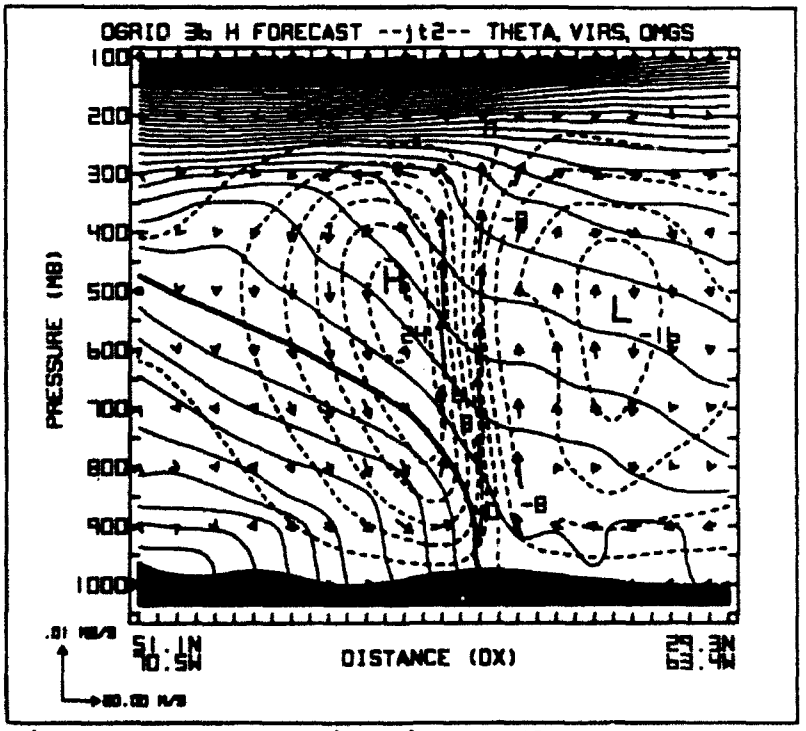

Figure 6.29b. As in Fig. 6.7b, except 36 h forecast, verification time 012/04

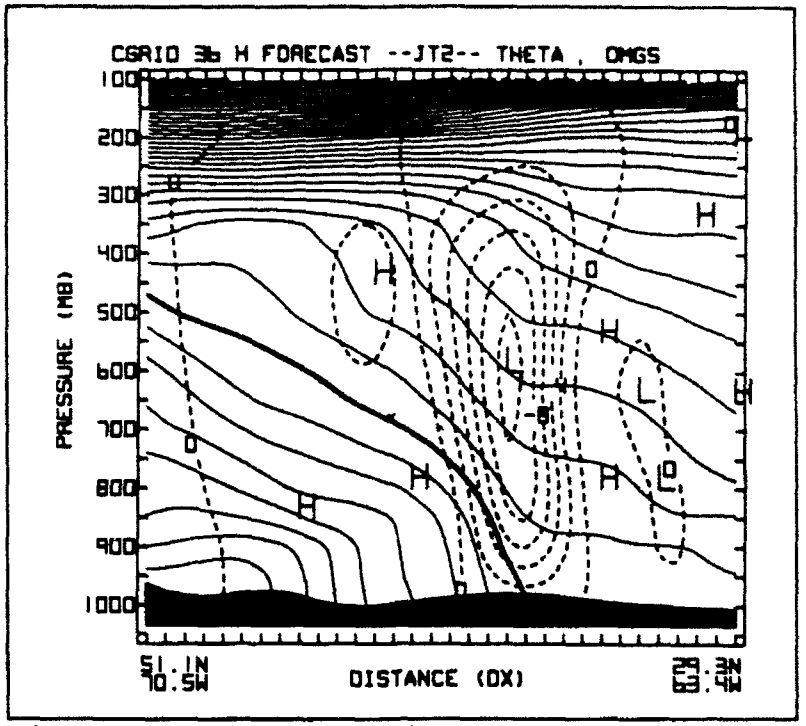

Figure 6.30a. As in Fig. 6.8a, except 36 h forecast, verification time 12Z/04

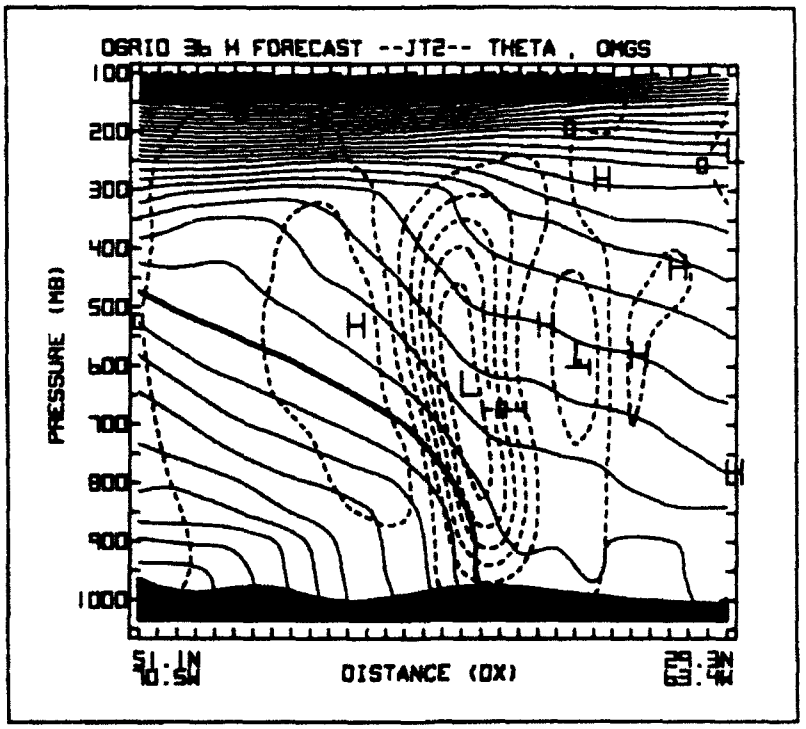

Figure 6.30b. As in Fig. 6.8b, except 36 forecast, verification time 12Z/04

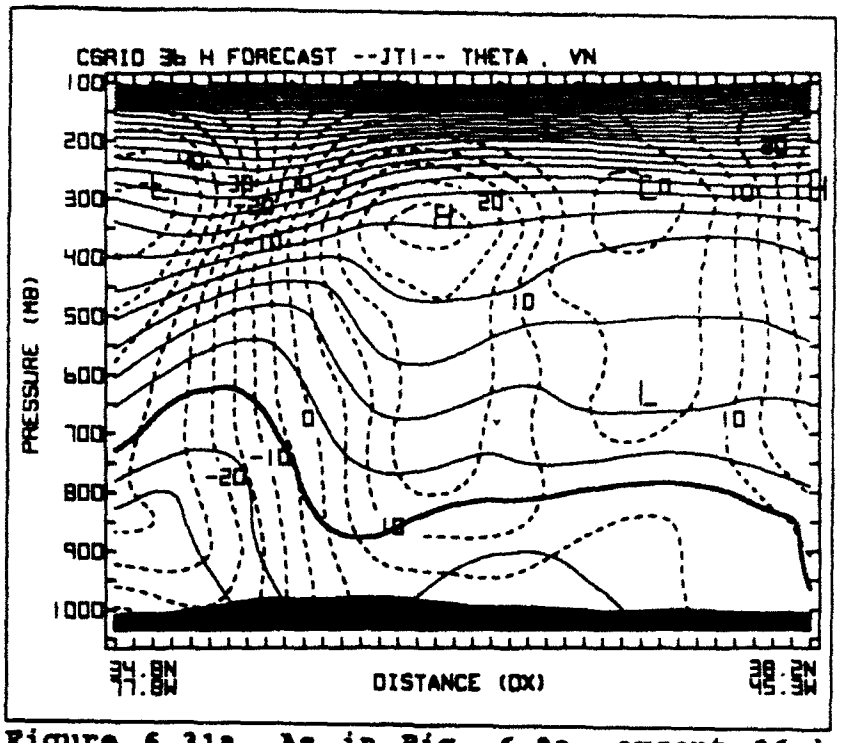

Figure 6.31a. As in Fig. 6.9a, except 36 h forecast, verification time 12Z/04

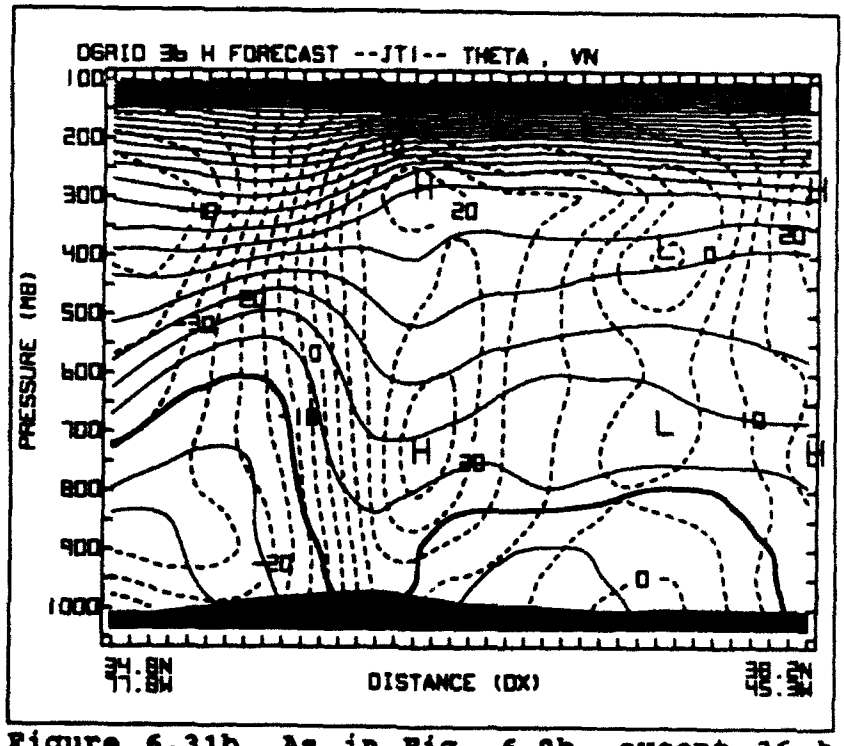

Figure 6.31b. As in Fig. 6.9b, except 36 h forecast, verification time 12Z/04

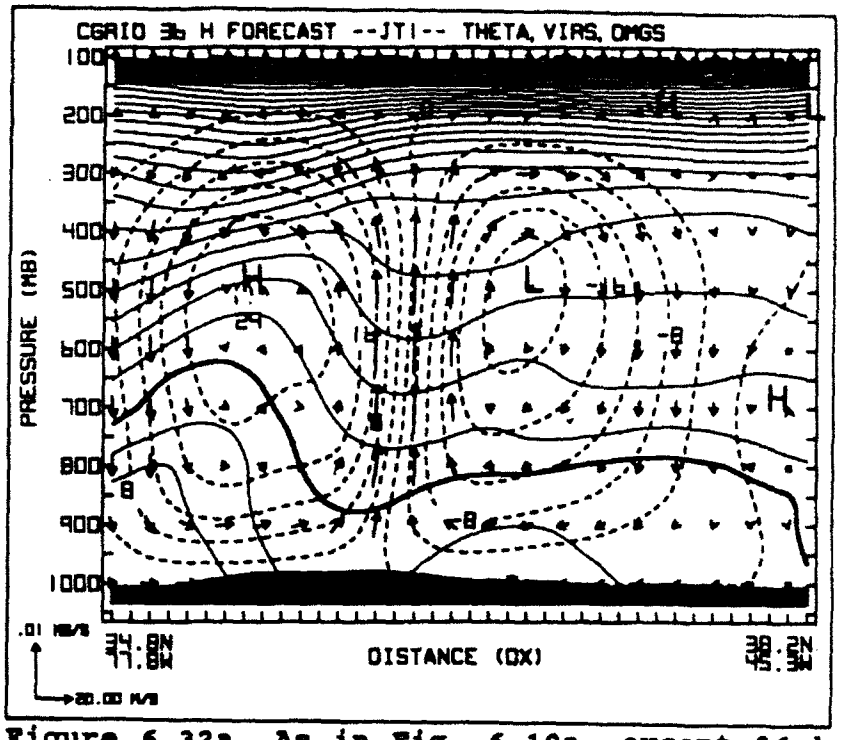

Figure 6.32a. As in Fig. 6.10a, except 36 h forecast, verification time 12Z/04

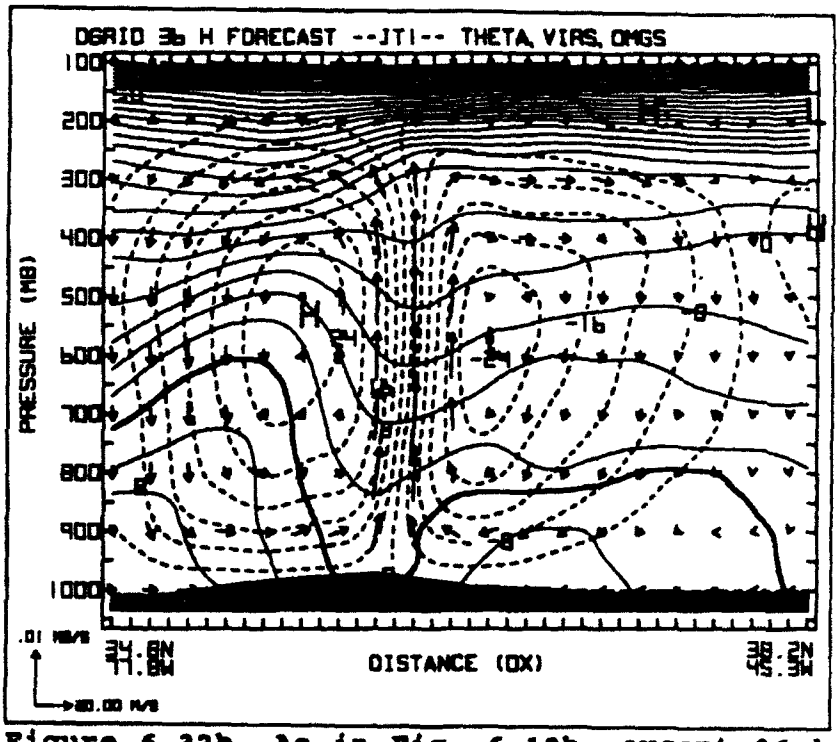

Figure 6.32b. As in Fig. 6.10b, except 36 h forecast, verification time 12Z/04

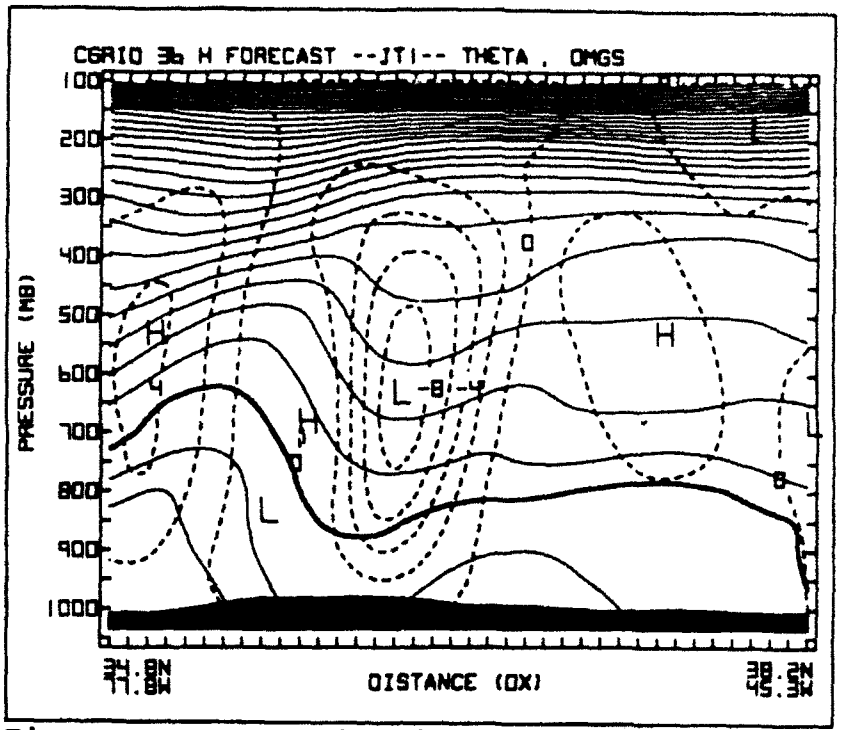

Figure 6.33a. As in Fig. 6.11a, except 36 h forecast, verification time 12Z/04

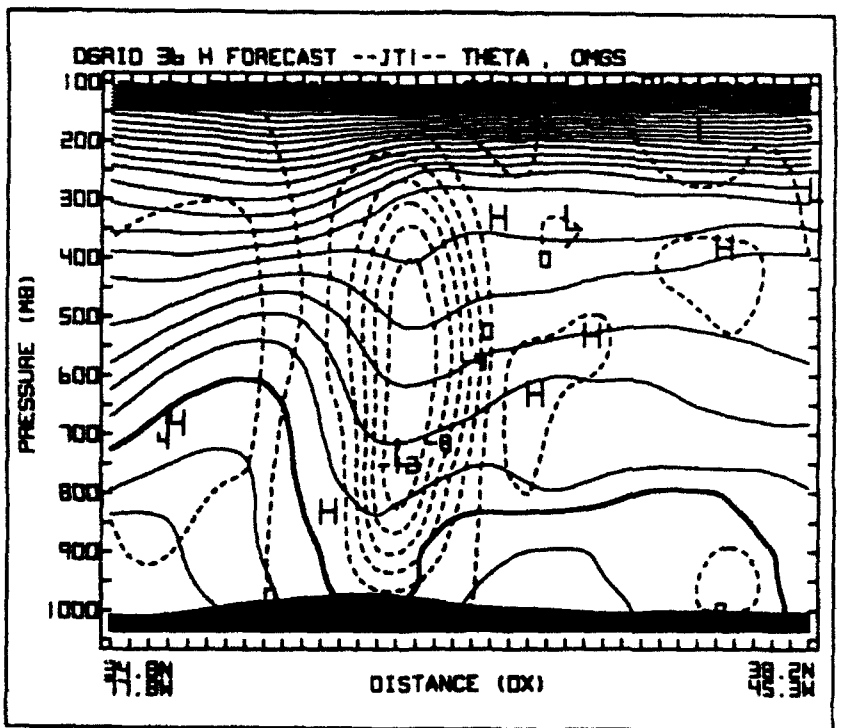

Figure 6.33b. As in Fig. 6.11b, except 36 h forecast, verification time 12Z/04

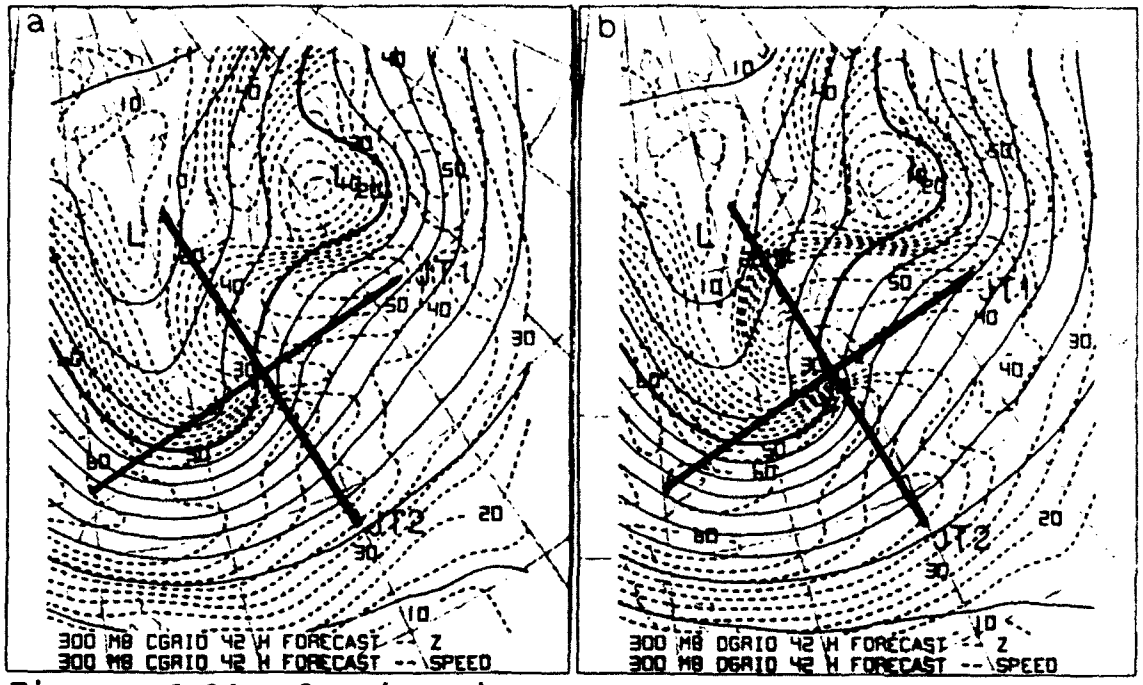

Figure 6.34. As in Fig. 6.1, except 42 h forecast, verification time 18Z/04

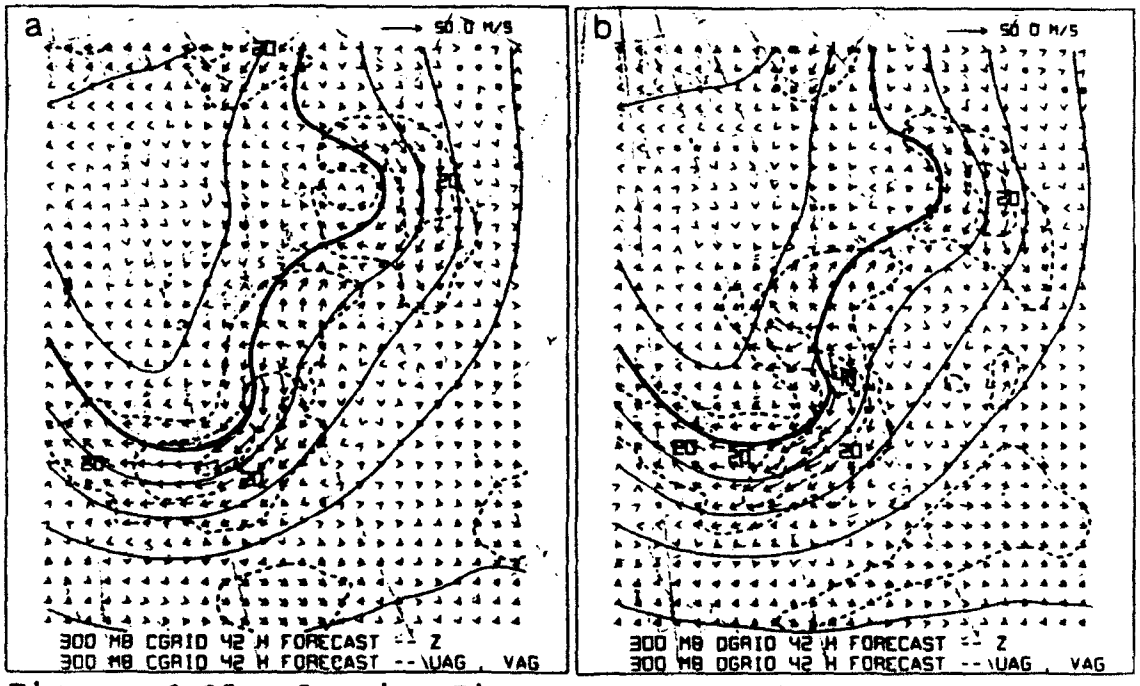

Figure 6.35. As in Fig. 6.2, except 42 h forecast, verification time 18Z/04

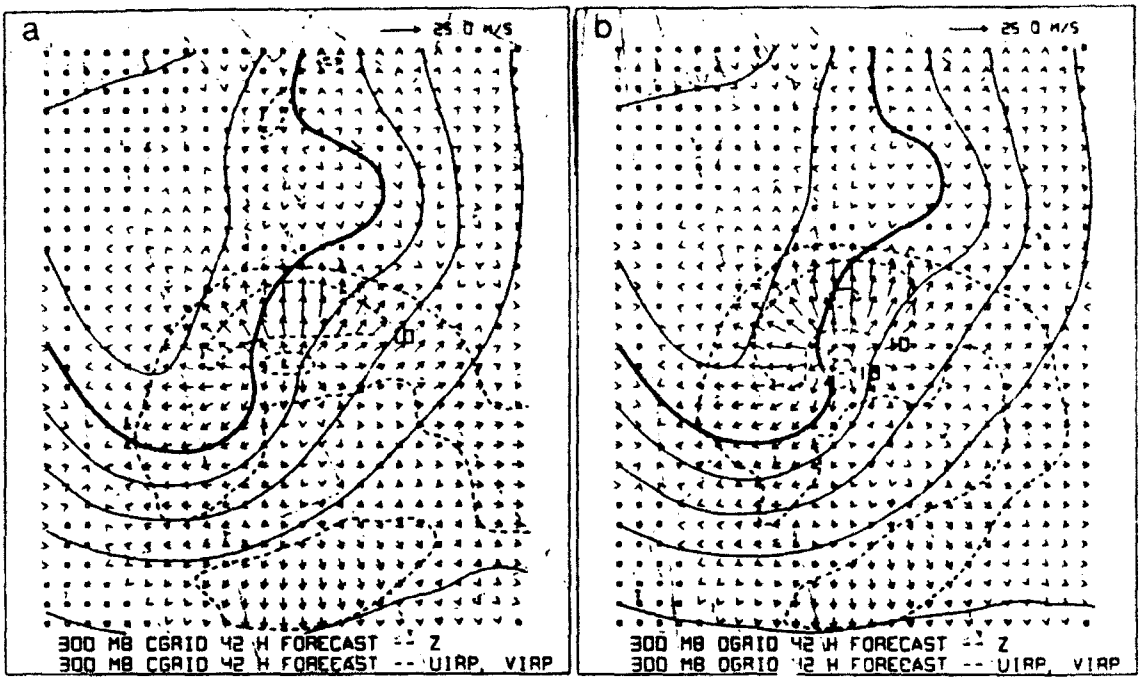

Figure 6.36. As in Fig. 6.3, except 42 h forecast, verification time 18Z/04

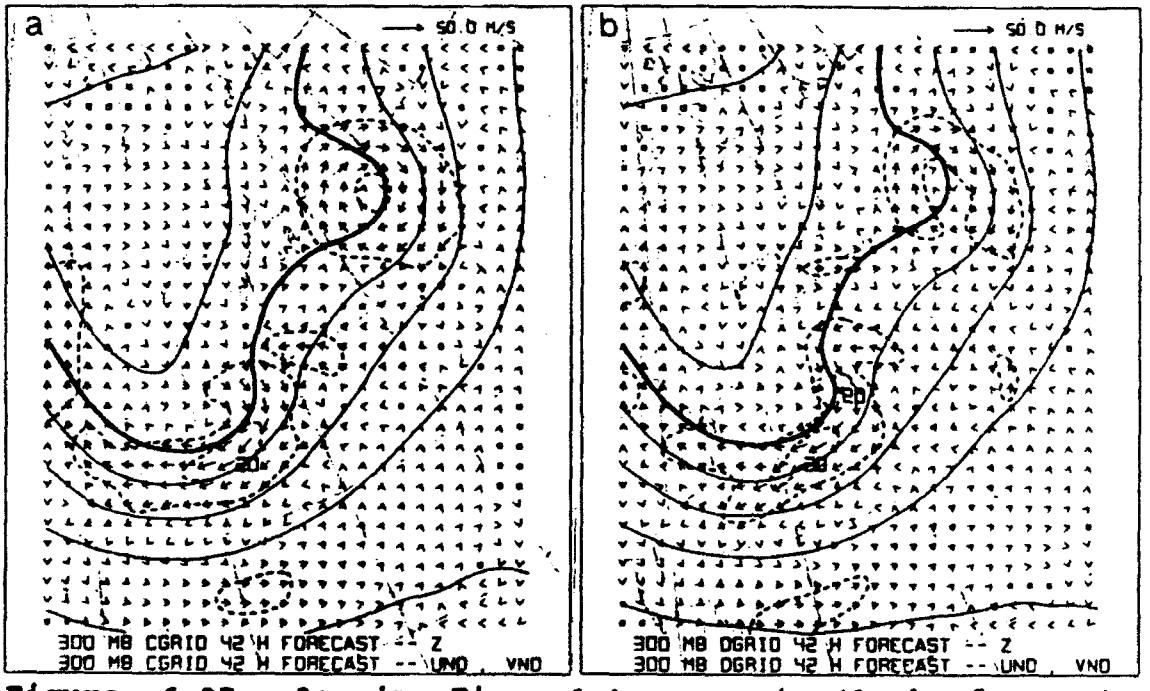

Figure 6.37. As in Fig. 6.4, except 42 h forecast, verification time 18Z/04

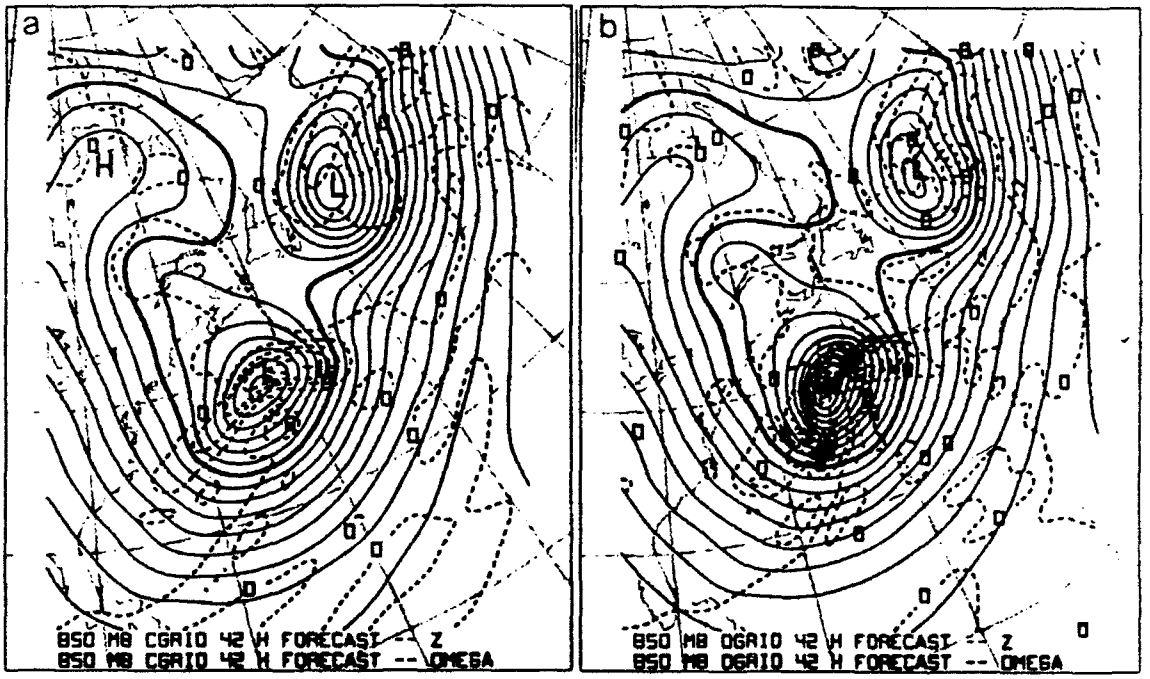

Figure 6.38. As in Fig. 6.5, except 42 h forecast, verification time 18Z/04

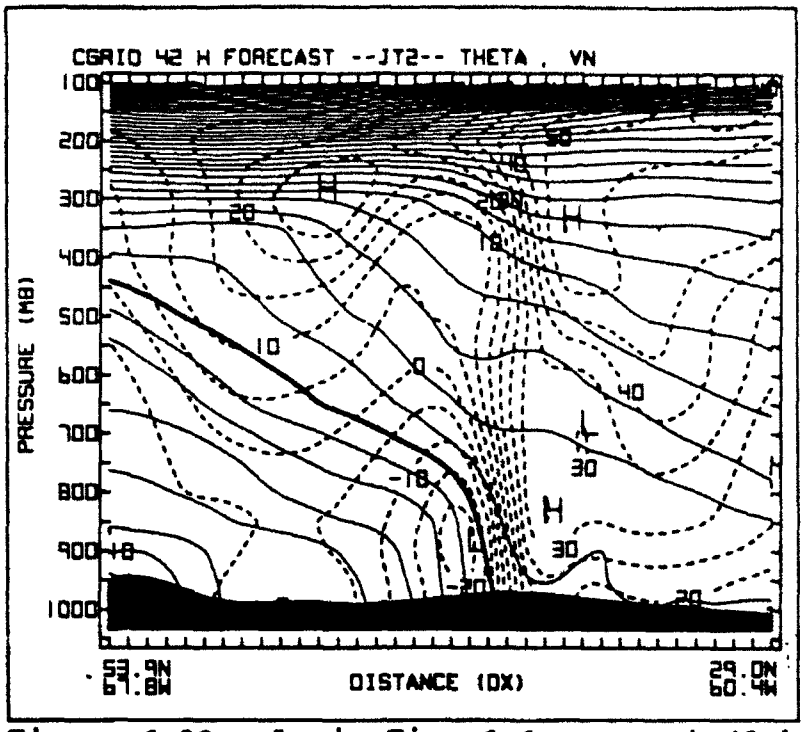

Figure 6.39a. As in Fig. 6.6a, except 42 h forecast, verification time 18Z/04

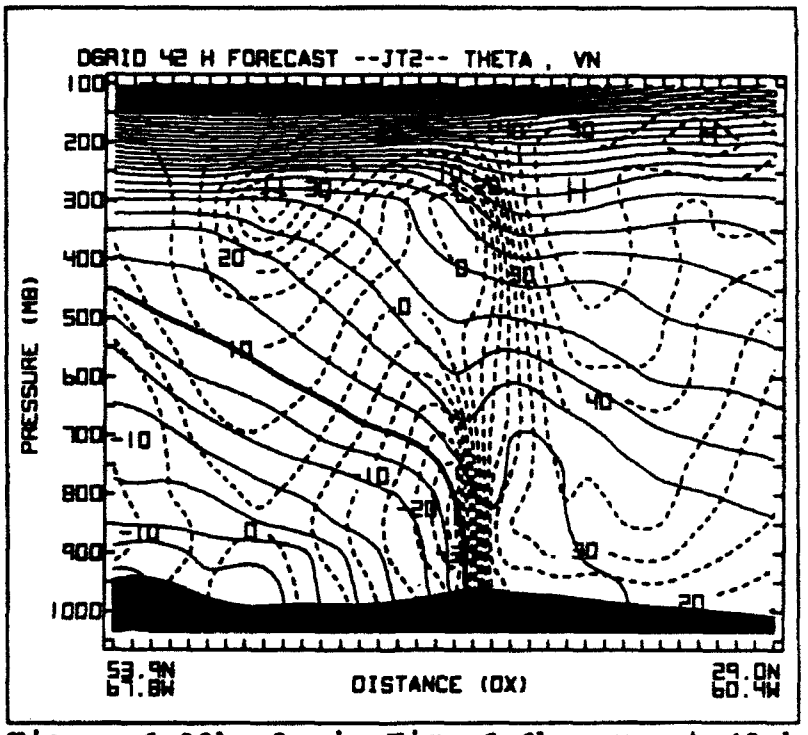

Figure 6.39b. As in Fig. 6.6b, except 42 h forecast, verification time 18Z/04

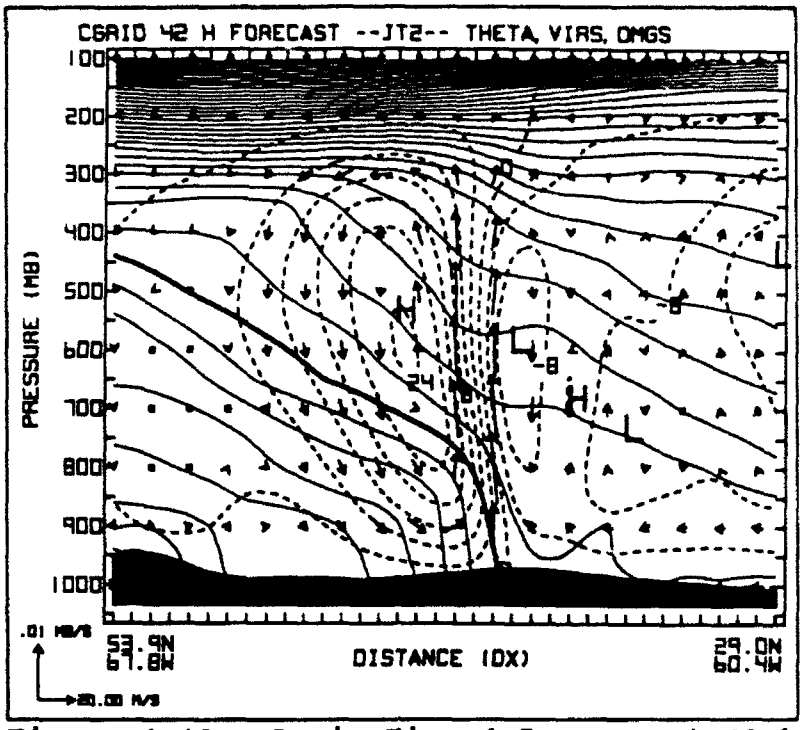

Figure 6.40a. As in Fig. 6.7a, except 42 h forecast, verification time 18Z/04

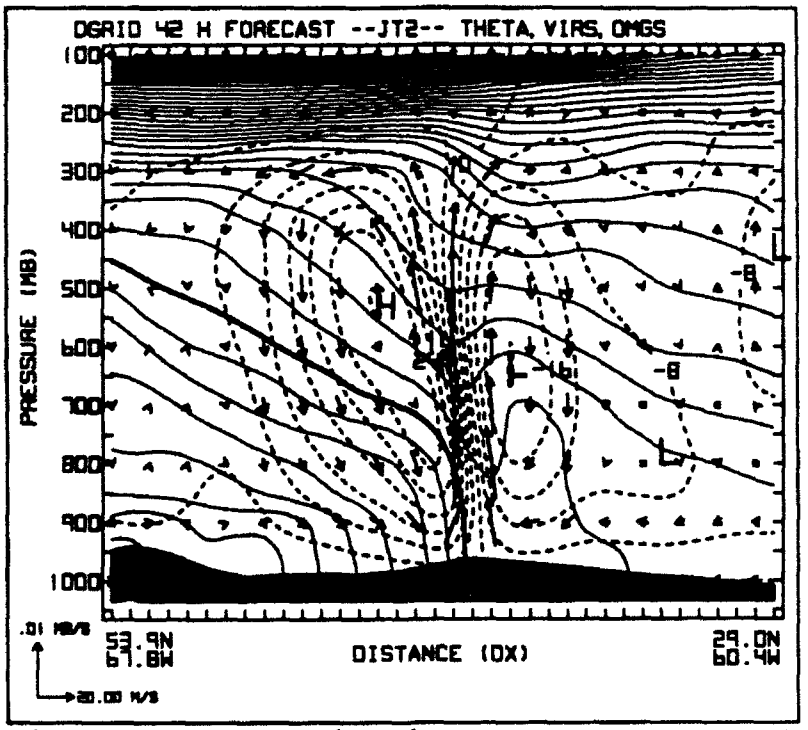

Figure 6.40b. As in Fig. 6.7b, except 42 h forecast, verification time 18Z/04

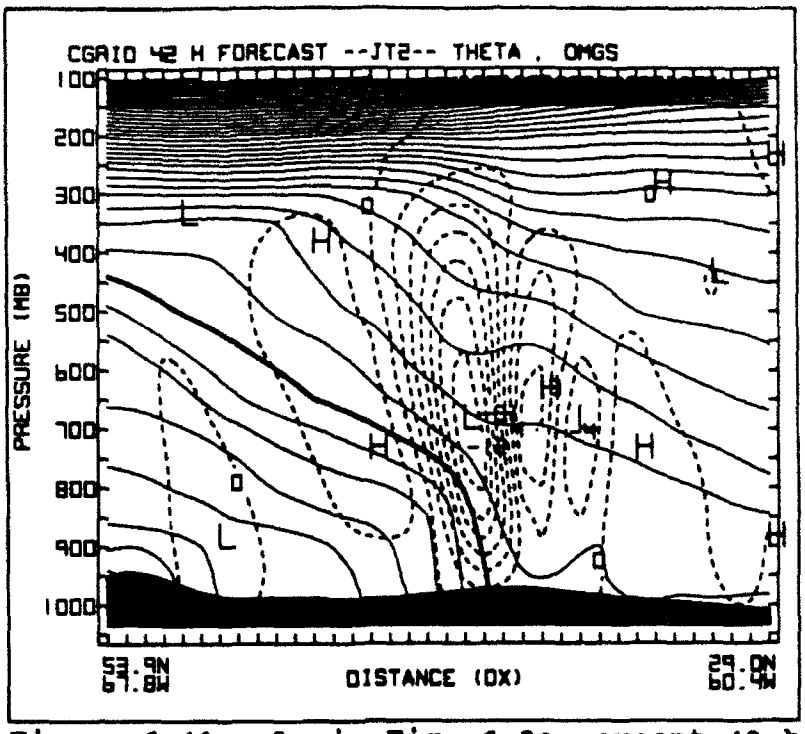

Figure 6.41a. As in Fig. 6.8a, except 42 h forecast, verification time 18Z/04

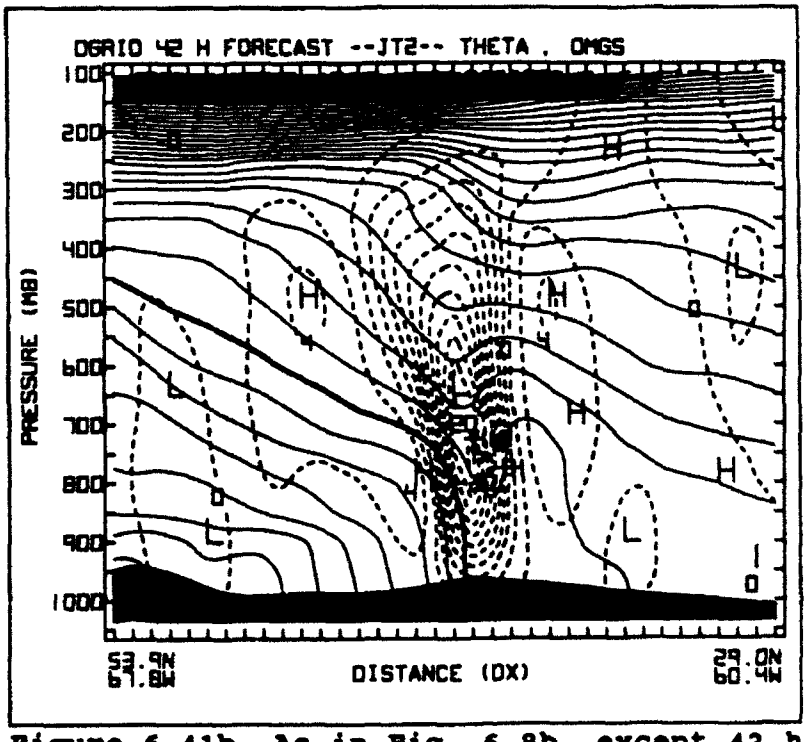

Figure 6.41b. As in Fig. 6.8b, except 42 h forecast, verification time 18Z/04

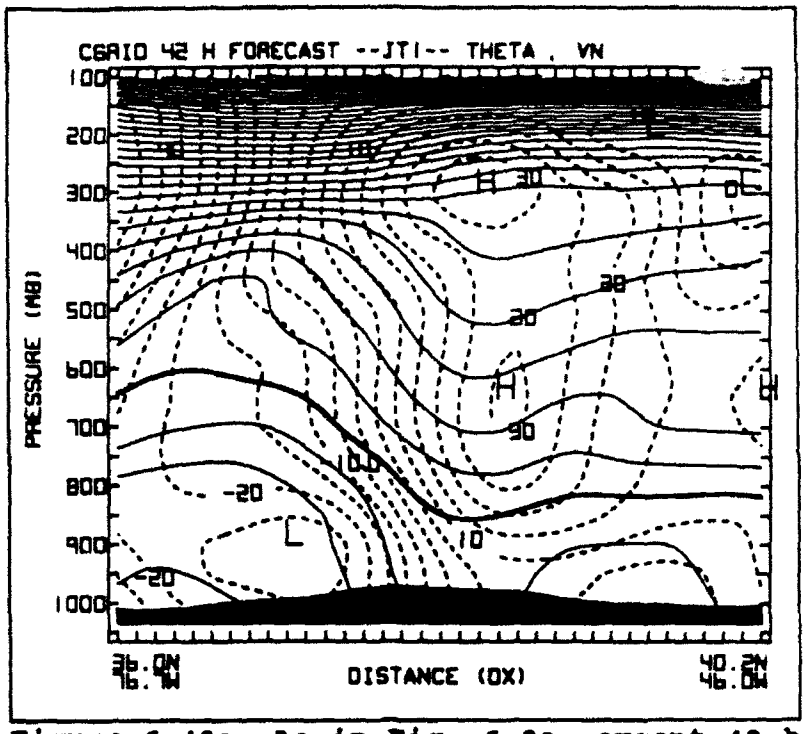

Figure 6.42a. As in Fig. 6.9a, except 42 h forecast, verification time 18Z/04

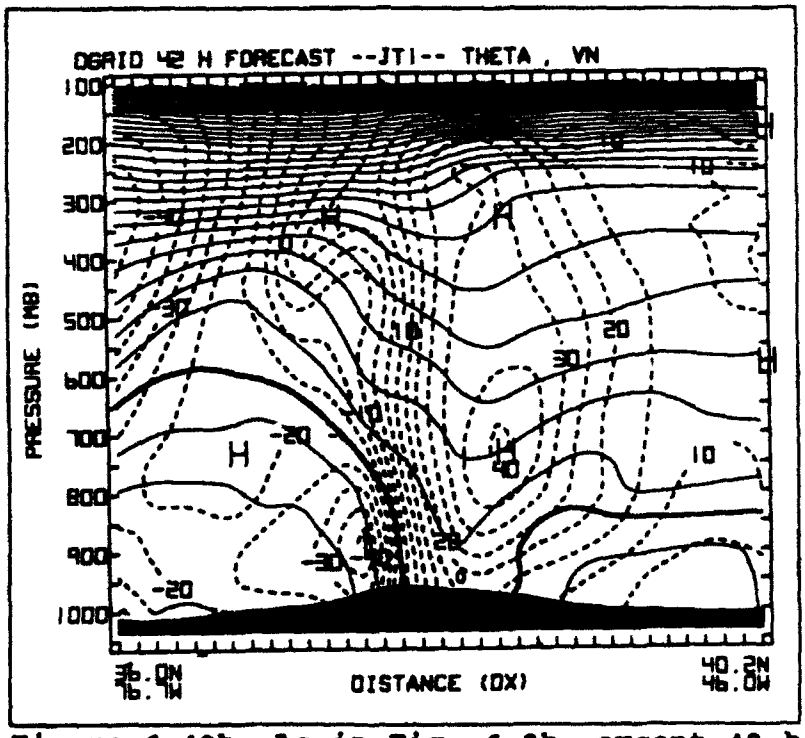

Figure 6.42b. As in Fig. 6.9b, except 42 h forecast, verification time 18Z/04

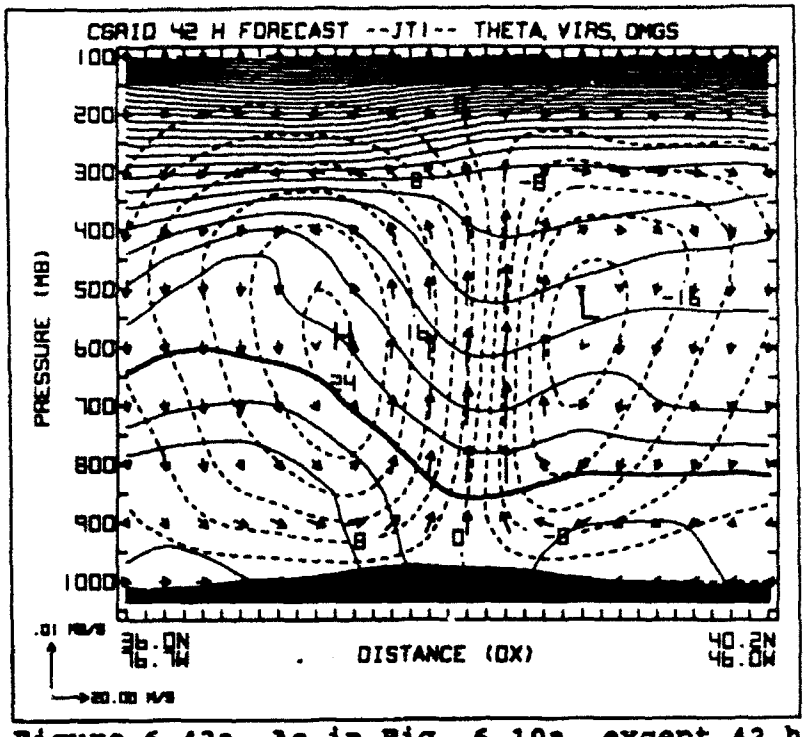

Figure 6.43a. As in Fig. 6.10a, except 42 h forecast, verification time 18Z/04

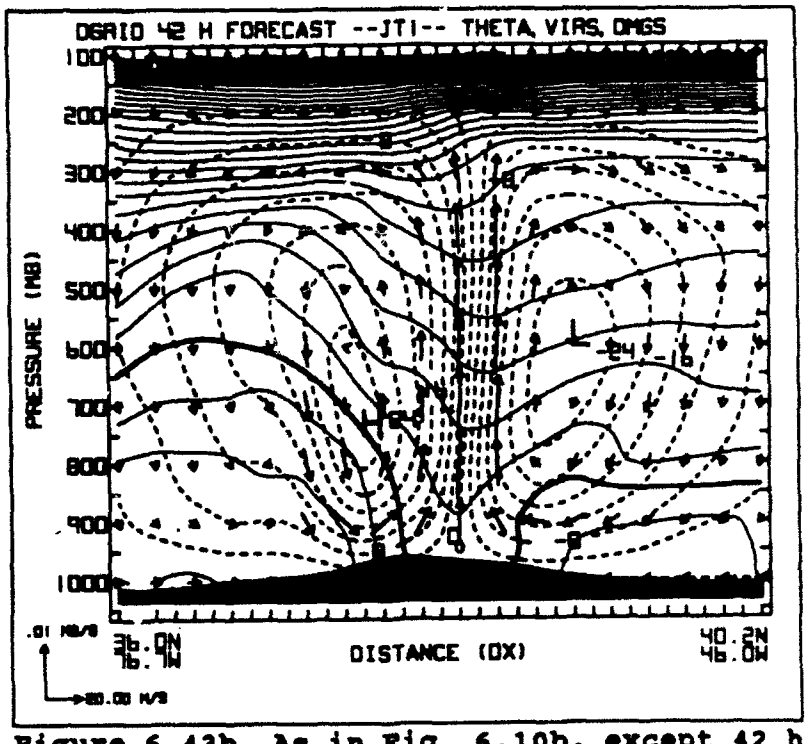

Figure 6.43b. As in Fig. 6.10b, except 42 h forecast, verification time 18Z/04

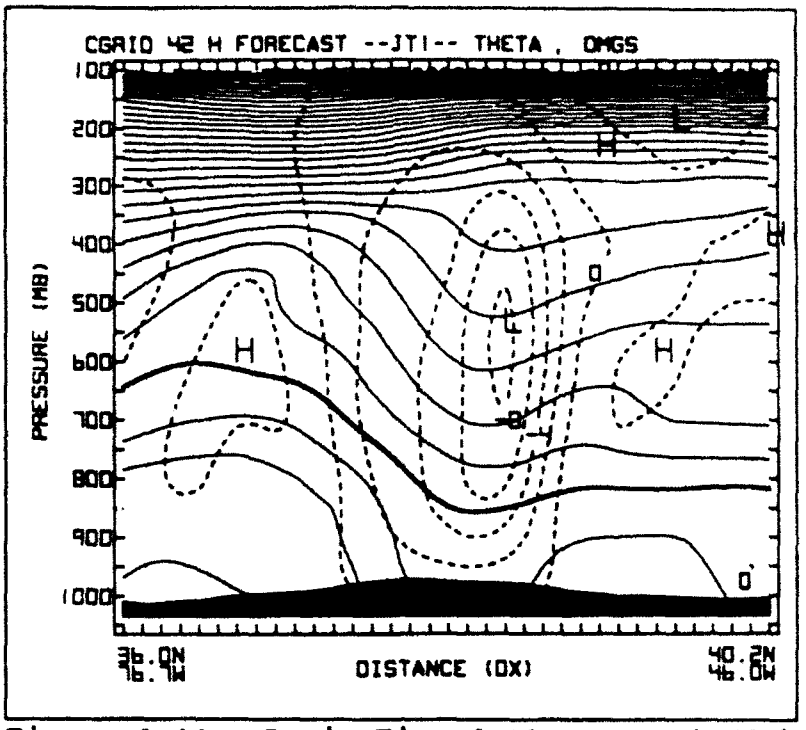

Figure 6.44a. As in Fig. 6.11a, except 42 h forecast, verification time 18Z/04

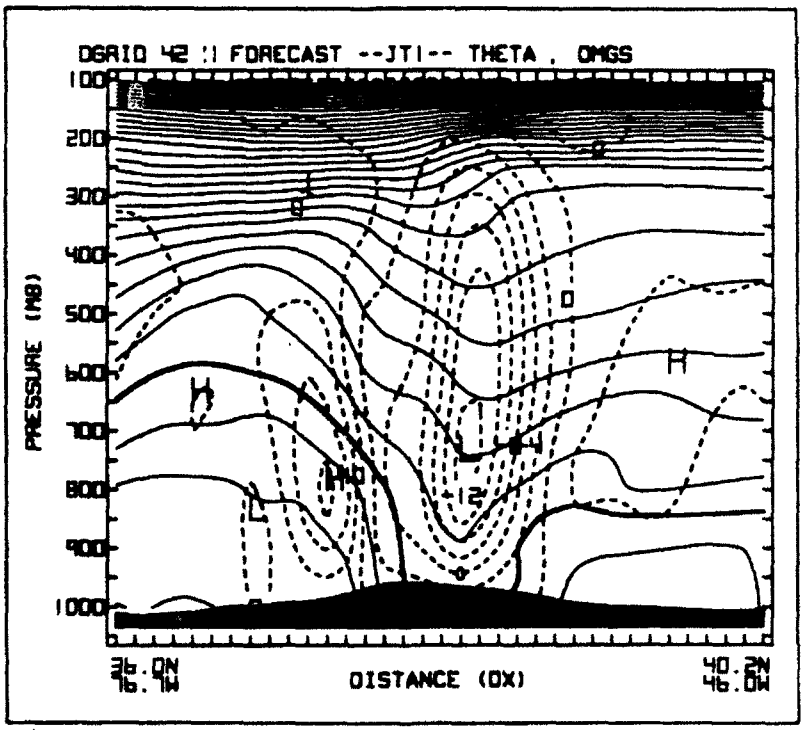

Figure 6.44b. As in Fig. 6.11b, except 42 h forecast, verification time 18Z/04

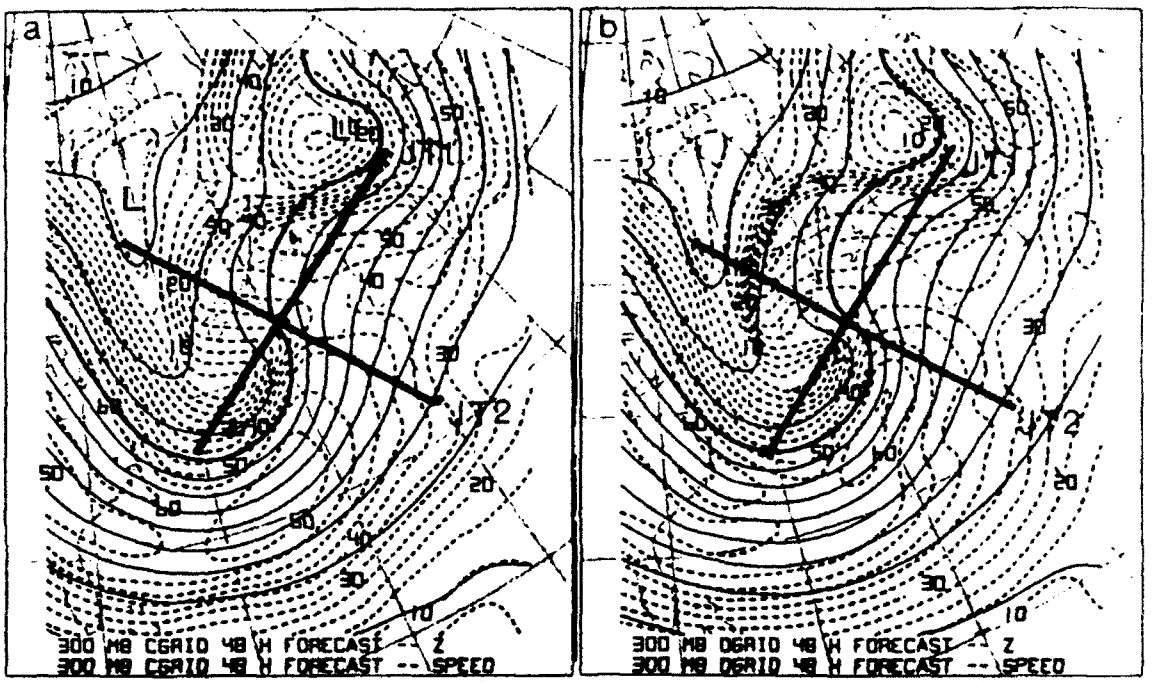

Figure 6.45. As in Fig. 6.1, except 48 h forecast, verification time 00Z/05

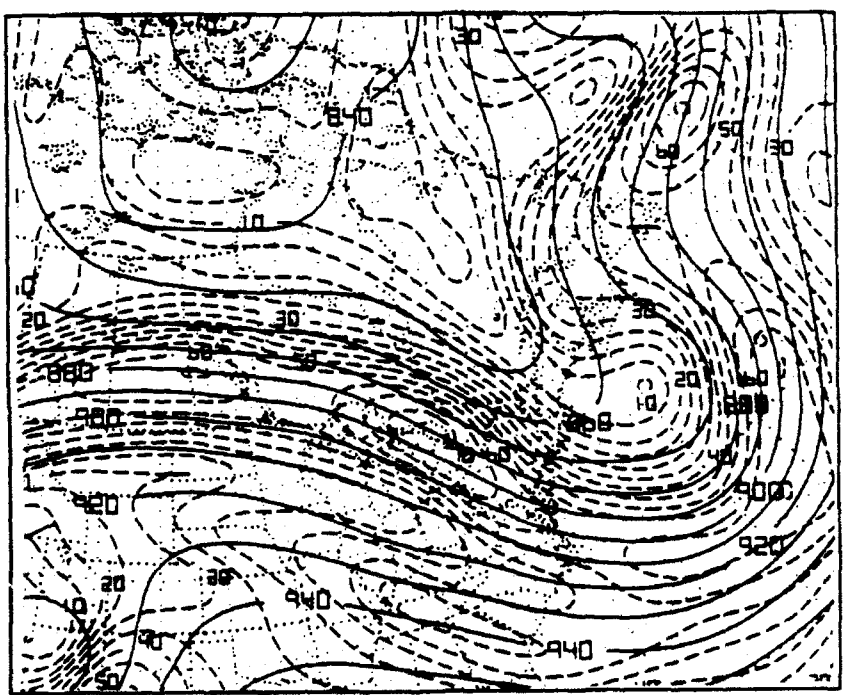

Figure 6.45c. As in Fig. 6.1c, except 00Z/05

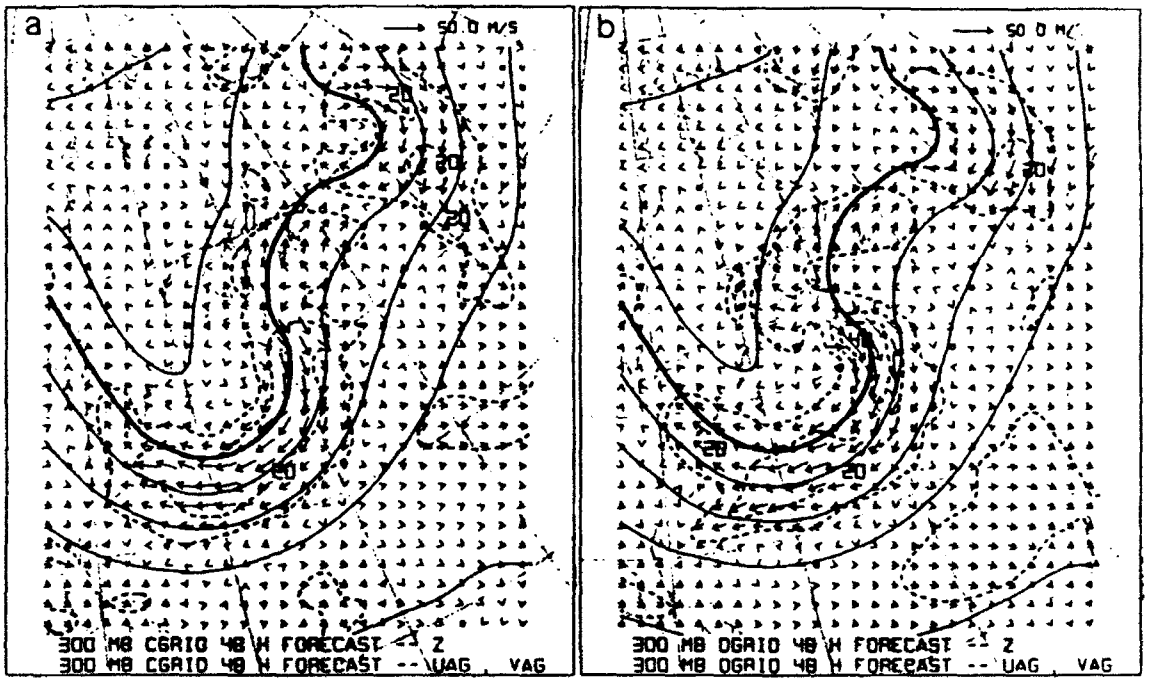

Figure 6.46. As in Fig. 6.2, except 48 h forecast, verification time 00Z/05

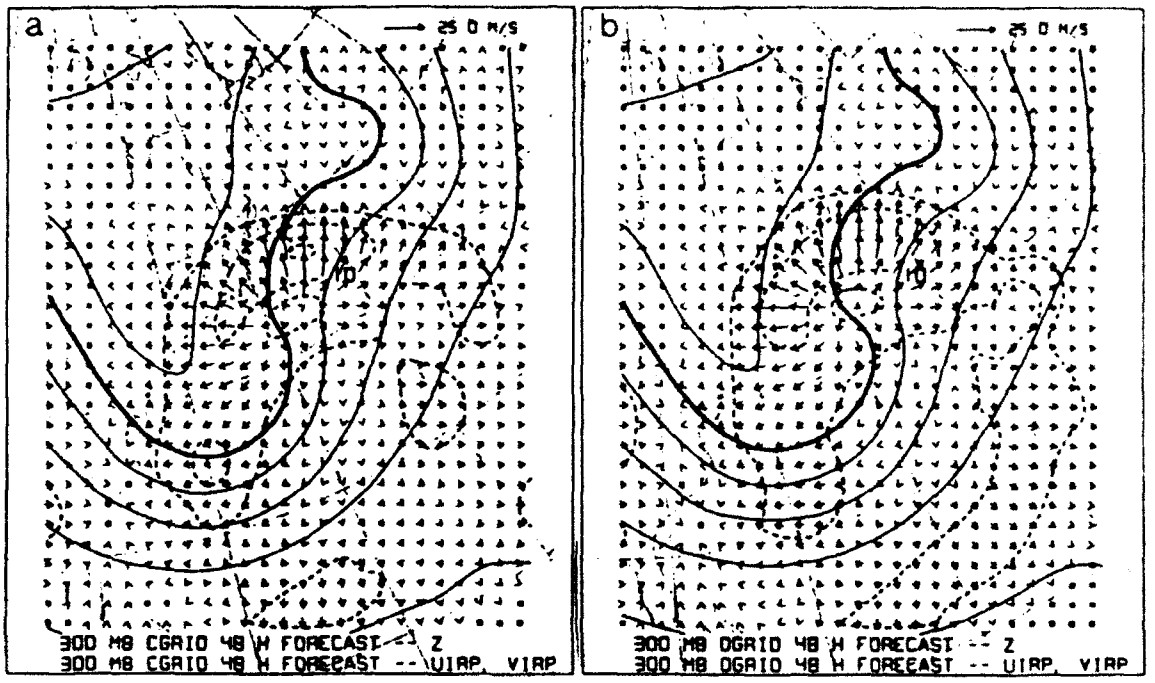

Figure 6.47. As in Fig. 6.3, except 48 h forecast, verification time 00Z/05

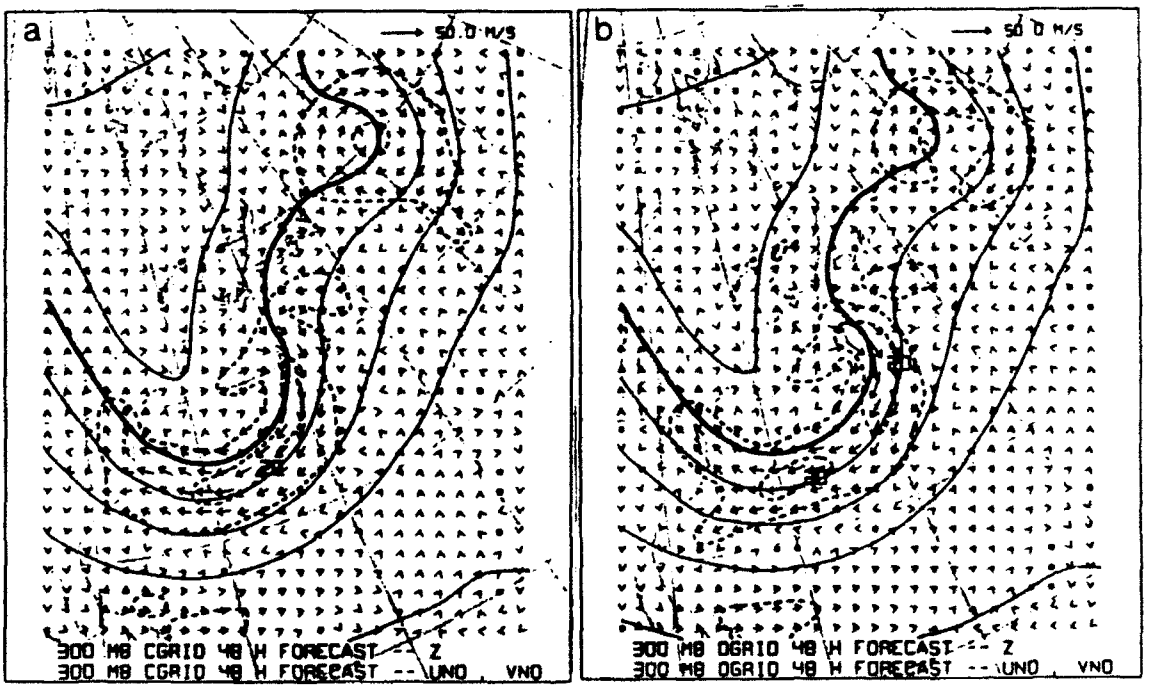

Figure 6.48. As in Fig. 6.4, except 48 h forecast, verification time 00Z/05

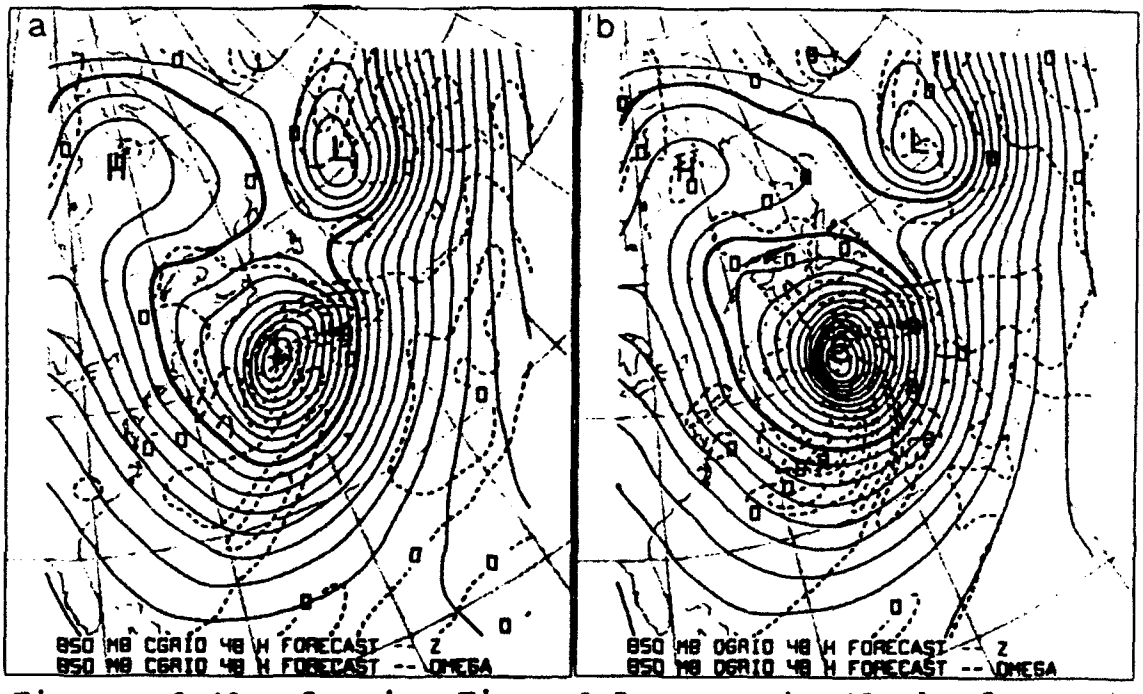

Figure 6.49. As in Fig. 6.5, except 48 h forecast, verification time 00Z/05

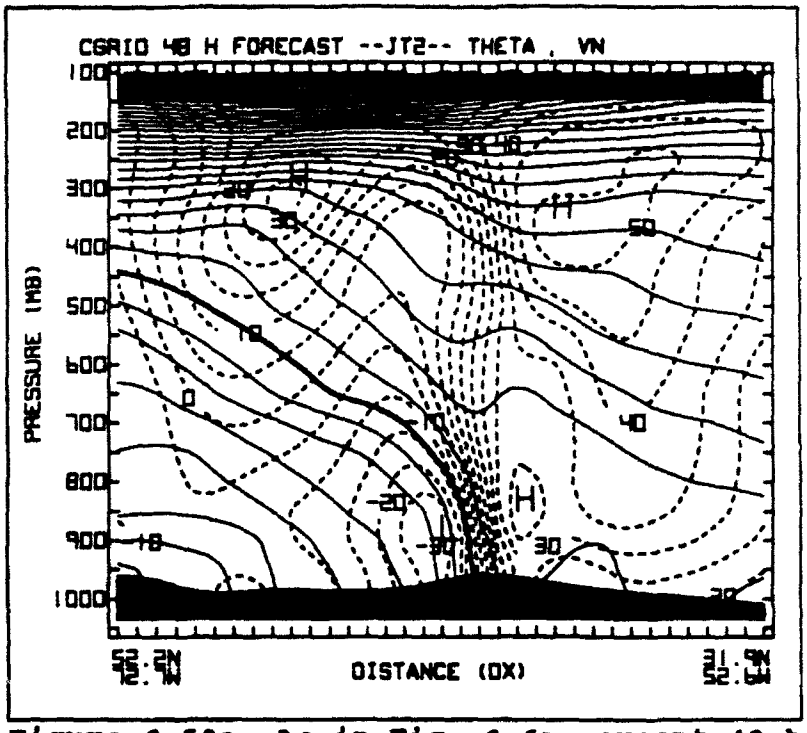

Figure 6.50a. As in Fig. 6.6a, except 48 h forecast, verification time 00Z/05

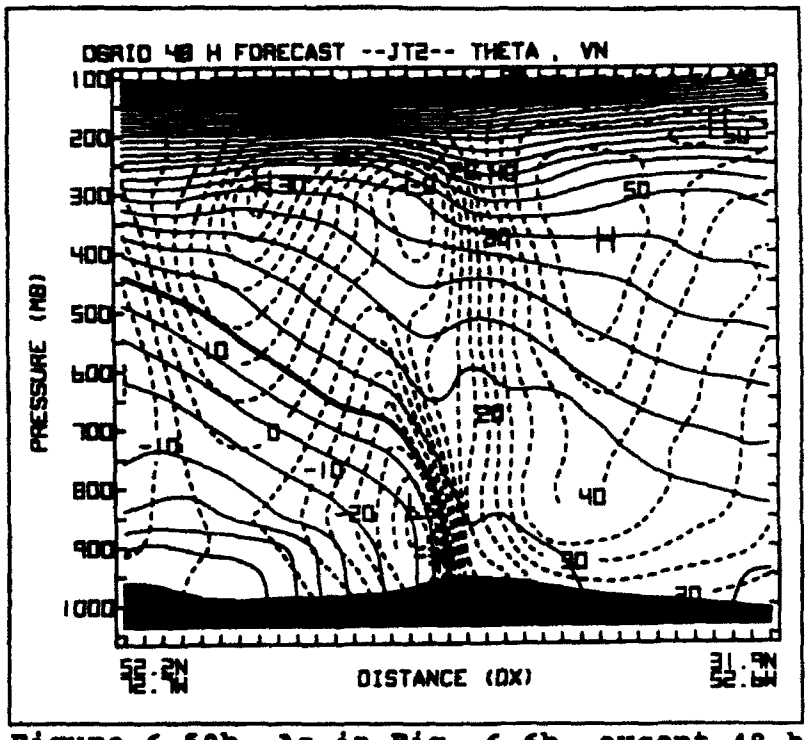

Figure 6.50b. As in Fig. 6.6b, except 48 h forecast, verification time 00Z/05

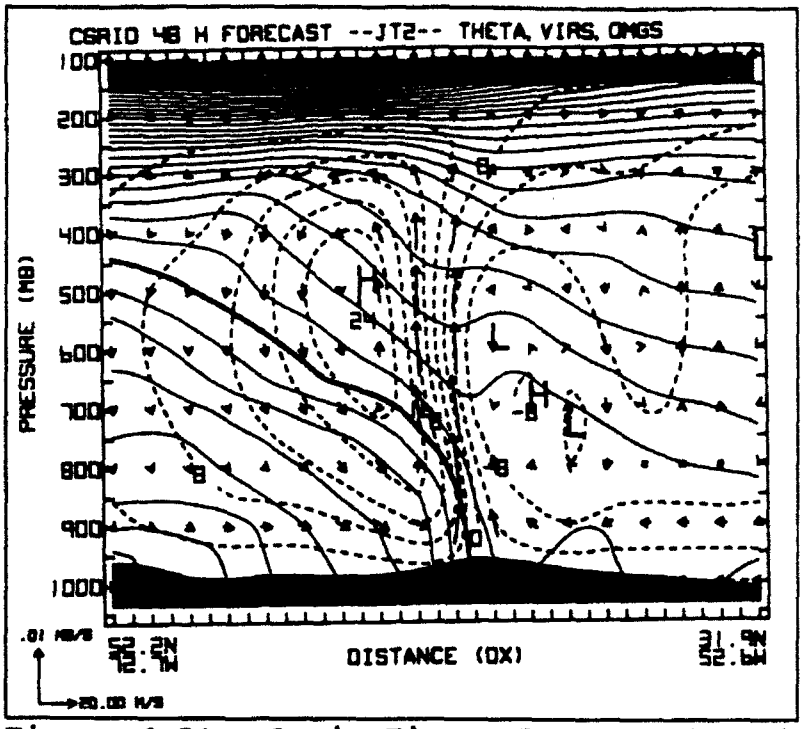

Figure 6.51a. As in Fig. 6.7a, except 48 h forecast, verification time 00Z/05

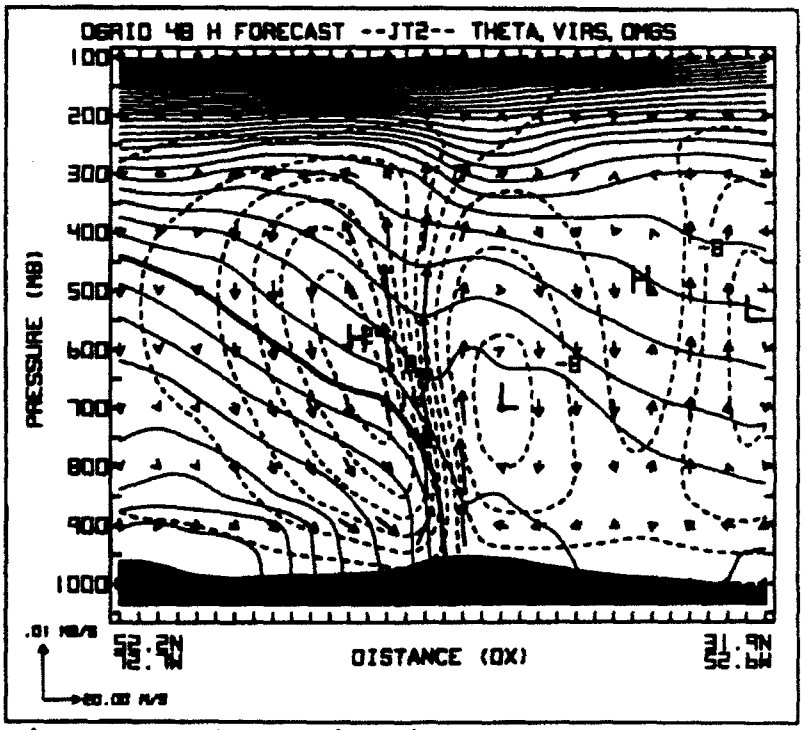

Figure 6.51b. As in Fig. 6.7b, except 48 h forecast, verification time 100/045

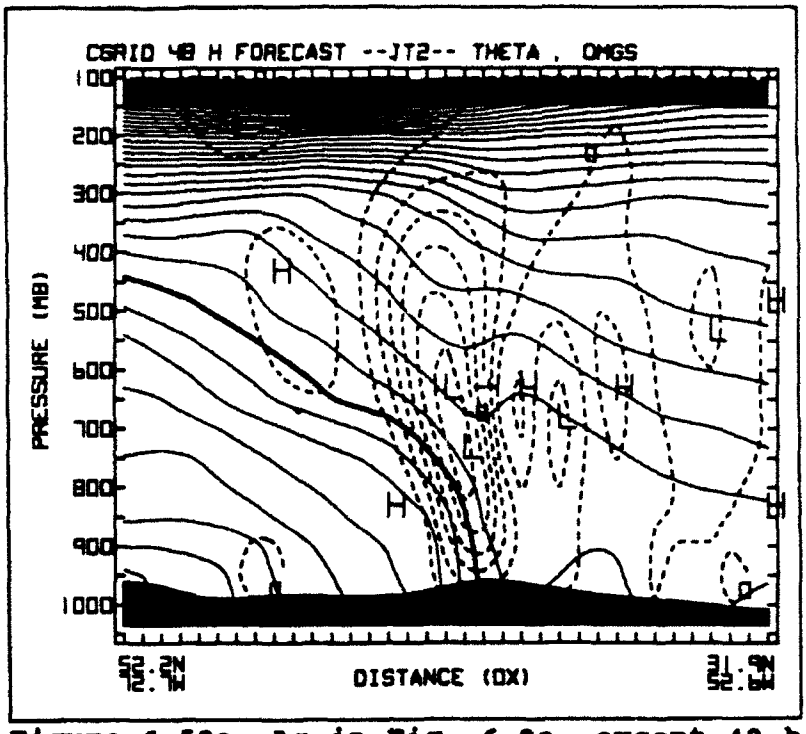

Figure 6.52a. As in Fig. 6.8a, except 48 h forecast, verification time 00Z/05

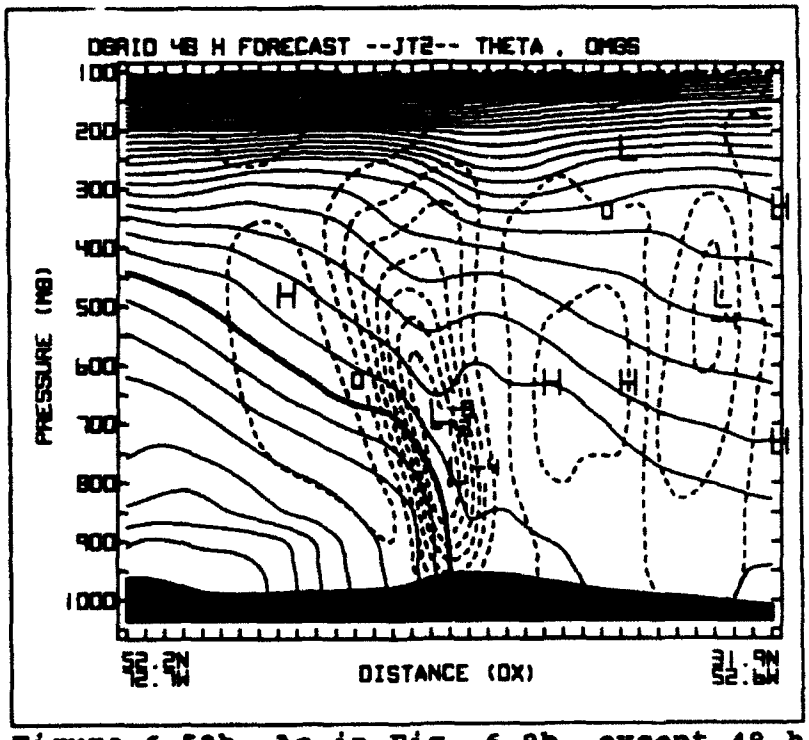

Figure 6.52b. As in Fig. 6.8b, except 48 h forecast, verification time 00Z/05

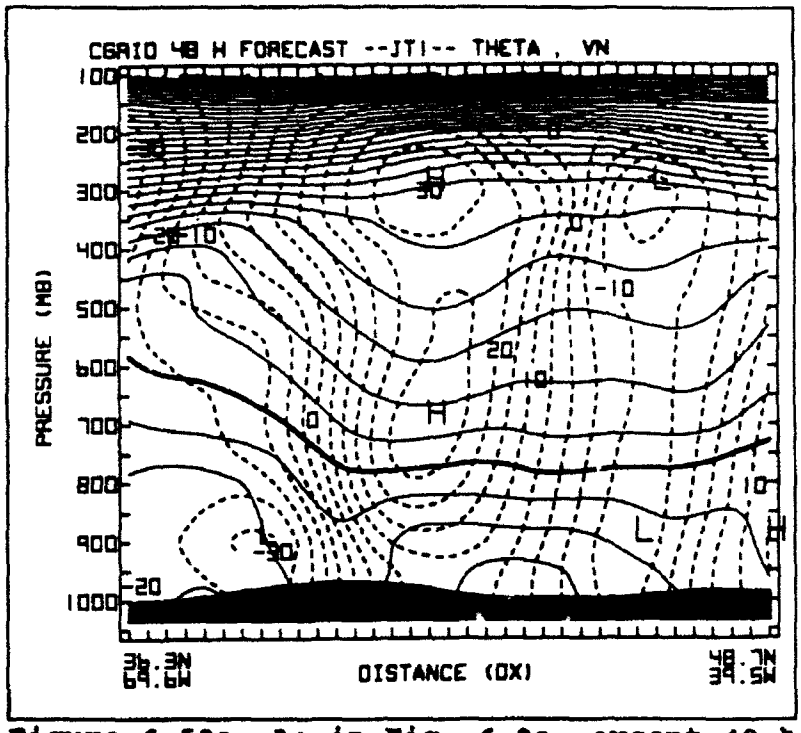

Figure 6.53a. As in Fig. 6.9a, except 48 h forecast, verification time 00Z/05

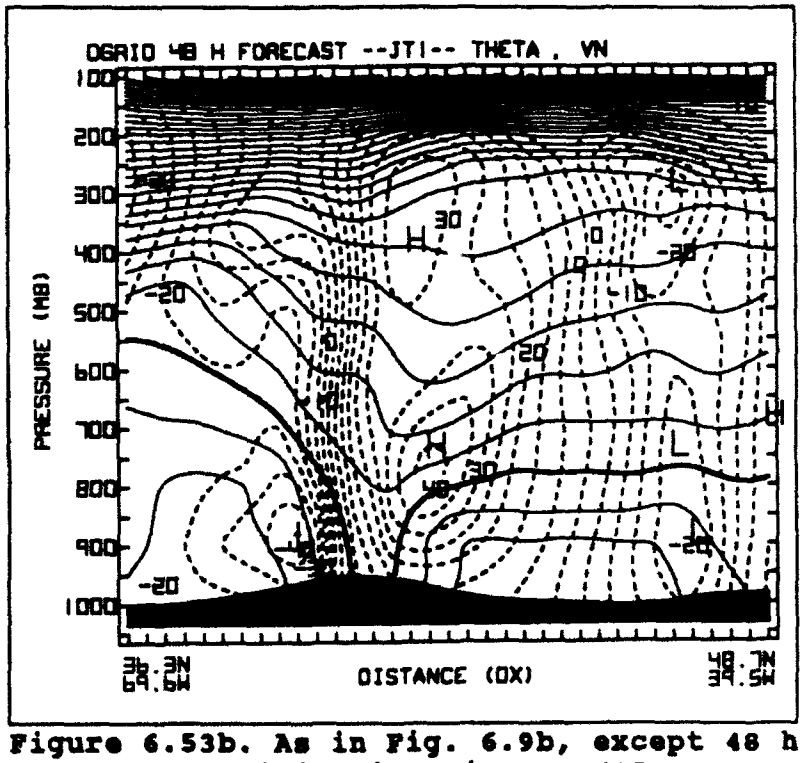

Figure 6.53b. As in Fig. 6.9b, except 48 h forecast, verification time 00Z/05

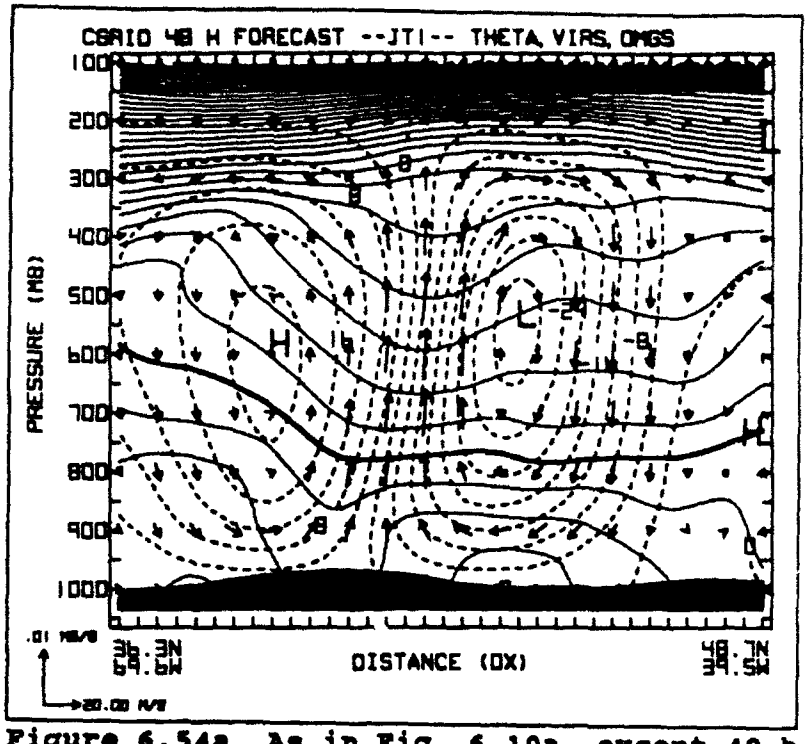

Figure 6.54a. As in Fig. 6.10a, except 48 h forecast, verification time 00Z/05

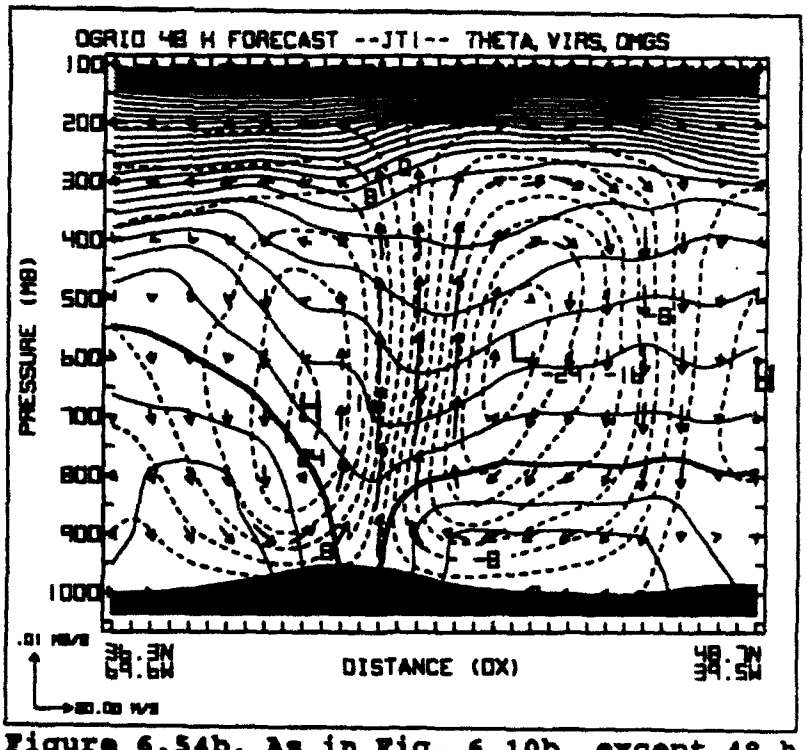

Figure 6.54b. As in Fig. 6.10b, except 48 h forecast, verification time 00Z/05

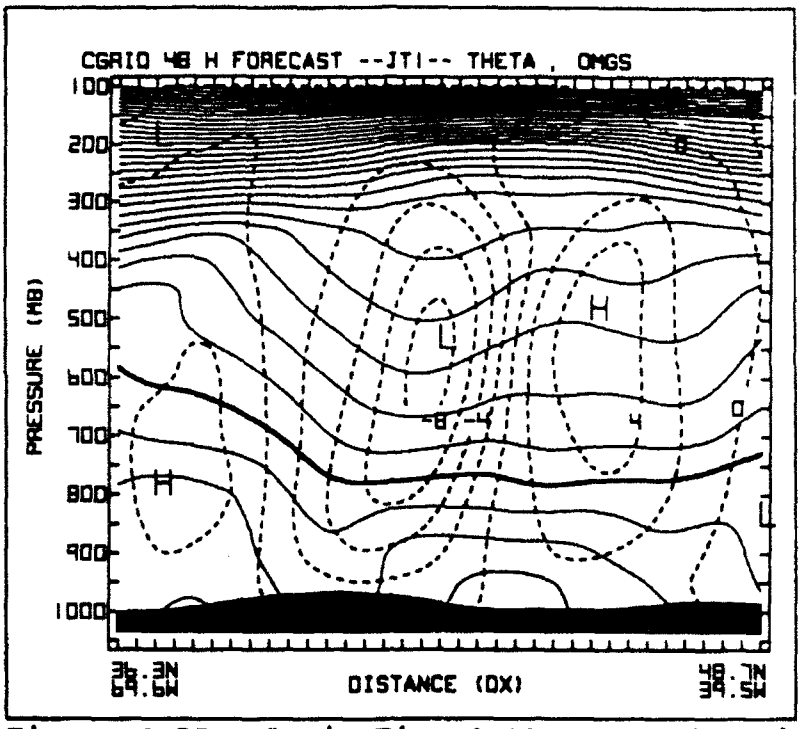

Figure 6.55a. As in Fig. 6.11a, except 48 h forecast, verification time 00Z/05

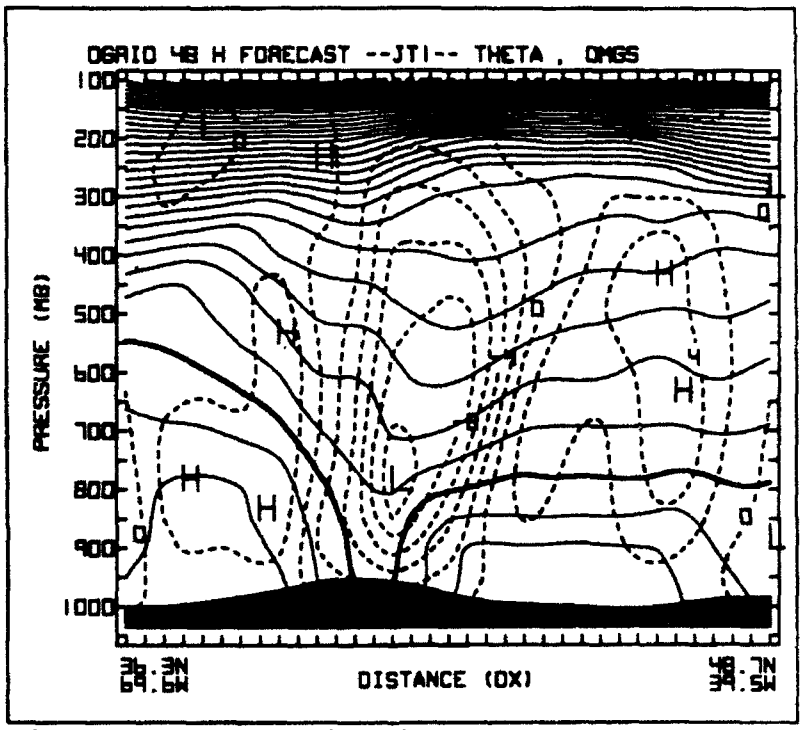

Figure 6.55b. As in Fig. 6.11b, except 48 h forecast, verification time 00Z/05

VII. CONCLUSIONS

A. DISCUSSION AND CONCLUSIONS

This study examined the effect model resolution had on the numerical prediction of the ERICA IOP-4 cyclone. The importance of resolution in numerical models has been demonstrated by studies such as Kuo and Low-Nam (1990), Weygandt and Seaman (1988), and Pecnick and Keyser (1989). This study investigated how sensitivity to resolution is capable of depicting lower central pressures and subsequently producing better forecasts. In particular, the role the ageostrophic vertical circulations played to produce the rapid intensification of this oceanic cyclone is investigated (Keyser et al. 1989). In order to diagnose the ageostrophic vertical circulations, the psi-vector technique was used to compute the divergent ageostrophic wind from the vertical motion and to project the circulation onto any arbitrary plane, as described by Keyser et al. (1989) and Loughe (1992).

This study compared experimental forecasts by the NGM at two different resolutions. The C-grid configuration was the same as the 1989 operational version of the NGM, except for a 20° eastward rotation of the grid system. This version of the model had a grid spacing of 92.45 km at 60°N on 16 terrain-following sigma levels. The NGM D-grid configuration had

twice the horizontal and vertical resolution of that in the C-grid, namely a grid spacing of 46.44 km at 60°N on 32 sigma levels.

The NGM C-grid forecast was slow to develop the cyclone, which was primarily due to resolution limitations and smoothing in the model as suggested by Pauley and Bramer (1992). On the other hand, the D-grid forecast was only slow in initially deepening the system during the first 6 h, thereafter exhibiting deepening rates similar to those observed. According to the NS analyses, the cyclone had a central pressure of 996 mb at 00Z/04 and deepened to 936 mb within 24 h. The NGM C-grid 48 h forecast depicted a central pressure of 959 mb at 00Z/05, 23 mb weaker than the NS analysis. On the other hand, the D-grid 48 h forecast showed a central pressure of 949 mb at 00Z/05, only 13 mb weaker than the NS analysis. However, the D-grid 30 h forecast was 16 mb weaker than the NS analysis, indicating that the disparity between the D-grid and the NS analyses occurred primarily during the initial 6 h.

The NS analyses of the IOP-4 cyclone exhibited evidence of a frontal structure similar to that proposed by Shapiro and Keyser (1990). Although slow in the evolution of this cycle, the D-grid forecasts displayed a progression from the frontal fracture phase to a T-bone configuration to a pronounced bent-back warm front wrapping around the cyclone. However, the D-grid forecast never quite formed the mature warm-core

seclusion phase as presented in the NS analyses at 00Z/05. On the other hand, the C-grid forecast displayed little evidence of the Shapiro and Keyser (1990) conceptual model of frontal feature. The cold-frontal temperature gradient was slow to form the frontal fracture and never separated from the low center forming the T-bone structure, but instead maintained its strength and extended into the center of the low for most of the forecast period. Only in the 48 h forecast, is there any indication of a bent-back warm front with some sign of a frontal fracture.

This study used the Keyser et al. (1989) technique for diagnosing vertical circulations. Using the three-component partitioning proposed by Lynch (1989) the ageostrophic wind can be decomposed into rotational $\vec{V}_{agr}$, divergent $\vec{V}_{agd}$, and harmonic $\vec{V}_{agh}$ components. The harmonic component $\vec{V}_{agh}$ isolates boundary effects and is both irrotational and nondivergent. The vertical motion ω is associated only with $\vec{V}_{agd}$, therefore, the vertical circulation can be written in terms of ω and $\vec{V}_{agd}$, both of which can be written in terms of the vector streamfunction $\vec{\Psi}$. As a result the vertical circulation can be projected onto any plane by projecting $\vec{\Psi}$ onto that plane.

Curvature effects associated with the upper-level trough/ridge system played an important role in the development of the IOP-4 cyclone. The subgeostrophic flow in

the upper-level trough and the supergeostrophic flow in the upper-level ridge were associated with significant longitudinal ageostrophic circulations and ascent. The strong ascent values led to low-level convergence and spin-up along with upper-level mass divergence, which acted to develop the surface cyclone. The magnitude of ascent associated with the longitudinal circulations increased throughout the C-grid forecasts from 4 μb s^{-1} in the 24 h forecast to 10 μb s^{-1} in the 48 h forecast. On the other hand, the D-grid forecast showed ascent to increase from 6 μb s^{-1} in the 24 h forecast to a maximum of 12 μb s^{-1} in the 42 h forecast and then decreased slightly in the 48 h forecast. Except for the 24 h forecast, the longitudinal circulations were stronger in the D-grid forecast than that of the C-grid.

The transverse ageostrophic circulations associated with jet streak dynamics were crucial in the rapid deepening of the low-level cyclone. A jet's entrance and exit region are characterized by transverse ageostrophic components which represent the upper branch of the direct and indirect circulations, respectively. A comparison of the C- and D-grid forecasts indicate the largest difference in the deepening rate occurred between the 30 h and 36 h forecasts. During this period, the northern jet streak developed at 300 mb with the D-grid having a different structure and orientation than the C-grid, with a greater wind speed maximum, greater

curvature and a more elongated configuration. The laterally coupled jet streaks produced strong transverse ageostrophic circulations evident by a strong thermally direct and indirect circulation in the JT2 cross-sections. The transverse circulation patterns were stronger in the D-grid forecast than in the C-grid, which ultimately led to the D-grid forecast experiencing greater divergence aloft, stronger ascent and greater spin-up of the low-level cyclone. The magnitude of ascent associated with the transverse circulations increased from 4 $\mu b\ s^{-1}$ for both the C- and D-grid 24 h forecast to 14 $\mu b\ s^{-1}$ in the C-grid 42 h forecast and 20 $\mu b\ s^{-1}$ in the D-grid 42 h forecast. However, both forecasts depicted a decrease in the ascent magnitude to 12 $\mu b\ s^{-1}$ in the C-grid and 14 $\mu b\ s^{-1}$ in the D-grid at the 48 h forecast. After the formation of the second jet streak the ascent magnitudes associated with the transverse circulations were stronger than those associated with the longitudinal circulations. These dynamical differences were associated with higher model resolution; the ERICA IOP-4 cyclone deepened substantially more in the higher resolution forecast.

B. RECOMMENDATIONS

Possible future studies should include the following:

- Explicitly separate $\vec{V}_{ag}$ into components parallel and perpendicular to the geostrophic wind which would more clearly separate the curvature vs. jet streak effects.

- Examine the evolution of the northern jet streak and its dependence on diabatic processes. Two cases of Kuo and Low-Nam (1990) model output showed such a dependence on latent heating.

- Examine low-level frontogenesis to better understand differences in low-level frontal structure in the C- and D-grid forecasts.

- Examine the sensitivity to model resolution for the strong tropopause fold illustrated by Neiman and Shapiro (1992) in this case.

- Partition the ageostrophic wind using a staggered grid, thereby, yielding an exact recovery of the total ageostrophic wind.

REFERENCES

Eliassen, A., 1984: Geostrophy. *Quart. J. Roy. Meteor. Soc.*, **110**, 1-12.

Gyakum, J.R., P.J. Roebber, and T.A. Bullock, 1992: The role antecedent surface vorticity development as a conditioning process in explosive cyclone intensification. *Mon. Wea. Rev.*, **120**, 1465-1489.

Hoke, J.E., N.A. Phillips, G.J. DiMego, J.J. Tuccillo, and J.G. Sela, 1989: The regional analysis and forecast system of the National Meteorological Center. *Weather and Forecasting*, **4**, 323-334.

Hoskins, B.J., I. Draghici, and H.C. Davies, 1978: A new look at the ω-equation. *Quart. J. Roy. Meteor. Soc.*, **104**, 31-38.

Hoskins, B.J., and M.A. Pedder, 1980: The diagnosis of middle latitude synoptic development. *Quart. J. Roy. Meteor. Soc.*, **106**, 707-719.

Houghton, D.D., R.A. Petersen, and R.L. Wobus, 1992: Spatial resolution impacts on National Weather Service Nested Grid Model simulations. Submitted to *Mon. Wea. Rev.*

Keyser, D., B.D. Schmidt and D.G. Duffy, 1989: A technique for representing three-dimensional vertical circulations in baroclinic disturbances. *Mon. Wea. Rev*, **117**, 2463-2494.

Kocin, P.J., and L.W. Uccellini, 1990: *Snowstorms Along the Northeastern Coast of the United States: 1955 to 1985.* Amer. Meteor. Soc., 280 pp.

Kuo, Y.-H., and S. Low-Nam, 1990: Prediction of nine explosive cyclones over the Western Atlantic Ocean with a regional model. *Mon. Wea. Rev.*, **118**, 3-25.

Loughe, A.F., 1992: Real data diagnosis of partitioned ageostrophic vertical circulations. M.S. Thesis, State University of New York-Albany, 138 pp.

Lynch, P., 1988: Deducing the wind from vorticity and divergence. *Mon. Wea. Rev.*, **116**, 86-93.

Lynch, P., 1989: Partitioning the wind in a limited domain. *Mon. Wea. Rev.*, **117**, 1492-1500.

Neiman, P.J., and M.A. Shapiro, 1992: The life cycle of an extratropical marine cyclone. Part I: Frontal-cyclone evolution and thermodynamic air-sea interaction. Submitted to *Mon. Wea. Rev.*

O'Brien, J.J., 1970: Alternative solutions to the classic vertical velocity problem. *J. Appl. Meteor.*, **9**, 197-203.

Pauley, P.M., R.L. Wobus, and M.J. Pecnick, 1991: Sensitivity of forecasts of rapid oceanic cyclogenesis to model resolution. Preprints, *Ninth Conf. on Numerical Weather Prediction*, Denver, Amer. Meteor. Soc., 756-759.

Pauley, P.M., and B.J. Bramer, 1992: The effect of resolution of the depiction of central pressure for an intense oceanic extratropical cyclone. *Mon. Wea. Rev*, **120**, 757-769.

Pecnick, M.J., and D. Keyser, 1989: The effect of spatial resolution on the simulation of upper-tropospheric frontogenesis using a sigma-coordinate primitive equation model. *Meteor. Atmos. Phys.*, **40**, 137-149.

Persson, P. Ola. G., and T.T. Warner, 1991: Model generation of spurious gravity waves due to inconsistency of the vertical and horizontal resolution. *Mon. Wea. Rev.*, **119**, 917-935.

Petterssen, S., 1956: *Weather Analysis and Forecasting, Vol. I.*, 2nd ed., McGraw-Hill, 428 pp.

Sanders, F., 1987: Skill of NMC operational dynamical models in prediction of explosive cyclogenesis. *Weather and Forecasting*, **2**, 322-336.

Sanders, F., and E.P. Auciello, 1989: Skill in prediction of explosive cyclogenesis over the western North Atlantic Ocean, 1987/88: a forecast checklist and NMC dynamical models. *Weather and Forecasting*, **4**, 157-172.

Sanders, F., 1990: Surface analysis over the oceans--searching for sea truth. *Weather and Forecasting*, **5**, 596-612.

Shapiro, M.A., and D. Keyser, 1990: Fronts, jet streams, and the tropopause. *Extratropical Cyclones, The Erik Palmén Memorial Volume*, C.W. Newton and E. Holopainen, Eds. Amer. Meteor. Soc., 167-191.

Uccellini, L.W., and P.J. Kocin, 1987: The interaction of jet streak circulation during heavy snow events along the East Coast of the United States. *Weather and Forecasting*, **2**, 289-308.

Wakimoto, R.M., W. Blier, and C. Liu, 1992: The frontal structure of an explosive oceanic cyclone: Airborne radar observations of ERICA IOP4. *Mon. Wea. Rev.*, **120**, 1135-1155.

Weygandt, S.S., and N.L. Seaman, 1988: The relationship between forecast accuracy and grid resolution in simulations of mesoscale features accompanying cyclogenesis. Preprints, *Eighth Conf. on Numerical Weather Prediction*, Baltimore, MD, Amer. Meteor. Soc., 700-707.

VIII. INITIAL DISTRIBUTION LIST

1.	Defense Technical Information Center Cameron Station Alexandria, VA 22304-6145	2
2.	Library, Code 52 Naval Postgraduate School Monterey, CA 93943-5002	2
3.	Chairman (Code MR/Hy) Department of Meteorology Naval Postgraduate School Monterey, CA 93943-5002	1
4.	Dr. Patricia M. Pauley (Code MR/Pa) Department of Meteorology Naval Postgraduate School Monterey, CA 93943-5002	2
5.	Dr. Carlyle H. Wash (Code MR/Wx) Department of Meteorology Naval Postgraduate School Monterey, CA 93943-5002	1
6.	LT James Berdeguez COMUNDERSEASURVLANT (N31) Norfolk, VA 23511-5220	1
7.	Commander Naval Oceanography Command Stennis Space Center MS 39529-5001	1
8.	Commanding Officer Fleet Numerical Oceanography Center Monterey, CA 93943-5005	1
9.	Commanding Officer Naval Research Laboratory Stennis Space Center MS 39529-5004	1
10.	Director Naval Research Laboratory Monterey, CA 93943-5006	1

11. Chief of Naval Research 1
800 N. Quincy Street
Arlington, VA 22217

12. Office of Naval Research (Code 420) 1
Naval Ocean Research and Development Activity
800 N. Quincy Street
Arlington, VA 22217